




8-2012

Morphology-properties studies in laser synthesized nanostructured materials

Nozomi Shirato
nshirato@utk.edu

Follow this and additional works at: https://trace.tennessee.edu/utk_graddiss

 Part of the [Condensed Matter Physics Commons](#), [Engineering Physics Commons](#), [Fluid Dynamics Commons](#), [Optics Commons](#), and the [Semiconductor and Optical Materials Commons](#)

Recommended Citation

Shirato, Nozomi, "Morphology-properties studies in laser synthesized nanostructured materials. " PhD diss., University of Tennessee, 2012.
https://trace.tennessee.edu/utk_graddiss/1395

This Dissertation is brought to you for free and open access by the Graduate School at TRACE: Tennessee Research and Creative Exchange. It has been accepted for inclusion in Doctoral Dissertations by an authorized administrator of TRACE: Tennessee Research and Creative Exchange. For more information, please contact trace@utk.edu.

To the Graduate Council:

I am submitting herewith a dissertation written by Nozomi Shirato entitled "Morphology-properties studies in laser synthesized nanostructured materials." I have examined the final electronic copy of this dissertation for form and content and recommend that it be accepted in partial fulfillment of the requirements for the degree of Doctor of Philosophy, with a major in Materials Science and Engineering.

Ramki Kalyanaraman, Major Professor

We have read this dissertation and recommend its acceptance:

Jon Camden, Gerd Duscher, David Mandrus, Philip Rack

Accepted for the Council:

Carolyn R. Hodges

Vice Provost and Dean of the Graduate School

(Original signatures are on file with official student records.)

Morphology-properties studies in laser synthesized nanostructured materials

A Thesis Presented for the
Doctor of Philosophy in Materials Science and Engineering
The University of Tennessee, Knoxville

Nozomi Shirato

August 2012

Acknowledgments

I owe special thanks to all those who have made the completion of my dissertation a reality. I would like to thank my advisor, Dr. Ramki Kalyanaraman for guidance and support and providing me with an excellent atmosphere for doing research. I am deeply grateful to him for the long discussions that helped me sort out the technical details of my work. I would also like to thank my dissertation committee members, Dr. Jon Camden, Dr. Gerd J. Duscher, Dr. David Mandrus and Dr. Philip D. Rack for their helpful advice and inputs. I have been very fortunate to collaborate with Dr. Anup K. Gangopadhyay in Washington University in St. Louis, Dr. Sudipta Seal in the University of Central Florida and Dr. Hernando Garcia in Southern Illinois University Edwardsville, and I also thank Dr. Seal's group members, Amit Kumar, Rameech McCormack, Abhilash Vincent and Umesh Singh. I also express my appreciation to Dr. Hare Krishna for great discussions and critical suggestions. In addition, I really appreciate encouragement from my lab-mates, Abhinav Malasi, Vanessa Ramos, Ritesh Sachan, Sagar Yadavali and friends, Dhivya and Sudershana.

I would like to thank all the people who have guided me in my life. Thank you to my family, whose moral and emotional support and love has made my life a joy. Also, I would like to acknowledge contributions from collaborators in details.

- Dr. J. Strader for his contribution in developing and analyzing the thermal profile simulation [shown in Figs. 2.7, 2.10, 2.14, 2.15 and 2.16].
- P. Mreutesatorn for his contribution in AFM measurements on SnO₂ nanoarrays [shown in Figs. 2.6 and 2.9].
- Dr. Karakoti for his contribution in conducting XPS and XRD measurements using EMSL, a national scientific user facility sponsored by the Department of Energy's Office of Biological and Environmental Research, located at the Pacific Northwest National Laboratory [shown in Figs. 2.3 and 2.4].
- Dr. H. Krishna for his help in development and calculation of TH model in the chapter 3.
- E. Mintun and S. Sherrill for their contribution in helping implementation of SMOKE system [shown in Figs. 4.2, 4.3, 4.5 and 4.6].
- U. Singh and Dr. H. J. Cho for their contribution in preparing electrical contacts (Au pads and wire bonding) to SnO₂ nanostructured arrays [shown in Fig. 2.11].

- A. Kumar, R. McCormack, and Dr. S. Seal for their contribution in performing hydrogen gas sensor evaluation of SnO₂ nanostructured arrays under dynamic condition of hydrogen environment [shown in Figs. 2.12(a)-(c)].
- R. Sachan and Dr. G. Duscher for their contribution in performing TEM and EELS analysis of a Co-Ag nanoparticle [shown in Fig. 6.1].

Abstract

Synthesis of well-defined nanostructures by pulsed laser melting is an interesting subject from both a fundamental and technological point of view. In this thesis, the synthesis and functional properties of potentially useful materials were studied, such as tin dioxide nanostructured arrays, which have potential applications in hydrogen gas sensing, and ferromagnetic Co nanowire and nanomagnets, which are fundamentally important towards understanding magnetism in the nanoscale. First, the formation of 1D periodic tin dioxide nanoarrays was investigated with the goal of forming nanowires for hydrogen sensing. Experimental observations combined with theoretical modeling successfully explained the mechanisms of structure formation. One of the primary findings was that evaporation of tin dioxide was the most significant contributor to the pattern formation. Next, the spontaneous liquid film spinodal dewetting process under pulsed laser melting was modeled using the viscous dissipation approach. We found that the fluid condition for spinodal dewetting is where the film-substrate tangential stress is zero. Following this, the remainder of the thesis focused on synthesis and characterization of magnetic nanostructures. We first successfully installed a home-built Surface Magneto-optical Kerr Effect (SMOKE) system. Using SMOKE we measured the Kerr rotation from potential plasmonic-ferromagnetic magneto-optical materials made from Co-Ag thin films and nanoparticles as a function of composition. We found that films made by co-deposition of Co and Ag showed higher Kerr rotation in contrast to bilayer film structures with same effective amount of Co and Ag. Next, we investigated the shape and size dependence of magnetic properties of nanostructures, specifically hemispherical nanoparticles, nanowires and nanorods, prepared by the pulsed laser process. The magnetic anisotropy was studied by using the SMOKE system complemented with magnetic force microscopy (MFM) analysis. Results from magnetic hysteresis measurements of the nanostructures in different geometries showed coercivity and remanence that could be attributed to magnetic shape anisotropy. MFM analysis showed that domain orientation was found to depend on the aspect ratio of the nanostructure. These investigations generally helped advance the science of nanostructure synthesis using nanosecond pulsed laser techniques as well demonstrate that SMOKE is a promising method to investigate nanostructure magnetism.

Contents

Abstract	iv
1 Structure-property studies in laser synthesized nanostructured materials: An introduction and overview	1
1.1 Introduction	1
1.2 Functional Nanostructured materials and techniques	3
1.2.1 Nanostructured array based gas sensors	3
1.2.2 Magnetic nanostructures	5
1.2.3 Surface magneto-optical Kerr effect (SMOKE) sensing with plasmonic-ferromagnetic (PF) materials	6
1.3 Synthesis of nanomaterials by self-organization and/or self-assembly	7
1.3.1 Self-organization by spinodal dewetting	7
1.3.1.1 Theory of spinodal dewetting	8
1.3.2 Background and/or state-of-art for spinodal dewetting	10
1.3.2.1 Pulsed laser induced Spinodal dewetting (PLiD)	10
1.3.2.2 Thin metal film dewetting: $2 < h < 20$ nm	11
1.4 Outline of Dissertation	12
2 Thickness dependent self limiting 1-D tin oxide nanowire arrays by nanosecond pulsed laser irradiation for hydrogen sensing	15
2.1 Summary	15
2.2 Introduction	16
2.3 Experimental Procedure	17
2.4 Results	18
2.4.1 Nanostructured arrays morphology	18
2.4.2 Crystal and chemical bonding properties	18
2.4.3 Understanding formation mechanism of NSA from films	21
2.4.3.1 Initial film thickness dependence	21
2.4.3.2 Laser energy density dependence	22
2.4.4 Collaborative work on SnO ₂ NSA based hydrogen sensor	23
2.4.4.1 Experimental details of sensor array fabrication	24

2.4.4.2	Testing of Sensor Devices by UCF collaborators	25
2.4.4.3	Testing Results and Discussion	26
2.5	Discussion	27
2.6	Conclusion	31
3	Thermodynamic modeling of thin metallic liquid films dewetting	36
3.1	Summary	36
3.2	Introduction	36
3.3	Theory	38
3.4	Results and Discussion	40
3.4.1	Dispersion relation for classical dewetting	40
3.4.2	Dispersion relation for thermocapillary dewetting from thermodynamics	42
3.4.2.1	Dispersion using minimum viscous dissipation	44
3.5	Conclusion	46
4	Implementation and testing of surface magneto-optical Kerr effect (SMOKE) system	48
4.1	Summary	48
4.2	Introduction	49
4.3	SMOKE system	50
4.3.1	Theory	50
4.3.1.1	<i>Faraday effect / Cotton-Mouton effect</i>	50
4.3.1.2	<i>Kerr effect</i>	50
4.3.2	Experimental setup	51
4.3.2.1	The Kerr rotation and ellipticity from experimental data	51
4.3.2.2	Software: Interfacing SMOKE system with PC using LabVIEW	53
4.4	Sample preparations and testing	53
4.5	Results and discussion	54
4.5.1	Co-deposited Co-Ag films	54
4.5.2	Bilayer vs co-deposited Co-Ag	54
4.5.3	Film vs nanoparticles	55
4.6	Conclusion	55
5	Magnetic properties of Co nanowires and nanoparticle arrays synthesized by pulsed laser melting	64
5.1	Summary	64
5.2	Introduction	65
5.3	Experimental Details	66
5.3.1	Synthesis of nanoparticle arrays by nanosecond pulsed laser dewetting	66
5.3.2	Synthesis of 1-D nanowire arrays by two beam interference irradiation	67
5.3.2.1	SMOKE measurements	67

5.4	Results	68
5.4.1	SEM, AFM and MFM	68
5.4.2	SMOKE	71
5.4.2.1	Co and Ni nanoparticles (NP1, NP2 and NP3)	71
5.4.2.2	Co nanostructures (TF, SW, NRNP, ONP and GW)	73
5.5	Discussion	74
5.5.1	Co and Ni nanoparticle arrays	74
5.5.2	Dependence of magnetic domain properties on aspect ratio	75
5.5.3	The chain of spheres model	75
5.6	Conclusion	77
6	Summary and Future work	79
6.1	Summary	79
6.2	Future directions	80
6.2.1	In ₂ O ₃ -doped SnO ₂ NSA based hydrogen sensor	80
6.2.2	Wavelength-dependent SMOKE of plasmonic-ferromagnetic (PF) composites	81
	List of References	83
	Vita	97

List of Figures

1.1	<i>The characteristic nanomorphologies following nanosecond pulsed laser-induced spontaneous dewetting of an ultrathin Ag film on SiO₂ substrates. (left) At early stages of dewetting (irradiation by ~10 laser pulses), holes with a narrow size distribution. (center) Later stage dewetting (~1000 pulses) leads to the formation of polygonal features with a narrow size distribution. (right) The final dewetting state (~10,000 pulses) consists of nanoparticles with a well defined nearest-neighbor spacing. Each image is of dimensions 8μm × 8μm. Figures and text taken from ref. [1].</i>	2
1.2	<i>(a) (left) Schematic representation of band bending model illustrating adsorption of O₂ at the surface and, (right) variation of the gas sensor's electrical conductance during the alternative exposure to O₂ and H₂ are shown [2]. (b) Schematic view of SnO₂ nanowire based gas sensing device. The wires are covered with vapor-deposited Pd clusters [3].</i>	4
1.3	<i>Characteristics of the nanocrystalline SnO₂ based thin film H₂ sensors. Each data point represents reported SnO₂ based H₂ sensor sensitivity at certain operating temperature. The sensors exhibit maximum H₂ sensitivity in the high temperature range (250 to 300°C). [4] .</i>	5
1.4	<i>(a) The simulated contrast in the MFM images of a single domain ferromagnetic particle with (left) in-plane (0 deg), (center) at an angle of 45 deg and (right) perpendicular to the plane (90 deg) [5], (b) High resolution MFM image of a portion of a Co nanowire, 150 nm in a diameter and (right) possible domain structures [6].</i>	6
1.5	<i>(a) Wind-blown ripples on the surface of a sand dune [7], (b) spiral patterns produced by the Belousov-Zhabotinski chemical reaction [8] and (c) Co nanoparticles with well-defined size and shape [9].</i>	8
1.6	<i>(a) (left) Micrographs at the holes state during dewetting of a 40 nm thick polystyrene film on a Si wafer and (right) Double logarithmic plot of the average diameter of particles and the average interparticle spacing (calculated from average number of particles per unit area) as a function of film thickness [10]. (b) Dewetting morphology of a 4 nm PS film on Si wafer as a function of annealing time. (left) Circular holes, (center) holes break up and (right) droplets formation at the end of the dewetting process [11].</i>	9

1.7	<i>Comparisons of characteristic pattern length scales for Co (dashed line) and Fe (solid line) film on SiO₂. The symbols represent the ratio of the experimentally measured nearest-neighbor spacing Λ_{expt} to the spinodal length scale Λ_c. The lines represent the ratio Λ/Λ_c, where Λ is the predicted length scale in the presence of intrinsic thermocapillary effects. For Co film thickness < 9 nm, Λ_{expt} increases $\sim h^2$ consistent with spinodal dewetting, however for thickness ≥ 9 nm case Λ_{expt} decreases sharply with increasing h. Taken from ref. [12].</i>	12
2.1	<i>(a) SEM images of SnO₂ nanowires synthesized from a 42 nm film at 300 mJ cm⁻² and an interference angle of 72°. SnO₂ rich and poor regions correspond to bright and dark contrasts, respectively. The average nanowire spacing is 232.3 nm while average width was estimated to be 97 nm. (b) AFM topography image of SnO₂ nanowires of the same sample as (a). (c) A typical AFM line profile of the nanowires of (b). From such line profiles, the average nanowire height, h_{nw}, could be calculated, and in this case it was 16 nm.</i>	19
2.2	<i>EDS (Energy-dispersive X-ray spectroscopy) measured areal density of Sn (wt. %/μm^2) with respect to as-deposited SnO₂ film thickness (nm). The exponential growth fit (red) and linear fit (blue) curves are shown.</i>	20
2.3	<i>XPS (X-ray photoelectron spectroscopy) spectra of Sn 3d_{5/2} measured on SnO₂ film and nanowires. The film (line with open symbols) and nanowires (line with closed symbols) photoemission intensity peaks of, 486.46 and 486.57 (eV) respectively, correspond with the binding energy of Sn⁴⁺ component, which is 486.3 (eV) [13]. Inset shows SEM image of nanowire region from which XPS was measured.</i>	20
2.4	<i>XRD spectra with the background removed of an SnO₂ (top) NSA sample with low index reflections of SnO₂ identified, where the relative intensity of the reflections indicate a tetragonal polycrystalline structure of $a = 4.78$ Å and $c = 3.21$ Å. (bottom) film sample, which indicates a single crystalline tetragonal structure due to the lack of SnO₂ reflections beyond (110) and (220).</i>	21
2.5	<i>SEM images of SnO₂ nanowires formed from two different initial film thickness (a) $h_o = 90$ nm and (b) $h_o = 15$ nm using the same interference angle, $\theta_i = 72^\circ$ and 3000 pulses at an energy density of 308 mJ/cm². The average nanowire spacing of (a) and (b) are 221 nm and 216 nm respectively.</i>	22
2.6	<i>AFM topography image and line scans of the wire profile of SnO₂ nanowire arrays formed from three different initial film thickness, (a) $h_o = 15$, (b) $h_o = 25$ and (c) $h_o = 90$ nm respectively. The SEM images of the sample $h_o = 15$ and 90 nm are shown in Fig 2.5. All three nanowires were synthesized using the same interference angle, $\theta_i = 72^\circ$ and 3000 pulses at an energy density of 308 mJ cm⁻². The average nanowire height of each sample is (a) $h_{\text{nw}} = 2$, (b) $h_{\text{nw}} = 8$ and $h_{\text{nw}} = 15$ nm.</i>	23

2.7	<i>Behavior of the nanowire characteristics prepared at the same laser energy density as a function of starting film thickness. (a) Experimentally determined nanowire height h_{nw} (open circles, left axes) and theoretically estimated integrated evaporation Γ^* (line, right axes). The nanowire height h_{nw} increases with increasing starting film thickness h_0. (b) Observation of the self-limiting effect. The experimentally measured remaining film thickness h_{rem} (symbols) is almost similar for all the films. The laser energy density used was 300 mJ cm^{-2}, the interference angle was 72° and the number of pulses was 3000 for all samples.</i>	24
2.11	<i>Image obtained through confocal microscope of SnO₂ nanostructured array supported on SiO₂/Si substrate with Au pads and wire bonding. It shows the sensing material region exposed to the environment [14].</i>	24
2.8	<i>SEM images of nanowires from 42 nm film for two different E_0 with the interference angle, $\theta_i = 86^\circ$, and 3000 laser pulses. (a) $E_0 = 440 \text{ mJ cm}^{-2}$ and (b) magnified image of (a). (c) $E_0 = 535 \text{ mJ cm}^{-2}$ and (d) magnified image of (c).</i>	25
2.9	<i>AFM line scans of the wire profiles of SnO₂ nanowires formed from three different energy densities (a) $E_0 = 440$, (b) $E_0 = 535$ and (c) $E_0 = 700 \text{ mJ cm}^{-2}$. The initial film thickness was 42 nm, the interference angle was 86°, and the number of laser pulses was 3000. The average for all measured nanowire height for each sample is (a) $h_{nw} = 14$, (b) $h_{nw} = 16$ and $h_{nw} = 19 \text{ nm}$ respectively.</i>	26
2.10	<i>Behavior of h_{nw} and h_{rem} as a function of E_0 for 42nm films at an interference angle of 86° irradiated by 3000 pulses: (a) the experimentally determined nanowire height (open circles, left axes) and theoretically predicted behavior of the integrated evaporation difference Γ^* between regions of maxim and minima (dashed line, right axes). (b) The experimentally measured (open symbols) and theoretically predicted (line) remaining film thicknesses h_{rem}.</i>	27
2.12	<i>(a) The resistance variation of SnO₂ nanostructured array (red line) and SnO₂ thin film (green line) at room temperature on exposure to hydrogen gas in a wide range of concentration, ranging from 300 ppm to 6000 ppm. Change in resistance does not decrease significantly from 6000 ppm to 300 ppm, which demonstrates the sensor capability to detect H₂ gas at very low concentrations. The resistance of the film sensor does not change significantly on exposure to H₂ gas and the change in the resistance do not significantly increase with increasing H₂ gas concentration even upto 9000 ppm. (b) The exhibited electrical response of the SnO₂ NSA to the varying H₂ concentrations shows that minimum sensitivity is around 137. This is evidences that SnO₂ are more than capable of detecting lower concentration. The electrical response of the SnO₂ film is relatively insensitive [14].</i>	28
2.13	<i>The resistance variation of SnO₂ nanostructured array (red line) and SnO₂ thin film (green line) at room temperature on exposure to hydrogen gas at a constant concentration at 3000 ppm. Cyclic exposure to fixed concentration of H₂ shows that the sensor is very robust and stable [14].</i>	29

2.14	(a) Schematic of geometry used for the optical + thermal model. (b) The measured reflectivity, and (c), transmittance (open symbols) of known thicknesses of SnO ₂ deposited on 750 μm quartz from optical spectroscopy. The best fits (crosses) were modeled assuming $N_{\text{SnO}_2} = 2.0 - 0.97i$.	29
2.15	Absorption profiles of the SnO ₂ /SiO ₂ /Si stack for the case of: (a) complete constructive interference depth profile and (b) surface absorption profile.	30
2.16	Thermal model results showing: (a) the temperature difference between the the interference maxima and minima when the entire film has melted; (b) maximum surface temperature as a function of SnO ₂ film thickness for $\theta = 72^\circ$ and $E_o = 400 \text{ mJ/cm}^2$; and (c) maximum surface temperature as a function of SnO ₂ film thickness for $\theta = 86^\circ$ and $E_o = 550 \text{ mJ/cm}^2$. The shaded regions in (b) and (c) represent the integrated evaporation difference Γ^* .	31
3.1	(a) Plot of the growth rate versus wave number for the dispersion relation obtained from the dissipation approach for strong thermal gradients. The data was evaluated for Co film of thickness 8 nm and various values of the gradient T_h , as indicated on the plot. (b) Plot of the characteristic length scale Λ_{TC}^{TH} for Co films on SiO ₂ as a function of various T_h . (c) Plot of the cut-off wavelength $\Lambda_{\text{cut-off}}$ for Co films on SiO ₂ as a function of various T_h . The cut-off wave number corresponds to the intersection of the rate with the wave number axis in Fig. (a).	47
4.1	Magneto-optical Kerr effects taking place when light reflected from surface of a magnetized material: (left) polar, (center) longitudinal and (right) transverse effects. \mathbf{E}_i , \mathbf{E}_r and $\mathbf{P}_{\text{plane}}$ denote incident and reflected electric fields and plane of incidence, respectively [15].	57
4.2	Schematic of the SMOKE system in (a) polar and (b) longitudinal geometries.	57
4.3	Front panel of LabVIEW GUI. (a) Main control and (b) measurement parameters input (indicated with red boxes) panels.	58
4.4	Raw SMOKE hysteresis loops of (a) Kerr rotation and (b) ellipticity, respectively. Averaged SMOKE hysteresis loops of (c) Kerr rotation and (d) ellipticity.	59
4.5	The block diagram of the LabVIEW GUI. Each red box indicates sub-diagram: hysteresis sweep control, dataflow control and output file control diagrams.	60
4.6	Processes of linear drift adjustment. (top-left) Raw data of Kerr signal vs. applied field hysteresis loops with linear drift. (top-right) Converting the plot to Kerr signal vs. time, and finding the slope value from linear fit. (bottom-right) The linear slope is adjusted. (bottom-left) Re-plotted Kerr signal vs. applied field hysteresis loops.	61
4.7	The measured Kerr signal of co-deposited Co-Ag films on SiO ₂ /Si with respect to Co weight percentage.	61
4.8	The measured Kerr signal of co-deposited Co-Ag films and nanoparticles as a function of Co weight percentage.	62

4.9	<i>SEM micrograph of arrays of Co-Ag nanoparticles with different Co weight percentage: (a) 100 %, (b) 50 % and (c) 35 %. The corresponding size distribution of nanoarrays obtained: (d) [from image (a)], (e) [from (b)] and (f) [from (c)].</i>	62
4.10	<i>Energy-dispersive X-ray mapping taken in SEM on the arrays of nanoparticles obtained from dewetting of co-deposited Co-Ag film. The image (a) is combined elemental maps of Co and Ag; (b) is the elemental maps of Co; (c) is the elemental maps of Ag. The size of images is 600 nm x 600 nm. The array of nanoparticles obtained from the thickness combinations of Co : Ag = 6 : 2 nm.</i>	63
5.1	<i>(a), (b), and (c) SEM images of Co arrays S1, Co array S2 and Ni array S3, respectively. (d), (e), and (f) The particle size distribution of corresponding to S1, S2, and S3 respectively. The average particle size D_{avg} estimated from the histograms are 53 nm (S1), 71 nm (S2) and 74 nm (S3).</i>	68
5.2	<i>SEM images of Co arrays of (a) grooved-wire, (b) single-wire, (c) rods/particles and (d) particles, respectively. (Co rich and SiO₂ rich regions correspond to bright and dark contrasts)</i>	69
5.3	<i>The nanostructure size distribution of (a) width and (b) length of Co single-wire, nanorod and nanoparticle arrays. The average width and length of wires and rods and diameter of particles estimated from the histograms are $W = 92$, $L = 1600$ nm (single-wire), $W = 82$ nm, $L = 357$ nm (rods) and $D = 132$ nm (particles), respectively.</i>	70
5.4	<i>AFM (left) and MFM (right) images of Co (a) grooved-wire, (b) single-wire, (c) rods/particles and (d) particles arrays, respectively.</i>	70
5.5	<i>Kerr signal - H hysteresis loops for arrays of Co hemispherical nanoparticles on SiO₂ (sample S1). The solid lines represent the data for polar geometry and the dashed lines for longitudinal geometry. The average diameter of the particle was 53 nm in diameter. (b) Hysteresis loop for arrays of Co hemispherical nanoparticles on SiO₂ (sample S2). The solid lines represent the data for polar geometry and the dashed lines for longitudinal geometry. The average diameter of the particle was 71 nm in diameter.</i>	71
5.6	<i>Hysteresis loops for the arrays of Co particles (sample S1 and S2) in (a) polar and (b) longitudinal geometries. The solid lines represent the data for S1 and the dashed lines for S2.</i>	72
5.7	<i>(a) Hysteresis loop for arrays of Ni hemispherical nanoparticles on SiO₂ (sample S3). The solid lines represent the data for polar geometry and the dashed lines for longitudinal geometry. The average diameter of the particle was 74 nm in diameter. (b) Comparison of hysteresis loops for the arrays of Co and Ni particles (sample S2 and S3) in polar and (c) longitudinal geometries. The dashed line represents S2 and the solid line represents the data for S3. The arrows mark the saturation points on the hysteresis curves.</i>	73
5.8	<i>Hysteresis loops for the arrays of Co (a) nanowire and (b) particles. (a) Comparison between hysteresis loops for the nanowire array in the L^{\parallel} and L^{\perp} geometries. (b) Comparison between hysteresis loops for the particle array in the L^{\parallel} and L^{\perp} geometries.</i>	74

5.9	<i>Hysteresis loops for the arrays of Co nanowires (single- and grooved-wire), rods/particles and particles. (a) Comparison between hysteresis loops for the four different nanostructure arrays in the L^{\parallel} geometry. (b) Comparison between hysteresis loops for grooved-wire, rods/particles and particles arrays in the polar geometry. In both (a) and (b), the red lines represent the data for grooved-wire, the green lines for single-wire, the blue lines for rods/particles and the violet lines for only particles.</i>	75
5.10	<i>Histogram of the in-plane aspect ratio (AR) distribution of nanostructures along with the nature of magnetic domain (single- vs multi-domain) and their magnetization orientation. The histogram indicates that the single domain and multi-domain nanostructure exists in the range of $1 < AR < 3$ and $AR \geq 3$, respectively. The AR values for out-of-plane and in-plane magnetization, as well as multi-domain magnetization are also shown</i>	76
5.11	<i>Measured values of the in-plane coercivity of Co nanowire, nanorod, and nanoparticle arrays (open circles) compared to the theoretical trend in coercivity obtained by the chain-of-spheres model [16].</i>	77
6.1	<i>(left) Cross-sectional TEM image of a Ag-Co nanoparticle made from Co-Ag bilayer films showing contrast variation indicating polycrystallinity within the particle. (center) Co and (right) Ag EELS elemental maps of the enclosed region shown in left image, exhibiting the immiscibility of Co and Ag in each other. The contrast bar shows the variation of atom % of Ag and Co individually in different locations. The size of elemental map image is 5.9 nm x 5.9 nm [17].</i>	81

List of Tables

2.1	<i>Optical values used in the simulation.</i>	30
2.2	<i>Thermal values used in the simulation. L is heat of transformation; ρ is density; k is thermal conductivity; C is heat capacity; T is temperature, and ϵ is phase change tuning parameter.</i>	33
4.1	<i>List of hardware used in the SMOKE system.</i>	52
4.2	<i>Table of co-deposited Co-Ag films parameters on SiO₂/Si substrates, including Co weight percentage and amount of Co and Ag in terms of film thickness. Experimentally measured Kerr rotation, θ_k, values are included.</i>	54
4.3	<i>Table of Co-Ag films with same sample parameters but different film structures: Co/Ag/SiO₂, Ag/Co/SiO₂ and co-deposited Co-Ag films. Experimentally measured Kerr rotation, θ_k, values of each sample are presented.</i>	54
4.4	<i>Table of co-deposited Co-Ag films and Co-Ag nanoparticle arrays with different composition. Each nanoparticle array was synthesized from the Co-Ag film with same composition. Measured Kerr rotation, θ_k, values are listed.</i>	55

Chapter 1

Structure-property studies in laser synthesized nanostructured materials: An introduction and overview

1.1 Introduction

Despite its relatively short history, concepts of nanotechnology have been discussed over a long period of time. As early as in the 1960's, Richard Feynman discussed in his famous lecture about "manipulating and controlling things on a small scale" that nanotechnology could be one of the most exciting advancements of science, and there was potential for an enormous number of technical applications [18]. He envisioned that at some point we might be able to arrange atoms the way we want, and that such technology would impact our life [18]. Twenty years later, as he predicted, the rise of nanotechnology gradually began due to technological advancements in fabrication and characterization. Scientists and engineers started inventing innovative methods to construct structures in the nanoscale by techniques such as physical vapor deposition (PVD), chemical vapor deposition (CVD), chemical etching, lithography, electrochemistry, and colloid & cluster chemistry. In parallel, they began to study nanoscopic properties, for example, by electron & ion microscopy, scanning probe microscopy (SPM), nano-indentation, X-ray spectroscopy, and optical/laser spectroscopy. For example, in 1982 Binnig and Rohrer developed a new type of microscopy system, scanning tunneling microscopy (STM), which was capable of imaging single atoms in Si crystal [19]. Scientists and researchers were intrigued by this nanomaterial because they exhibited surprisingly unique and extraordinary properties, such as exhibiting superparamagnetism when a ferromagnetic particle size decreases to nanoscale dimensions, improved catalytic processes by nanosized catalysts, strong light absorption in the UV-visible region due to the size and shape dependent localized surface plasmon resonance (LSPR), shape dependent enhanced magnetic anisotropy, and so on. Now, nanomaterials are acknowledged to have distinct physical properties from bulk materials and are being utilized in all areas of science and technology, including energy harvesting [20, 21, 22, 23, 24], catalysis [25], drug delivery [26], bio-imaging [27, 28], and biological-, chemical- and physical- sensing [29, 30, 31, 32, 33, 21, 34].

The common theme of this research involves the synthesis of nanomaterials by physical vapor thin film deposition and nanosecond pulsed laser irradiation. Pulsed laser synthesis and processing, especially in the nanosecond (ns) or shorter time scales, has enabled a number of advances in materials science due to the highly non-equilibrium nature of the interaction. One of the most important of these has been the ability to make stoichiometric films of important classes of materials, such as the high-Tc superconductors or transparent conducting oxides, which contain multiple different components with varying vapor pressure. As shown early on by the groups of Venkatesan et al in Maryland, and Narayan et al at NC State, films of the multi-component oxide high-Tc superconductors like YBCO or semiconductors like ZnO, could be made with extremely high quality by using nanosecond pulsed laser ablation [35, 36, 37, 38, 39]. In the context of the research presented here, nanosecond laser processing has been an enabling technique to study the spontaneous dynamics of ultrathin film deformation under melting, as was first shown by Bischof and co-workers in 1996 [40, 41]. Their nanosecond pulsed laser work on the spinodal dewetting instability of ultrathin metal films has triggered a growth in the thermal dewetting study of metal films, and has led to a number of groups, including our own, focusing on the science of laser-metal interactions to investigate the phenomenon of self-organization and structure formation [42, 43, 12]. One of the most important aspects of ns laser processing of thin films on surfaces is that the high heating and cooling rates can quench in the various intermediate structures during the deformation process. In other words, each laser pulse progresses (and quenches in) the deformation, which can be captured by imaging techniques such as scanning electron microscopy (SEM) or atomic force microscopy (AFM), thus leading to a sequence of pictures, like in a high-speed camera”, that accurately represents the evolution. An example of this is shown in Fig. 1.1 for the case of Ag on SiO₂ substrate [44]. Therefore, pulsed lasers have become a powerful tool in the study of dynamic phenomenon such as dewetting, which we discuss in Sec. 1.3.

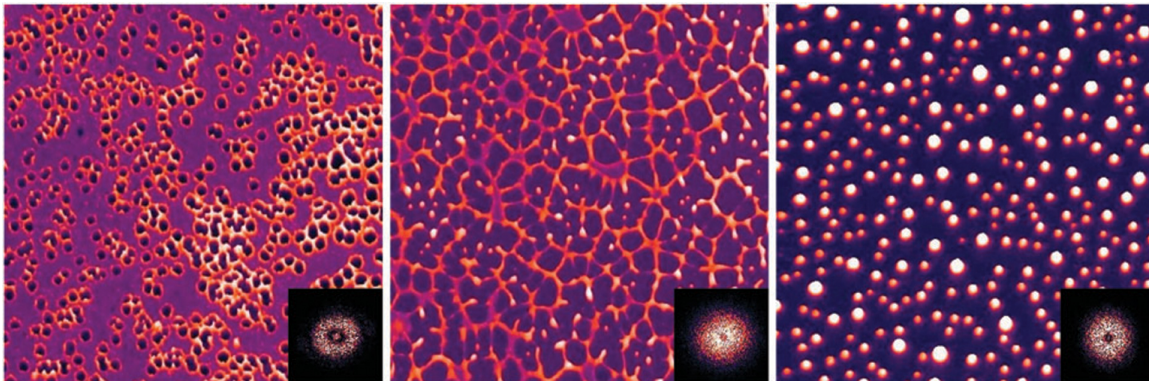


Figure 1.1: *The characteristic nanomorphologies following nanosecond pulsed laser-induced spontaneous dewetting of an ultrathin Ag film on SiO₂ substrates. (left) At early stages of dewetting (irradiation by ~10 laser pulses), holes with a narrow size distribution. (center) Later stage dewetting (~1000 pulses) leads to the formation of polygonal features with a narrow size distribution. (right) The final dewetting state (~10,000 pulses) consists of nanoparticles with a well defined nearest-neighbor spacing. Each image is of dimensions 8 μ m \times 8 μ m. Figures and text taken from ref. [1].*

In this thesis, we have utilized ns pulsed laser irradiation to synthesize nanostructures of semiconductor oxide and metallic materials with controlled size, spacing and shape. Such nanomaterials have many ap-

plications. For instance, increased surface-to-volume ratio shown by semiconductor nanowire arrays over a planar film can provide high sensitivity and selectivity for sensing of toxic and reactive gases [45, 3]. Plasmonic or semiconducting nanoparticles with strong optical scattering and/or fluorescence, incorporated on the surface, can be used for enhancement of solar cell efficiency [23, 24, 20]. Metallic nanomaterials made of combined localized surface plasmon resonance (LSPR) and ferromagnetic materials can realize high sensitivity bio- and chemical-sensors [46, 47, 48]. High aspect ratio magnetic nanowires can be used for data transfer and storage applications [49, 50, 51]. And finally, nanoscale optical biosensors can be based on localized surface plasmon resonance of metallic nanoparticles [52] and nanorods [53].

1.2 Functional Nanostructured materials and techniques

Among the many possible materials and techniques available, this thesis concentrates on two different aspects of the field. One pertains to the investigation of the synthesis of potentially useful materials. In this context, we have studied the synthesis of tin oxide (SnO_2) nanostructured arrays, which have potential applications in hydrogen gas sensing. Another is the synthesis and magnetic characterization of nanowires and nanomagnets of ferromagnetic Co, which is of fundamental interest and has applications in data storage. The other study pertains to the implementation of the Surface Magneto-optical Kerr Effect (SMOKE) technique, which is an important tool to investigate magnetism from surfaces and nanostructures, while also being able to measure magneto-optical Kerr and Faraday rotations, which are potentially useful in optical communication and sensing applications. To test the home-built system, we have studied the Kerr rotation of nanostructures of Co-Ag bimetallic systems, which have potential applications as plasmonic and magneto-optical devices. In the next few sections, we briefly overview some of these applications and the material requirements.

1.2.1 Nanostructured array based gas sensors

The wide variety of electronic and chemical properties of metal oxides makes them exciting materials for basic research and for technological applications. SnO_2 thin films have been of interest for several applications, including in electrode materials, and solar cells and is also known for its excellent gas sensitivity [54]. This is mainly because SnO_2 belongs to a class of oxide materials that have high electrical conductivity [55]. The schematic diagram and plot in Fig. 1.2 depicts the band bending mechanism at the surface when charged molecules attach [Fig. 1.2(a)], leading to changes in the electrical conductance when a sensor is exposed to gases [Fig. 1.2(b)]. Currently, SnO_2 that is doped with various appropriate elements, such as In_2O_3 [56], CuO [57] and Pd [58], is a promising area of research for improved gas sensor performance. In addition, the size and morphology of SnO_2 grains and nanostructures [59, 60] strongly affects their application and therefore appropriately doped and nanostructured SnO_2 can potentially serve as ultrasensitive gas sensors [61].

For gas sensing, a primary motivation to explore the synthesis of well-defined nanostructures is the associated increase in surface-to-volume ratio, which is known to translate into increased functionality of the sensor. In fact, increasing the surface to volume ratio of semiconducting metal oxide nanostructures

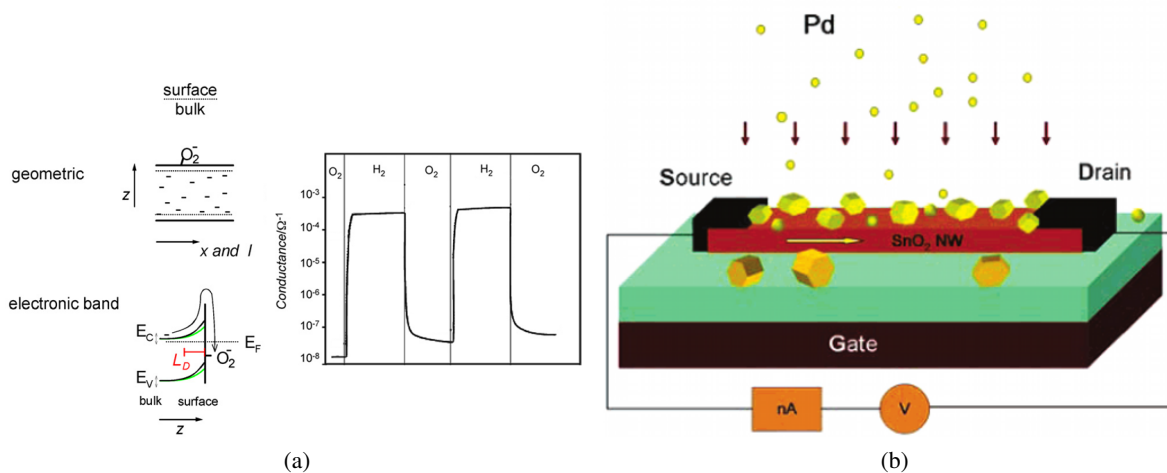


Figure 1.2: (a) (left) Schematic representation of band bending model illustrating adsorption of O_2 at the surface and, (right) variation of the gas sensor's electrical conductance during the alternative exposure to O_2 and H_2 are shown [2]. (b) Schematic view of SnO_2 nanowire based gas sensing device. The wires are covered with vapor-deposited Pd clusters [3].

[Fig. 1.2(b)] make them highly sensitive to surface chemical processes resulting in efficient transduction into electrical signals [3, 45]. One promising architecture is an array of nanowires. This structure will have increased surface-to-volume ratio over the planar films, and is likely to show decrease in the electrical noise, as compared to, for example, a porous type of nanostructure [62]. In addition to the architecture, among polycrystalline gas sensing materials, the grain size plays a major role on sensor functionality, sensitivity, selectivity and reaction time. For instance, the band bending [55], increased surface area of the depletion layer [2], and the enhanced mobility of the free charge carriers [63], are all considered to be caused by the decreased grain size and these effects lead to improved functionality of the sensors [55].

As the use of hydrogen (H_2) gas as an alternative clean energy source is stimulated, accurate and fast detection of the H_2 has become exceedingly important for its safe handling, transportation and operation. Vehicles utilizing domestic fuel cell based cogeneration systems [64], solid oxide fuel cell (SOFC) technology [65], and internal combustion engines [66] are already commercialized H_2 powered systems. Due to its very small size, H_2 is very susceptible to leakage. Since H_2 molecules are quite reactive in the vapor phase, typically about 1-3 vol. % of the H_2 is considered to be explosive, hence, careless treatment can lead to expensive and damaging incidents. Currently, there are several available techniques for measuring H_2 gas concentration, including conductivity changes in pure continuous or porous SnO_2 films [67, 68, 69]. However, there are several challenging issues that remain to be solved, such as the requirements of low working temperature (room temperature and below), fast response and recovery time, as well as high sensitivity and selectivity. The current state of art in the measurement of hydrogen using SnO gas sensors, as outlined by our collaborators at the University at Central Florida, is shown in Fig. 1.3. As is evident, there is a huge gap in the measurement of hydrogen at room temperature and is therefore one of the reasons for our work on SnO_2 arrays.

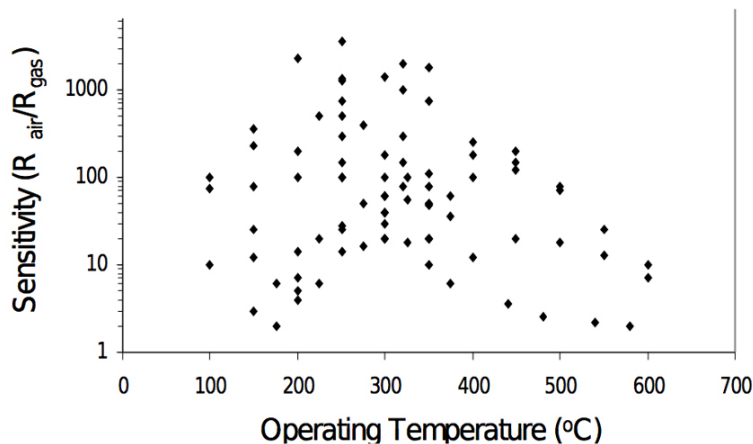


Figure 1.3: *Characteristics of the nanocrystalline SnO₂ based thin film H₂ sensors. Each data point represents reported SnO₂ based H₂ sensor sensitivity at certain operating temperature. The sensors exhibit maximum H₂ sensitivity in the high temperature range (250 to 300°C). [4]*

1.2.2 Magnetic nanostructures

When the size of a magnetic material is decreased to a length scale comparable with the magnetic domain wall or exchange force distance, the material starts exhibiting unusual magnetic behaviors. For instance, well-studied ferromagnetic material like cobalt exhibits unique magnetic properties when it is in the form of nanoparticles. Krishna et al. showed that Co nanoparticles synthesized via pulsed laser treatment exhibit unusual size dependent magnetization [5]. These single domain nanoparticles have the magnetization direction oriented in-plane for the smaller particles (< 75 nm) and out-of-plane for the larger particles (< 180 nm) [5] [Fig. 1.4(a)]. For recording media application, perpendicular recording (using out-of-plane oriented data bit) has several advantages over currently commercially used parallel recording (in-plane), such as high density data storage, high stability, and short bit length [70]. In order to make this technology possible, out-of-plane oriented magnetic data bit with large magnetic anisotropy and greater stability are desired.

Similarly, arrays of nanowires [Fig. 1.4(b)] made from Co with high length to width aspect ratio exhibit large coercivity, large anisotropy and high remanence due to the shape and crystalline anisotropy [6, 71]. Henry et al. showed that the competition between magnetocrystalline and shape anisotropy causes preferential magnetization direction to be either parallel or perpendicular to the wire direction, and this was differentiated by the diameter (~ 50 nm) [6]. In both studies, cobalt was chosen due to its hard magnetic properties, such as high coercivity and magnetization values, large magneto-optic constant, and high Curie point. Ferromagnetic nanowires have potential applications in magnetic MEMS (micro-electric-mechanical-system). Nanowires can be utilized for sensing, manipulating and separating biological cells [72, 73] and these applications require high coercivities and stability at ambient conditions.

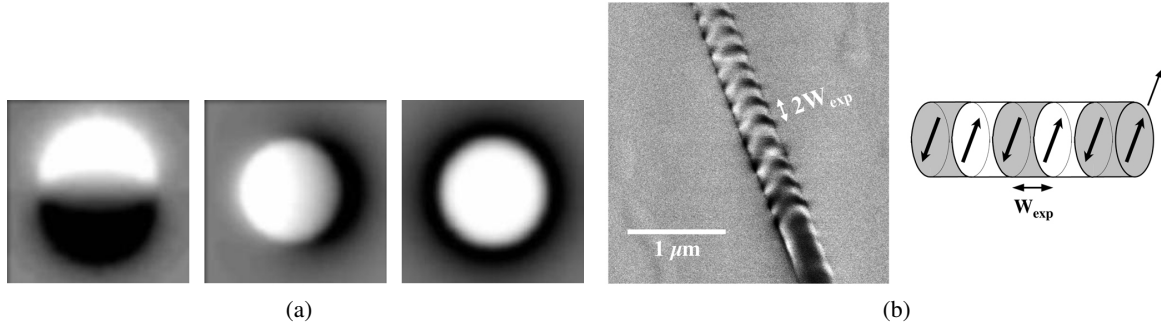


Figure 1.4: (a) The simulated contrast in the MFM images of a single domain ferromagnetic particle with (left) in-plane (0 deg), (center) at an angle of 45 deg and (right) perpendicular to the plane (90 deg) [5], (b) High resolution MFM image of a portion of a Co nanowire, 150 nm in a diameter and (right) possible domain structures [6].

1.2.3 Surface magneto-optical Kerr effect (SMOKE) sensing with plasmonic-ferromagnetic (PF) materials

Enhanced magneto-optical (M-O) Kerr effect sensing with plasmonic-ferromagnetic (PF) material utilizes both surface plasmon resonance (SPR) and magneto-optical (M-O) effects [74, 75, 76, 77]. SPR is the collective oscillation of the conduction electrons [78], and M-O effects are phenomena arising as a result of interaction between light and matter when the latter is under a magnetic field [79]. This hybrid material, i.e. one which could show enhanced M-O effects, was theoretically hypothesized [74, 75, 80, 81] by having SPR and ferromagnetism effects in the proximity of each other. Therefore, SPR materials like Au, Ag, Cu and M-O materials, like Co, Fe, Ni, Fe_2O_3 , YIG, etc. needed to be combined together *without* chemical binding, i.e. as composites rather than as alloys or compounds. From a nanoscale picture, a nanocomposite of SPR and M-O materials can be assumed as a optically homogeneous material if the dimension of the composite structure is smaller than the wavelength of light [80, 82]. The propagation of an electromagnetic wave in such a material can be described in terms of an effective dielectric and magnetic permeability tensor [80]. The theoretical calculations revealed that the diagonal part of the effective dielectric tensor (linked to SPR material) can enhance the strength of magneto-optical effect, which is in the off-diagonal part of the tensor [75, 74]. Hence, such composites exhibit enhanced M-O effects at or near the surface plasmon resonance frequency. Initial work focused on investigations of multilayered SPR and M-O materials prepared by PVD techniques and these showed large M-O enhancement at locations of the surface plasmon [77, 76, 83, 84, 85]. Subsequently, different types of architectures were fabricated, including Au and Co nanosandwiches [47], Ag coated nanoparticles [46], embedded Au particles in YIG medium [86], Au particles on M-O materials [87], and paired SPR and M-O nanoparticles [48, 88].

Among various elemental/material combinations, one suitable candidate for the PF nanoparticle is a mixture of a ferromagnetic metal like Co, with a well suited plasmonic material, like Ag. From the binary phase diagram, Co and Ag is an immiscible system, both in their liquid phase as well as solid phase, and therefore, combining Co with Ag can potentially show controllable ferromagnetic anisotropy as well as strong LSPR effect. Additionally, we found in a recent study that the proximity of Co and Ag within

a nanoparticle could reduce the environmental degradation of Ag, thus permitting more environmentally stable magneto-optical behavior [17].

In this thesis, our focus has been to implement a home-built surface magneto-optical Kerr effect (SMOKE) system. SMOKE is easy implementation and surface sensitive characterization technique. It's a powerful tool to study magnetism of nanostructures. Especially, its usefulness is substantial in the understanding of magnetic anisotropies [89], domain orientation behavior [90] and magnetic switching process [91]. SMOKE operates on the principle of a complex rotation of the plane of polarization of linearly polarized incident light upon reflection from the surface of magnetic material. The rotation is linearly proportional to the magnetization of the material within the probing region of the light. Hence, the measured rotation values as a function of applied magnetic field yields the magnetic hysteresis loops.

1.3 Synthesis of nanomaterials by self-organization and/or self-assembly

Nanostructured self-organization is one of the potential routes to make well-defined nanostructures in a highly repeatable and efficient manner. The self-organizing (SO) or self-assembling (SA) process refers to a broad range of autonomous pattern-forming processes which are commonly seen in physical and biological systems [92, 7]. In self-organizing systems, pattern formation occurs through interactions internal to the system, or in other words, without need for intervention by external directing influences, such as human intervention [7, 92]. Also, SO/SA reflects information coded in shape, physical properties, charge, magnetic dipole, etc. within the individual components. These characteristics determine the interactions among them. In order to reach a final structure, the system goes through certain thermodynamic or kinetic pathways, and eventually stability is obtained with the formation of characteristic patterns. Therefore, nature is able to replicate vast amounts of material repeatedly and accurately in a wide range of scales, from nanometer [size of deoxyribonucleic acid (DNA)] to astronomical units [size of the solar system]. For instance, sand grains assembling into rippled dunes [Fig. 1.5(a)], chemical reactants forming swirling spirals produced by the Belousov-Zhabotinski reaction [8, 93] [Fig. 1.5(b)], cells making up highly structured tissues [94], highly ordered metal nanoparticles of well-defined size and shape made by laser melting [9], and fish joining together in schools [95], are all formed based on SO/SA processes. One of the characteristics relevant to this research is that the SO/SA system also has ability to produce well-defined nanostructures and is therefore viewed as a practical strategy for making large quantities of nanostructures with low cost and high precision [95, 92].

1.3.1 Self-organization by spinodal dewetting

Spinodal dewetting is a robust and predictable approach to making self-organized nanostructures with characteristic size and spacing. A thin liquid film on a non-wetting solid surface is not thermodynamically stable, and so the film can break up spontaneously into a lower energy state comprised of liquid droplets. In daily life, similar phenomena can be observed in numerous occasions like on a car's windshield and on a rain jacket's surface. Interestingly, the liquid droplet formation processes can be seen in the nanoscopic state as well. In general, this whole process of droplet formation is called dewetting. Usually, liquid droplets are

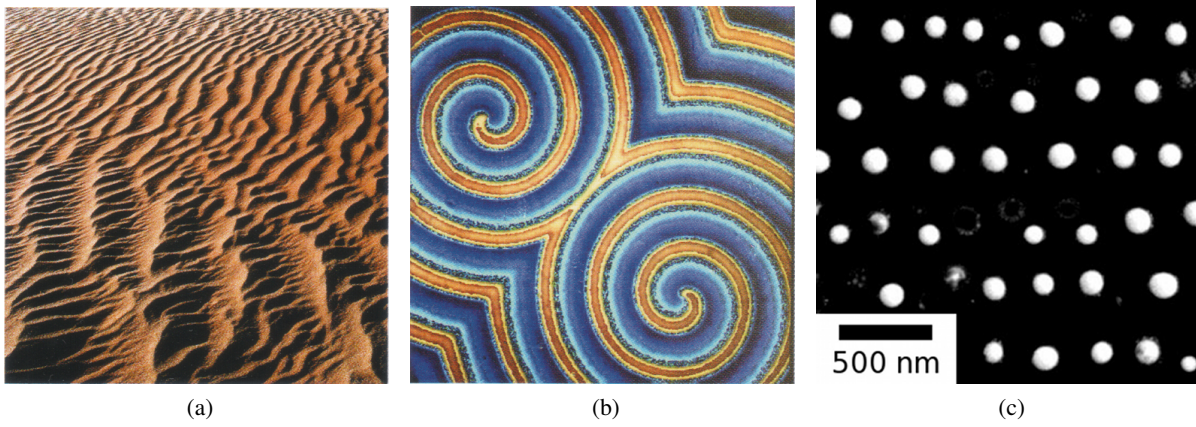


Figure 1.5: (a) Wind-blown ripples on the surface of a sand dune [7], (b) spiral patterns produced by the Belousov-Zhabotinski chemical reaction [8] and (c) Co nanoparticles with well-defined size and shape [9].

formed by overcoming an energy barrier, such as at nucleation sites-like tiny dust particles or other defects on a surface. Due to the inherent randomness of this process, no characteristic length exists in this type of pattern. However, it is also possible for the droplet formation to occur without a nucleation barrier, i.e. spontaneously. In such a case, the dewetting process has been termed spinodal dewetting in analogy to the behavior of the thermodynamic thin film free energy curvature to that of spinodal decomposition of immiscible binary systems [11]. In order to understand the physical origin and mechanism of spinodal dewetting, the theory of dewetting is discussed in the following section.

1.3.1.1 Theory of spinodal dewetting

In the earliest reported studies of spinodal dewetting, Vrij theorized how thin liquid films are influenced by van der Waals and interfacial repulsion forces, and how these forces lead to formation of liquid droplets without requirement of nucleation [96, 97]. He defined that the spinodal dewetting occurs when the system satisfies the spinodal condition of the second derivative of the excess intermolecular free energy with respect to the film thickness, i.e. a negative value of $\partial^2 \Delta G / \partial h^2$ [96]. Sharma incorporated excess free energy per unit area from van der Waals interactions and pressure as:

$$\Delta G = -A/12\pi h^2 + S^P \exp[(d_0 - h)/l] \quad (1.1)$$

where S^P is the polar component of spreading coefficients [98]. Williams, Sharma and Paulsen incorporated van der Waals (intermolecular) interactions to make the generalized disjoining pressure expression or the free energy per unit volume, which is a differentiation of Eq. 1.1, as :

$$\phi = \alpha(d_0^2/h^3) - (S^P/l) \exp[(d_0 - h)/l] \quad (1.2)$$

Vrij further discovered that there are multiple growing wavelengths λ , and characteristic dewetting time scales τ during spinodal dewetting [96]. He related λ to $\partial^2 \Delta G / \partial h^2$ as:

$$\lambda_c(h) = \sqrt{\frac{-2\pi^2\gamma}{\partial^2\Delta G/\partial h^2}} \quad (1.3)$$

and, τ to $\partial^2\Delta G/\partial h^2$ as

$$\tau(h) = \frac{24\gamma\eta}{h_0^3(\partial^2\Delta G/\partial h^2)^2} \quad (1.4)$$

The relations tells us that λ_c and τ vary with respect to the initial film thickness h . Vrij found that among the wavelengths, the fastest growing wavelength, λ_c will dominate the dewetting length scale [96]. Hence he predicted λ_c or the characteristic length scale should be proportional to the square of film thickness, h^2 . Also, he evaluated τ , and showed that the characteristic time scale associated with the growth of the fastest growing wavelength should be proportional to h^5 .

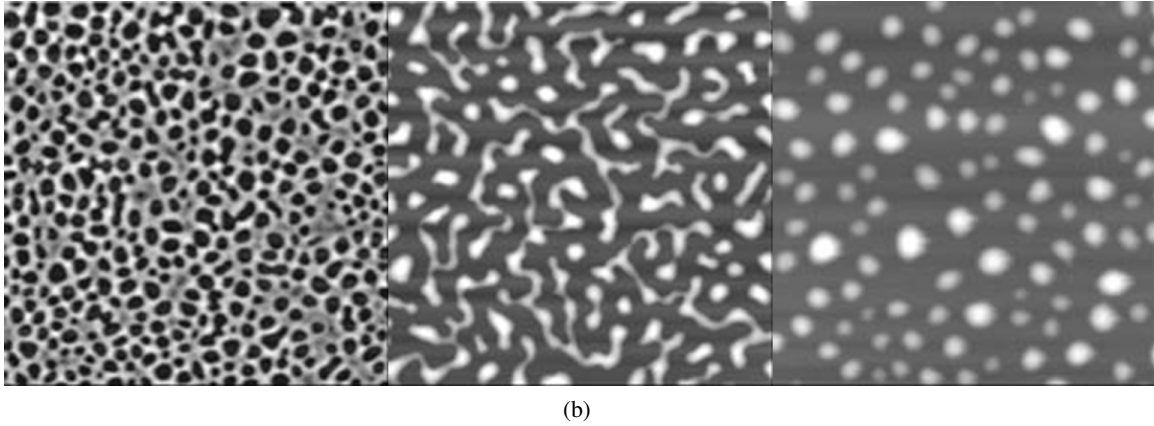
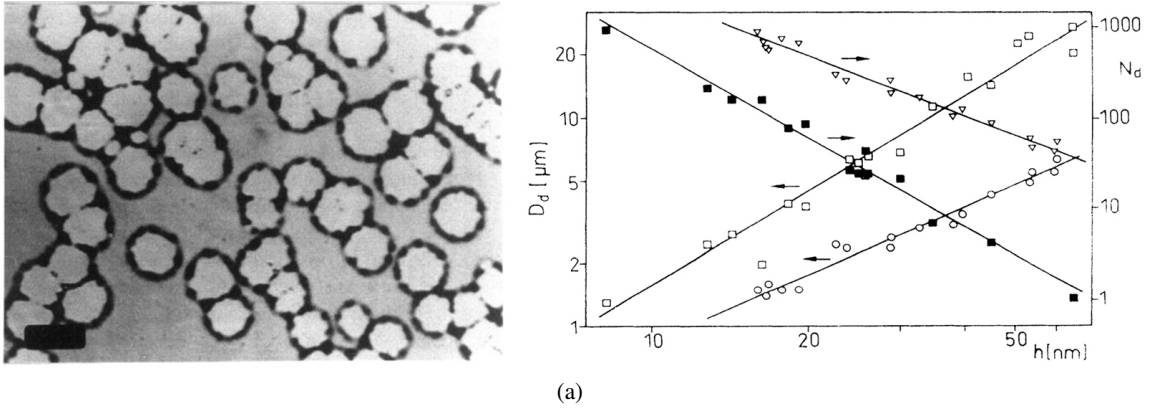


Figure 1.6: (a) (left) Micrographs at the holes state during dewetting of a 40 nm thick polystyrene film on a Si wafer and (right) Double logarithmic plot of the average diameter of particles and the average interparticle spacing (calculated from average number of particles per unit area) as a function of film thickness [10]. (b) Dewetting morphology of a 4 nm PS film on Si wafer as a function of annealing time. (left) Circular holes, (center) holes break up and (right) droplets formation at the end of the dewetting process [11].

1.3.2 Background and/or state-of-art for spinodal dewetting

Experimentally, over the last few decades, the spinodal dewetting system has been examined in both organic and inorganic materials. The dewetting of thin liquid polymer films has been studied extensively for more than three decades [99, 100, 10, 101, 102, 103]. For the first time, Reiter showed that the average hole-hole spacing of polymer liquid films follows h^2 relation which is the characteristic relation of spinodal dewetting [10, 101] [Fig. 1.6(a)]. He studied the influence of the film thickness on dewetting processes using thermally annealed thin polymer films (< 100 nm). Xie et al. further studied dewetting of thin polymer films (< 20 nm) and also confirmed spinodal dewetting [103]. Besides, they found that a transition in the dewetting process with the film thickness < 10 nm [103]. Sharma and Reiter presented well matched theoretical predictions and experimental results for all stages of thin polymer films (< 60 nm) dewetting [100, 102] (Fig. 1.6(b)). On the other hand, studies of the dewetting of liquid metal films started about fifteen years ago [40, 41]. The earliest evidence of spinodal-like instability ($\lambda(h) \propto h^2$) from thin metal films was observed under pulsed laser melting first by Bischof et al. [40] and then by others [104, 43]. Trice et al. showed that because of the nanoscopic nature of pulsed laser heating, under certain conditions, thermal gradient along the interface play a dominant role in the dewetting process [12, 105]. In the metal film cases, patterns similar to those found in polymers have been observed [1] (Fig. 1.1). However, because of the high melting point of metals, thermal annealing, which is the central technique to dewet polymers, cannot readily be applied. In the next subsection, two different types of techniques, pulsed laser irradiation and ion beam induced melting, are discussed in order to study dewetting in metals.

1.3.2.1 Pulsed laser induced Spinodal dewetting (PLiD)

Compared to metals and oxides, polymer thin films have high stability and relatively low melting point, so all morphological stages of dewetting can be studied by thermally annealing films at room temperature. Relatively large length (\sim micrometer) and time (\sim second) scales compared to metals help to study the evolution of morphology. This is due to the thick film thickness and the materials physical properties compared to metals. On the other hand, studying dewetting in metals, semiconductors and metal oxides is challenging due to their high melting point. Additionally, dewetting of these materials under conventional long-time annealing is complicated because various surface processes including metal-substrate chemical interactions and metal diffusion into the substrate can influence dewetting. Solid state diffusion via thermal annealing at below melting point may be one solution. However slow mass transport process is not practical in terms of industrial applications, and as has been shown, solid state dewetting involves fundamentally different mass transport processes, which will lead to different length and time scales [106]. Exploring metal film spinodal dewetting via nanosecond pulse laser heating or ion beam irradiation is an alternate solution. Rapid melting of films minimize unwanted chemical reactions between metal and substrate. Also, because the viscosity of liquid metals is orders of magnitude lower and surface energies are higher than typical liquid polymers, the dewetting time scale would be in the micron- to nano- second range [41]. Hence, short liquid life time per single irradiation (\sim few nanosecond) allows us to examine liquid dynamics of the dewetting process in details.

The dewetting of metal thin film has been studied since mid 1990's [40, 41, 104]. In the initial stage of the study, Bischof et al. deposited Au, Cu and Ni films with thickness ranging from 25 to 50 nm on fused silica substrates with an intermediate layer of less than 2 nm thick Cr. Resulting surface morphology was explored after pulsed laser irradiation on the metal films using Q-switched Nd:YAG laser with 7 ns pulsed width, 532 nm wavelength [41, 40]. From detailed surface roughness analysis using a scanning electron microscope, they found surface undulations at the early stage and holes at a later stage. They observed that the surface undulations as a function h follows spinodal-like instability relation, $\lambda(h) \propto h^2$, and the characteristic wavelength growth time scale follows $\tau(h) \propto h^5$ relation [40]. From the free energy analysis, they also confirmed the second derivative of the effective potential was negative, $\partial^2 \Delta G / \partial h^2 < 0$, which was a necessary condition for spinodal dewetting [41].

Ion beam induced metal and semiconductor films dewetting has been studied by Cahill et al. [107, 108, 109, 110, 111]. Nanopattern formation upon irradiation of films as a function of the number of ions were studied. In contrast to typical methods to induce dewetting (films are heated homogeneously, and dewetting occurs over large areas), irradiation with ion beams leads to a different kind of heating. Accelerated individual heavy-ion strikes on the films, and ion-phonon coupling leads to heat the materials far above their melting temperatures. Such heating is highly localized both in space (\sim nanometer) and time (\sim picoseconds) [107]. The maximum size of this locally melted area (molten zone) varies from ion to ion, i.e. in the case of 800 keV Kr^+ incident on Pt films, the average molten zone size was \sim 5 nm [107]. Upon melting, a radial temperature gradient is built up, which also establishes a gradient in the surface tension γ from the dependence of γ on temperature. The combination of the ion-imparted momentum and the surface tension gradient in the molten zone drives mass transport [107]. Therefore, the observed dewetting is either heterogeneous with a lateral size distribution of dry patches, presumably due to nucleation and growth, or homogeneous with a characteristic lateral size. Since the amplification of surface fluctuations requires that the lateral dimension of the fluctuated homogeneous liquid film be larger than the fluctuation wavelength [96], spinodal dewetting may not be applicable to ion-induced dewetting when the molten zone size is in the range of a few nanometers [108].

In summary, nanosecond (ns) pulsed laser melting has demonstrated that it is a well-suited approach to study dewetting of metal films compared to ion beam induced melting. In the following subsection, a detailed study of thin metal film dewetting, specifically in the range of 2 to 20 nm film thickness is discussed, which results in nanostructures with size in the range of 10 to \sim 100 nm.

1.3.2.2 Thin metal film dewetting: $2 < h < 20$ nm

Pulsed laser induced spinodal dewetting of thin films has been studied extensively [12, 43, 104]. Favazza et al. explored dewetting of metal films with thickness ranging from 2 to 20 nm. They explored the resulting morphology in terms of characteristic intermediate hole-hole spacing, inter-particle spacing and particle diameter as a function of initial film thickness. In the experiments, several different thick metal films were deposited on SiO_2 substrates primarily by physical vapor deposition (PVD) techniques, such as e-beam or pulsed laser deposition. After the pulsed laser irradiation of the films, the resulting morphologies were studied. As was observed in the polymer dewetting and metal films (thickness: 25 to 50 nm) dewetting

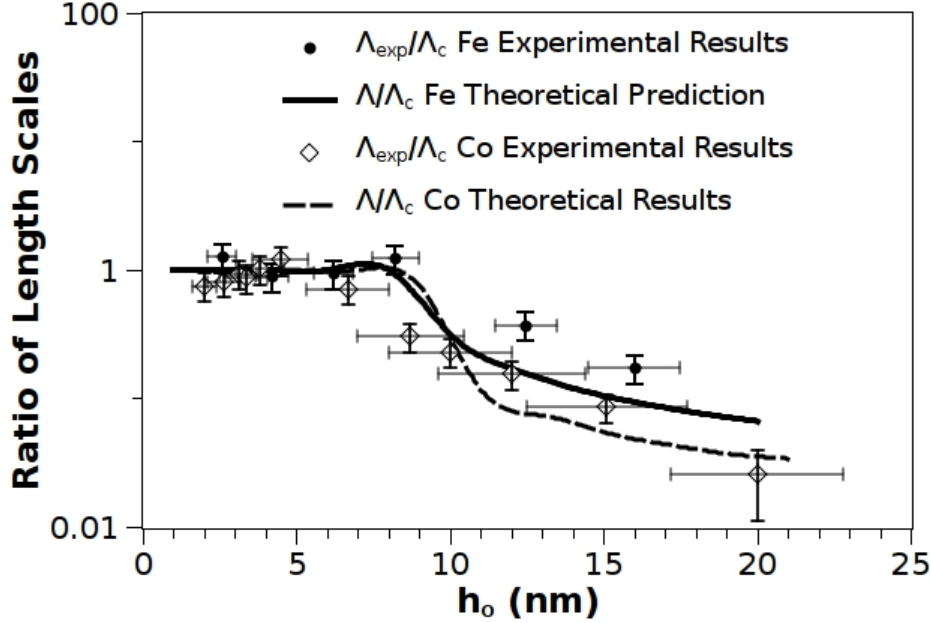


Figure 1.7: Comparisons of characteristic pattern length scales for Co (dashed line) and Fe (solid line) film on SiO_2 . The symbols represent the ratio of the experimentally measured nearest-neighbor spacing Λ_{expt} to the spinodal length scale Λ_c . The lines represent the ratio Λ/Λ_c , where Λ is the predicted length scale in the presence of intrinsic thermocapillary effects. For Co film thickness < 9 nm, Λ_{expt} increases $\sim h^2$ consistent with spinodal dewetting, however for thickness ≥ 9 nm case Λ_{expt} decreases sharply with increasing h . Taken from ref. [12].

systems, the formation of an array of nanoparticles with a monomodal size distribution and short range spatial order in the nearest neighbor spacing were observed in the liquid metal films (thickness: 2 to 20 nm) dewetting systems [43, 112]. In the thin metal film dewetting system, the size and spacing of the nanoparticles dependence on the initial film thickness were shown with the particle radius and spacing varying as $h^{5/3}$ and h^2 [43, 112]. One of the major findings of this previous work was the discovery of novel effects related to the thickness-dependent heating of the films. Specifically, a reduction in the particle spacing with increasing h was observed for Co and Fe films, as shown in Fig. 1.7. This was attributed to the thickness dependence of laser heating arising from thickness-dependent optical reflectivity and the heat sinking into the substrate, which resulted in intrinsic thermocapillary effects along the plane of the substrate [105, 12]. This work clearly indicated that ns pulsed laser processing can often produce new and unexpected results, as will also be shown in this thesis.

1.4 Outline of Dissertation

- Chapter 2: Thickness dependent self limiting 1-D tin oxide nanowire arrays by nanosecond pulsed laser irradiation

An experimental study of the synthesis and characterization of 1-D SnO₂ periodic nanostructures via pulsed laser processing technique is presented. Two beam laser interference irradiation was performed on SnO₂ films on SiO₂ substrates. The resulting surface morphology was characterized by SEM and AFM. Experimental observations combined with theoretical modeling of the thermal behavior of the thin film under laser irradiation was used to explain the mechanism of nanostructure formation. In collaboration with the University of Central Florida, these SnO₂ samples were used to measure sensitivity to hydrogen gas detection. The sensor results showed improved sensitivity, selectivity and response time over the planar SnO₂ thin film.

- Chapter 3: *Thermodynamic modeling of thin metallic liquid films dewetting*

In the studies of dewetting instabilities, insight into the nature of fluid flow as well as the energy pathway is critical. We have applied an energy rate approach to describe the case of isothermal and non-isothermal dewetting, i.e. in which film thickness dependent Marangoni effect or thermocapillary forces are also present. Specifically, within the energy rate analysis, the rate of thermodynamic free energy decrease due to film thickness fluctuations is balanced by the rate of energy loss due to viscous dissipation. This approach permits a rapid analysis of the dewetting length scales for classical spinodal dewetting as well as for dewetting with thickness-dependent Marangoni effects.

- Chapter 4: *Implementation and testing of a home-built SMOKE system for up to 0.7 T field measurements.*

In this chapter, we first discuss the successful implementation of a SMOKE system built in-house. Subsequently, to test the system, we measured the Kerr rotation from nanostructures of the Co-Ag system in various geometries and shapes. This included measurements from bilayer films, co-deposited composite films and nanoparticles. The co-deposited film showed higher Kerr rotation (6×10^{-3} degrees) than the bilayer structures with same effective amount of Co and Ag. Furthermore, nanoparticles showed a factor of 2 or higher Kerr rotation than composite films of similar Co composition ranging between 35 to 100%.

- Chapter 5: *Magnetic properties of Co nanowires and nanoparticle arrays synthesized by pulsed laser melting*

Previous investigations of ferromagnetic nanoparticles by our group has focused on synthesis of nanoparticles by nanosecond laser dewetting. Those studies demonstrated that the resulting nanoparticles show unusual magnetic anisotropy behaviors [5, 113]. Here, we have focused on the shape dependence of the magnetic behavior of Co nanostructures prepared by nanosecond laser interference technique. First, Co nanostructures of various shapes, including nanowires (high in-plane aspect ratio), nanorods (medium in-plane aspect ratio), and nanoparticles (in-plane aspect ratio of 0.5) were prepared by laser interference processing and the Rayleigh instability. Subsequently the mag-

netic domain and magnetization reversal behavior of these structures were studied using Surface magneto-optic Kerr effect (SMOKE) and magnetic force microscopy (MFM). Multidomain features as well as large anisotropy were observed. We concluded that shape anisotropy was primarily responsible for the magnetic behaviors.

- Chapter 6: *Summary and future work*

A summary of the main results of this dissertation as well as some potential future directions of research pertaining to hydrogen sensing and magneto-optical sensing is discussed.

Chapter 2

Thickness dependent self limiting 1-D tin oxide nanowire arrays by nanosecond pulsed laser irradiation for hydrogen sensing

(Reported to Nanoscale vol. 3, 1090 (2011))

2.1 Summary

Fast, sensitive and discriminating detection of hydrogen at room temperature is crucial for storage, transportation, and distribution of hydrogen as an energy source. One dimensional nanowires of SnO₂ are potential candidates for improved H₂ sensor performance. The single directional conducting continuous nanowires can decrease electrical noise, and their large active surface area could improve the response and recovery time of the sensor. In this work we discuss synthesis and characterization of nanowire arrays made using nanosecond ultraviolet wavelength (266 nm) laser interference processing of ultrathin SnO₂ films on SiO₂ substrates. The laser energy was chosen to be above the melting point of the films. The results show that the final nanowire formation is dominated by preferential evaporation as compared to thermocapillary flow. The nanowire height (and hence wire aspect ratio) increased with increasing initial film thickness h_o and with increasing laser energy density E_o . Furthermore, a self-limiting effect was observed where-in the wire formation ceased at a specific final remaining thickness of SnO₂ that was almost independent of h_o for a given E_o . To understand these effects, finite element modeling of the nanoscale laser heating was performed. This showed that the temperature rise under laser heating was a strong non-monotonic function of film thickness. As a result, the preferential evaporation rate varies as wire formation occurs,

eventually leading to a shut-off of evaporation at a characteristic thickness. This results in the stoppage of wire formation. This combination of nanosecond pulsed laser experiments and thermal modeling shows that several unique synthesis approaches can be utilized to control the nanowire characteristics.

2.2 Introduction

As the use of hydrogen (H_2) gas as an alternative clean energy source is stimulated, accurate and fast detection of the H_2 will become exceedingly important for its safe handling, transportation and operation. Vehicles utilizing domestic fuel cell based cogeneration systems [64], solid oxide fuel cell (SOFC) technology [65], and internal combustion engines [66] are already commercialized H_2 powered systems. Due to its very small size, H_2 is very susceptible to leakage. Since H_2 molecules are quite reactive in the vapor phase, typically about 1-3 vol % of the H_2 is considered to be explosive, hence, careless treatment can lead to expensive and damaging incidents. Thus, precise control of the gas is essential, especially via detection of leaks. Currently, there are several available techniques for measuring H_2 gas concentration, including conductivity changes in pure continuous or porous SnO_2 films [67, 68, 69] and in TiO_2 nanotubes arrays [114, 115], measurement of surface plasmon resonance utilizing palladium [116], using the Schottky effect in Pt-Carbide [117] and carbon nanotubes decorated with Pd nanoparticles. However, there are several challenging issues that remain to be solved, such as the requirements of low working temperature (room temperature and below), fast response and recovery time, as well as high sensitivity and selectivity.

SnO_2 thin films have been of interest for several applications such as transistors, electrode materials, and solar cells and is also known for its excellent gas sensitivity [54]. SnO_2 doped with various appropriate elements, such as In_2O_3 [56], CuO [57] and Pd [58], is a promising area of research for improved gas sensor performance. This type of doping generates an excess concentration of lattice oxygen-ion vacancies and decreases the concentration of free electrons to maintain the charge balance. In addition, the size and morphology of SnO_2 grains and nanostructures [59] strongly affects their application and therefore appropriately doped and nanostructured SnO_2 can serve as ultrasensitive gas sensors [61]. In this paper, we explore the synthesis of arrays of one dimensional (1-D) nanowires of SnO_2 , with the eventual goal of fabricating In_2O_3 -doped SnO_2 , which is a potential candidate for improved H_2 sensor. The doped In^{3+} cations are effective in increasing the number of active surface area sites enabling the sensor to detect H_2 at lower operating temperatures.

A primary motivation to explore the synthesis of well-defined nanostructures is the associated increase in surface-to-volume ratio, which is known to translate into increased sensitivity, selectivity and response speed of the H_2 sensor [55]. Another potential advantage of an array of continuous nanowires is a decrease in the electrical noise, as compared to, for example, a porous type nanostructure [118]. Here we focus on synthesis and characterization of arrays made from thin films of pure SnO_2 on SiO_2 substrates by use of nanosecond pulses of ultraviolet (UV) wavelength (266 nm) laser. Pulsed laser interference irradiation is a well-known means of creating a well-defined and spatially periodic but transient surface temperature profile [119, 120, 121]. For appropriate energy densities, the film can be locally evaporated or melted, with the liquid being subject to strong thermocapillary forces under the thermal gradients. As a result, a periodic structuring of the film material can take place. For irradiation with nanosecond pulses, the heating and cooling rates

are extremely large [104, 105] and as a result, the morphology changes occurring in the liquid phase can be rapidly quenched, resulting in periodic structures [9]. However, as has been shown recently, nanoscale effects strongly influence the UV laser heating of very thin films, often resulting in unusual and unexpected effects on morphology evolution [12, 44]. Here we have utilized a thermal model based on finite element analysis that accurately accounts for the nanoscale thickness dependent optical and thermal behavior of the film-substrate system in order to predict the thermal behavior of the films. By comparison with experimental observations of melting and array formation, a reliable model for the mechanism of nanowire array formation was established. The nanowire formation was dominated by preferential evaporation. We also observed experimentally that the final effective thickness of SnO₂ remaining after array formation was nearly constant for various starting film thickness at a given laser energy density. This self-limiting effect was due to the strong thickness-dependent temperature of the film under laser irradiation for any given energy density. As a result, thermal evaporation and thermocapillary flow can both shut down as the film morphology evolves. Other features of the nanowire morphology, including nanowire height and aspect ratio were found to increase with increasing film thickness and laser energy. These results are qualitatively consistent with the thermal model result based on the temperature difference between the regions of interference maxima and minima. The experimental and supporting theoretical modeling results permits selection of the appropriate thin film and laser parameters to achieve desired nanowire morphology characteristics.

2.3 Experimental Procedure

Thin films of SnO₂, with thickness between 5 to 100 nm, were deposited onto 400 nm thick thermally grown SiO₂ on Si wafers and quartz wafers by pulsed laser deposition (PLD). The substrates were ultrasonically rinsed and dried in air prior to use. Deposition was performed under ultrahigh vacuum (UHV) conditions, at a base pressure of 10⁻⁷ Torr, with the substrate at room temperature. SnO₂ slugs (99.9% purity, obtained from CERAC, inc.) were used as PLD targets. Thickness of the as-deposited films was measured by performing atomic force microscopy (AFM) on a step-height region generated by the application and subsequent removal by acetone of a nitrocellulose mask. Besides, AFM analysis yielded a maximum RMS roughness of the as-deposited films of 0.3 nm. Energy dispersive X-ray spectroscopy (EDS) measurements were employed to determine the relative concentration of Sn within the electron interaction zone. The resulting concentrations were then fitted on an exponential curve, so that subsequent measurements of the effective thickness of the laser irradiated films could be determined from the EDS measurements. The optical properties of the as-deposited films were measured by an Ocean Optics HR2000+ spectrometer in order to obtain the accurate complex refractive index for the deposited films, which are known to differ from bulk values [122].

Laser processing was performed with the 4th harmonic (266 nm wavelength) of an Nd:YAG laser, with a 9 ns pulse width and a repetition rate $f = 50$ Hz. All the results presented here are based on irradiations done under ambient conditions. First, the melt threshold energy for various SnO₂ film thickness (5 and 42 nm) was obtained by normal incidence single beam irradiation with 3000 pulses at various laser energy densities, E_o . The melt threshold was defined as the minimum energy required to show a substantial morphology change to the surface of the film after substantial irradiation times, as has been done in the past [105].

This morphology change was evidenced in a scanning electron microscope (SEM). These measurements enabled a quantitative comparison of the experimentally determined melting energy with the finite element model for laser heating of the films. Based on the melt threshold energies determined by single beam experiments, two-beam laser irradiation was performed for nanowire array synthesis. The laser beam was split into two equal energy beams using a 50-50 beam splitter and were incident on the sample at inclusive angle, θ_i , of 72° (and 86°) with a resulting theoretical interference fringe spacing of 224 nm (and 195 nm) respectively. Approximately 3000 pulses were applied in order to produce an array of wire-like features within the irradiated area. The resulting film morphology was characterized by SEM (using either a Hitachi S4300N or a Gemini: LEO 1525), AFM in a Nanonics MultiView 1000, and by EDS measurements in the LEO 1525. The elemental compositions of select samples were also characterized by X-ray photoelectron spectroscopy (XPS) using a Physical Electronics (PHI5400 ESCA) spectrometer with a monochromatic Al $K\alpha$ X-ray source operated at 300W. The crystal structures of select samples were characterized by x-ray diffractometry (XRD) using a Rigaku D/MAX RAPID II microdiffractometer with a curved imaging plate and a rotating Cr anode operating at 35 kV and 25 mA.

2.4 Results

2.4.1 Nanostructured arrays morphology

Fig. 2.1(a) shows the SEM image of an SnO₂ nanowire array synthesized from SnO₂ films of initial thickness $h_0 = 42$ nm and at an energy density of 300 mJ/cm^2 with $\theta_i = 72^\circ$ degrees. This and similar SEM micrographs were used to analyze the average spacing Λ_{av} of the nanowires in the array. Also, EDS measurements performed over large portions of the array, $\sim 100 \mu\text{m}^2$, were used to estimate the remaining amount (h_{rem}) of SnO₂ in the array. In order to quantify h_{rem} value, the weight percentage of Sn per unit area with varying thickness of as-deposited SnO₂ film was calibrated. The EDS measurement parameters, such as the acceleration voltage (10 kV), the probing area ($\sim 100 \mu\text{m}^2$), the processing time (200 seconds) and the substrate (400 nm thick SiO₂ layer on Si wafer), were fixed. Fig. 2.2 shows areal density of Sn (wt. $\%/\mu\text{m}^2$) with respect to SnO₂ film thickness (nm). From comparison between the exponential and linear fit curves, the exponential curve agrees with overall trend of the experimental data. Fig. 2.1(b) shows the AFM image of the same sample for which the SEM image is shown in Fig. 2.1(a) is shown. AFM was performed to extract the topographic information of the wires, from which line profiles, such as shown in Fig. 2.1(c), were extracted. From such line profiles, the average nanowire height h_{nw} was measured as the value between the peak to trough of the nanowires averaged over large portions of the array.

2.4.2 Crystal and chemical bonding properties

The surface elemental composition of the SnO₂ before and after laser processing was evaluated using XPS. In Fig. 2.3, XPS spectra of Sn $3d_{5/2}$ measured on the as-deposited SnO₂ film of thickness 42 nm and nanowires synthesized at a laser energy density of 300 mJ cm^{-2} from the 42 nm film are shown. The photoemission intensity peaks occur at 486.46 and 486.57 (eV) respectively, for the two surfaces, and this corresponds well to the Sn⁴⁺ binding energy component of stoichiometric SnO₂, which is at 486.3 eV [13]. The Sn $3d_{5/2}$ peak for SNO is 0.5 eV lower than the SnO₂ peak and we did not observe this peak shift in

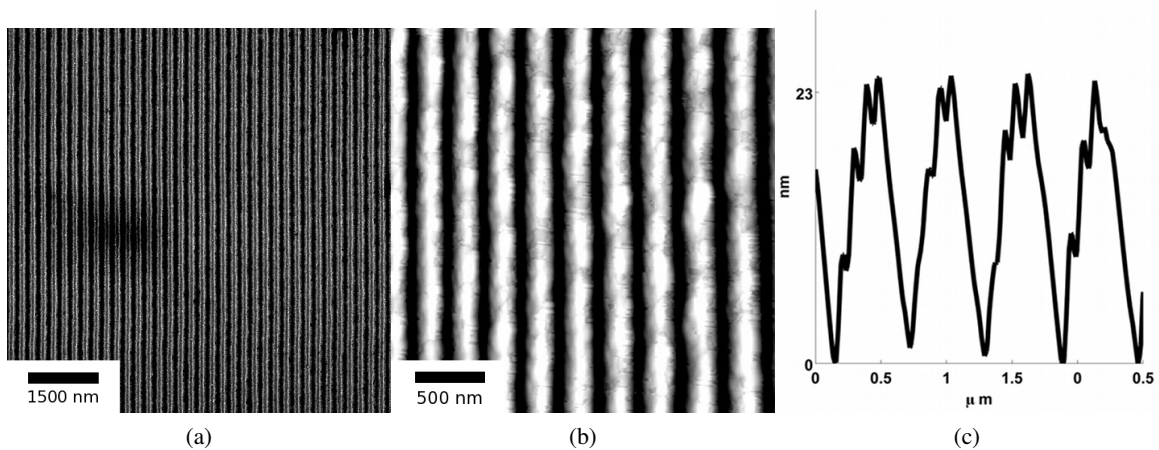


Figure 2.1: (a) SEM images of SnO₂ nanowires synthesized from a 42 nm film at 300 mJ cm⁻² and an interference angle of 72°. SnO₂ rich and poor regions correspond to bright and dark contrasts, respectively. The average nanowire spacing is 232.3 nm while average width was estimated to be 97 nm. (b) AFM topography image of SnO₂ nanowires of the same sample as (a). (c) A typical AFM line profile of the nanowires of (b). From such line profiles, the average nanowire height, h_{nw} , could be calculated, and in this case it was 16 nm.

the nanowires sample. This suggests that upon irradiation of the as-deposited SnO₂ films, the formation of nanowires is not assisted by valence change, and thus the nanowires remained as SnO₂.

The crystal structure of the samples before and after the irradiation was evaluated by glancing angle XRD. The XRD equipped with a curved imaging plate and a rotating Cr anode operating at 35 kV and 25 mA. An optical prefix consisting of horizontal and vertical mirrors specific to Cr K_α radiation was employed in the incident beam to provide a focused x-rays at the sample position. At the end of the incident beam path, a 0.3 mm collimator was used to optimize the resolution and signal to noise ratio of the diffraction patterns. The incident beam path from x-ray generator to the collimator was protected by o-ring sealed tubing that was purged with Helium gas to improve the x-ray flux at the sample position. The samples were mounted on a stainless steel sample holder with the x-ray beam 2° off axis from the plane of the sample. JADE 8.5 from Materials Data Inc., and PDF4+ database from ICSD were used to analyze x-ray diffraction data. Fig. 2.4(a) and (b) shows the background subtraction XRD data of the nanowires synthesized from a 42 nm film and an as-deposited SnO₂ film of thickness 42 nm, respectively. Analysis of the nanowire sample indicated a polycrystalline tetragonal crystal structure with lattice parameters of $a = 4.78$ and $c = 3.21$, but the initial SnO₂ film was found to be single crystal in nature, since only the (110) and (220) peaks of SnO₂ appeared in the XRD scans. No change in the lattice parameter was found between the two samples. From the Scherrer equation, $B(2\theta) = \frac{0.94\lambda}{L\cos\theta}$, the average grain size at (110) orientation for film: $L_{avg} = 53nm$ and NSA: $L_{avg} = 18nm$ were calculated. B and θ represent peak width and angle in XRD spectrum, respectively. λ is x-ray wavelength, and L is crystallite size. From the XRD spectrum in Fig. 2.4, full width at half maximum (FWHM) of (110) orientation diffraction peaks of both film and NSA were obtained. From the calculation, there was approximately 65% decrease in the average grain size of NSA from film.

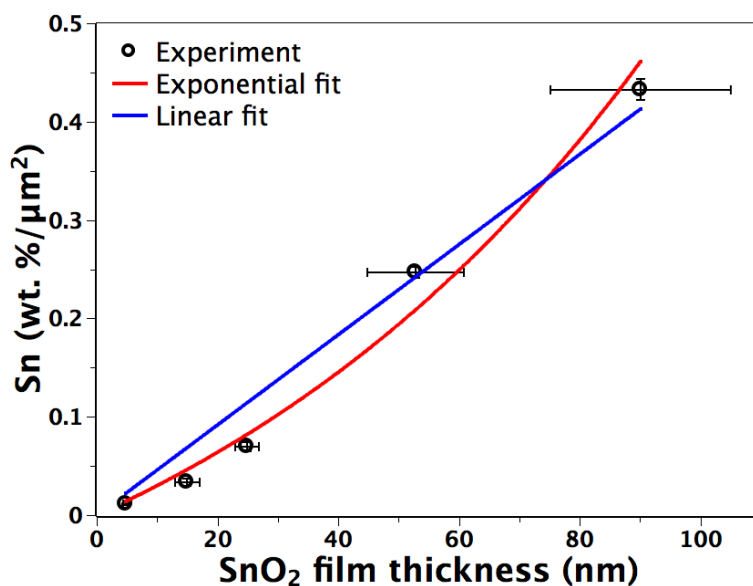


Figure 2.2: EDS (Energy-dispersive X-ray spectroscopy) measured areal density of Sn (wt. %/μm²) with respect to as-deposited SnO₂ film thickness (nm). The exponential growth fit (red) and linear fit (blue) curves are shown.

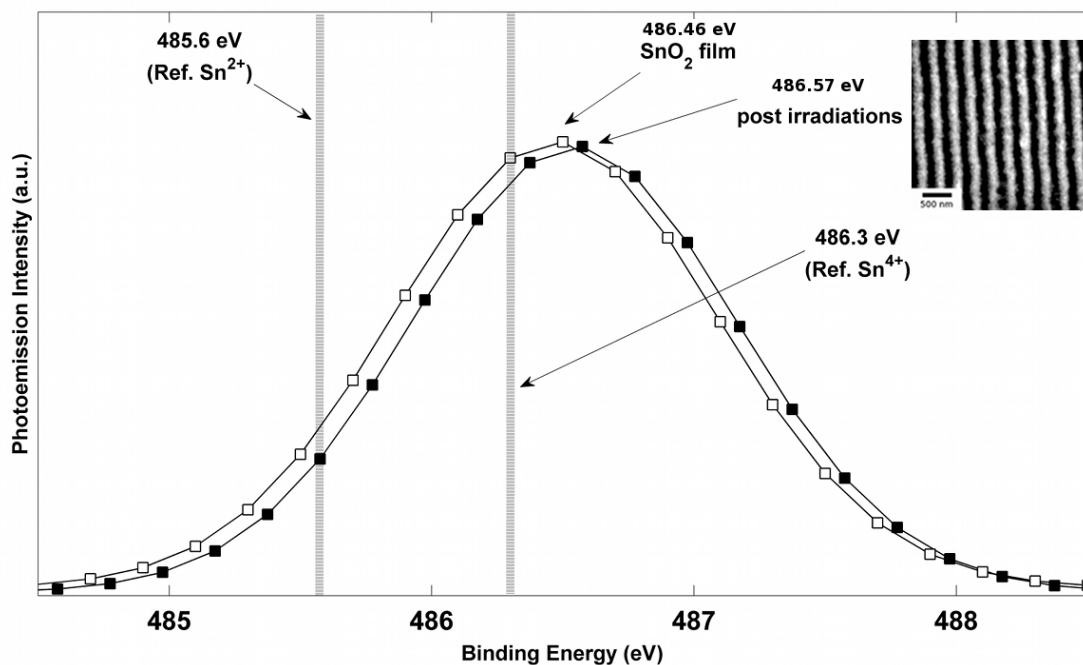


Figure 2.3: XPS (X-ray photoelectron spectroscopy) spectra of Sn 3d_{5/2} measured on SnO₂ film and nanowires. The film (line with open symbols) and nanowires (line with closed symbols) photoemission intensity peaks of, 486.46 and 486.57 (eV) respectively, correspond with the binding energy of Sn⁴⁺ component, which is 486.3 (eV) [13]. Inset shows SEM image of nanowire region from which XPS was measured.

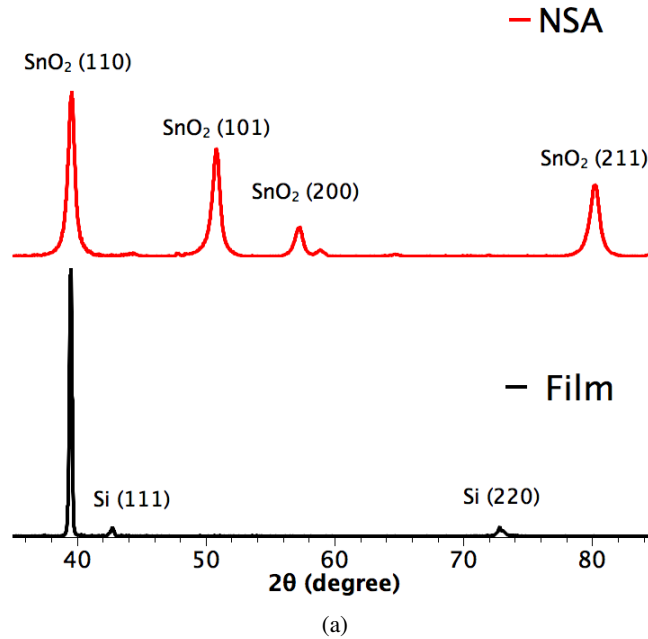


Figure 2.4: XRD spectra with the background removed of an SnO_2 (top) NSA sample with low index reflections of SnO_2 identified, where the relative intensity of the reflections indicate a tetragonal polycrystalline structure of $a = 4.78 \text{ \AA}$ and $c = 3.21 \text{ \AA}$. (bottom) film sample, which indicates a single crystalline tetragonal structure due to the lack of SnO_2 reflections beyond (110) and (220).

2.4.3 Understanding formation mechanism of NSA from films

2.4.3.1 Initial film thickness dependence

The quality of nanowires, or equivalently, its quantitative morphological characteristics given by h_{nw} , h_{rem} , and the aspect ratio given by $AR = h_{nw} \Lambda_{av}^{-1}$, was next investigated as a function of initial film thickness h_o for various laser energy densities E_o . In Fig. 2.5, SEM images of the nanowires formed from two different h_o values but from similar E_o (308 mJ cm^{-2}), interference angle (72°) and number of pulses (3000) are shown. A clear difference in morphology can be seen between the two arrays with films of larger h_o producing a more well defined nanowire structure. In Fig 2.6, the AFM measurements and typical line scans of the wire profile for three different h_o values prepared with above energy and interference conditions are shown. The average nanowire height, h_{nw} , was obtained by averaging over 128 consecutive line scans, corresponding to a length of 375 nm, over 7 nanowires. The, h_{rem} was measured using EDS over an area of $100 \mu\text{m}^2$ (or approximately 50 wires) at a location corresponding to the AFM measurements. The results of these measurements are shown in Fig. 2.7 for the various thicknesses. Fig. 2.7(a) corresponds to the average h_{nw} (open symbols correspond to experimental measurements) while Fig. 2.7(b) is the remaining film thickness h_{rem} . Fig. 2.7(a) clearly shows that h_{nw} , and therefore the aspect ratio of the wire increases with increasing initial film thickness h_o . This behavior is especially important from viewpoint of maximizing the effective surface area for use in sensor applications. On the other hand, Fig. 2.7(b) shows that the final

amount h_{rem} of SnO_2 is 14 ± 1 nm, which is substantially lower than the starting thickness. This clearly points to a large contribution from evaporation for the wire synthesis. More interesting however, is the little dependence of h_{rem} on the initial thickness h_o for processing at a constant laser energy density E_o . Nanowires derived from films that undergo substantial evaporation ($h_o \gg h_{rem}$), such as Figs. 2.6(b) and (c), yield a continuous nanowire structure, but samples produced where evaporation was negligible ($h_o \approx h_{rem}$), Fig. 2.5 (b), show inconsistencies that may include the formation of clusters of nanoparticles. One important observation on the synthesis of nanowires is its dependence on the number of laser pulses. While the dependence on film thickness (and energy, which is discussed next) was performed at a fixed number of pulses (3000), the actual final state of the wires is typically formed at a much shorter number of pulses. In other words, the wire formation appears to stop very early in the irradiation and further irradiation does not result in any changes to the wire characteristics. Therefore, following 3000 pulses the morphology is in a stable state and does not progress further. This observation points to a self-limiting or self-stopping mechanism, where the wire formation ceases due to intrinsic conditions.

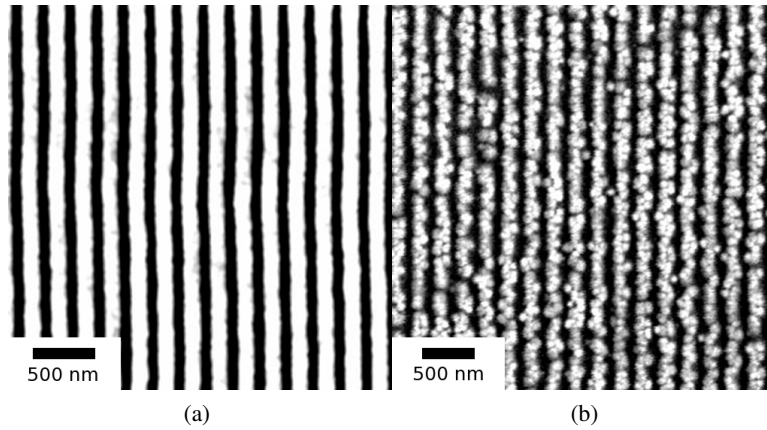


Figure 2.5: SEM images of SnO_2 nanowires formed from two different initial film thickness (a) $h_o = 90$ nm and (b) $h_o = 15$ nm using the same interference angle, $\theta_i = 72^\circ$ and 3000 pulses at an energy density of 308 mJ/cm^2 . The average nanowire spacing of (a) and (b) are 221 nm and 216 nm respectively.

2.4.3.2 Laser energy density dependence

Next, we investigated the dependence of nanowire morphology on the laser energy density (between 440 to 700 mJ/cm^2) for films of a fixed thickness ($h_o = 42$ nm), irradiated using the same interference angle of $\theta_i = 86^\circ$ degree, and with 3000 laser pulses. In Fig. 2.8(a) and (c) SEM images of the nanowires formed from E_o values of 440 and 535 mJ cm^{-2} respectively, are shown. In Fig. 2.8(b) and (d), magnified SEM images corresponding to (a) and (c) respectively, are shown. In Fig. 2.9 the AFM and line profiles corresponding to 440, 535 and 700 mJ cm^{-2} energy density values are shown. In Fig. 2.10(a) and (b), the h_{nw} and h_{rem} are shown, respectively, as a function of E_o . The wire height was found to increase with increasing energy density [Fig. 2.10(a)]. Higher irradiation energy densities were also found to consistently produce a more

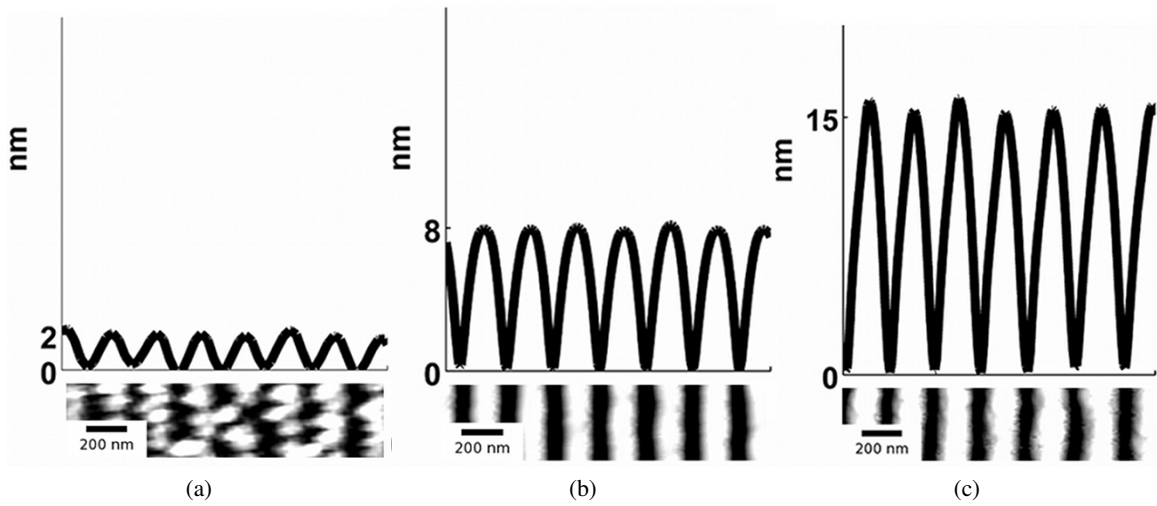


Figure 2.6: AFM topography image and line scans of the wire profile of SnO_2 nanowire arrays formed from three different initial film thickness, (a) $h_0 = 15$, (b) $h_0 = 25$ and (c) $h_0 = 90$ nm respectively. The SEM images of the sample $h_0 = 15$ and 90 nm are shown in Fig 2.5. All three nanowires were synthesized using the same interference angle, $\theta_i = 72^\circ$ and 3000 pulses at an energy density of 308 mJ cm^{-2} . The average nanowire height of each sample is (a) $h_{\text{nw}} = 2$, (b) $h_{\text{nw}} = 8$ and $h_{\text{nw}} = 15$ nm.

nanowire structure with clusters of nanoparticles, such as that of 2.8(d) in contrast to the lower energy density case, (b). Again, this a useful result as it shows that E_0 can be used as an experimental control parameter in the synthesis of wires with different morphology. Also, the remaining film thickness was found to decrease with increasing energy density [Fig. 2.10(b)].

Based on the SEM and AFM results presented above, one can conclude some general aspects about the mechanism of nanowire synthesis. First, evaporation appears to be playing an important role in the synthesis, as is evident from the lower film thickness remaining following the processing [Fig. 2.7(b) and Fig. 2.10(b)]. This observation of large evaporation is also important in the context of the chosen energy densities, which were close to the melt threshold energy of the SnO_2 films. Secondly, the wire height (and aspect ratio) increase with increasing initial film thickness as well as increasing energy density. Finally, the self-limiting effect on wire formation needs to be explained. In this effect, wire formation appears to stop when the remaining film thickness achieves a stable value shown in Fig. 2.7(b) and Fig. 2.10(b). In order to understand these aspects, we have resorted to finite element calculations of the nanosecond pulsed laser interference heating of the SnO_2 films to determine the temperature behavior as a function of film thickness and laser energy density.

2.4.4 Collaborative work on SnO_2 NSA based hydrogen sensor

In the previous sections, synthesis and applications of 1-D SnO_2 periodic nanostructured arrays (NSA) using a pulsed laser interference technique for H_2 gas sensing was explained. Our collaborators at the University of central Florida have shown that the 1D SnO_2 shows excellent sensitivity to hydrogen sensing at room temperature, with the ability to detect less than 300 ppm of hydrogen. This result is significantly better than any current hydrogen sensor. *Our collaborators at UCF are presently working on developing a*

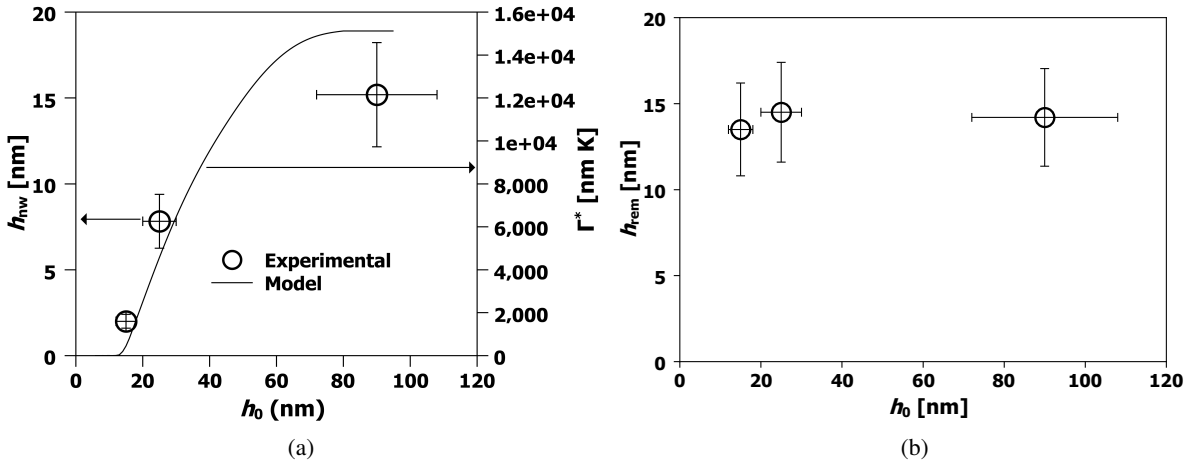


Figure 2.7: Behavior of the nanowire characteristics prepared at the same laser energy density as a function of starting film thickness. (a) Experimentally determined nanowire height h_{nw} (open circles, left axes) and theoretically estimated integrated evaporation Γ^* (line, right axes). The nanowire height h_{nw} increases with increasing starting film thickness h_0 . (b) Observation of the self-limiting effect. The experimentally measured remaining film thickness h_{rem} (symbols) is almost similar for all the films. The laser energy density used was 300 mJ cm^{-2} , the interference angle was 72° and the number of pulses was 3000 for all samples.

model to explain the enhanced hydrogen sensing capability of our materials, as described below [14]. We first summarize their results here.

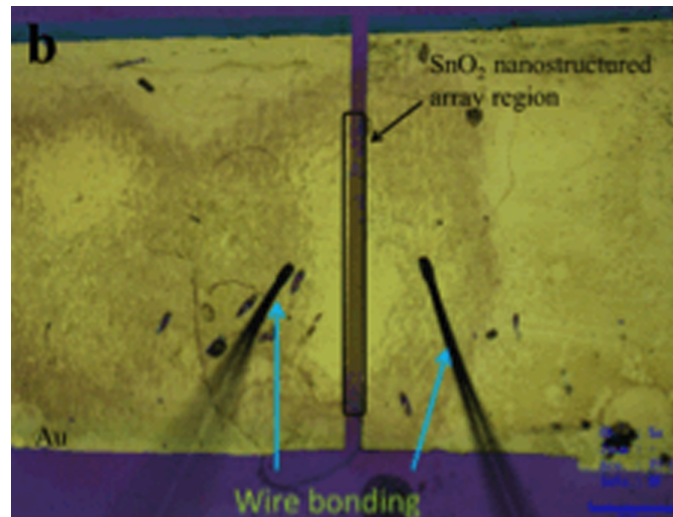


Figure 2.11: Image obtained through confocal microscope of SnO₂ nanostructured array supported on SiO₂/Si substrate with Au pads and wire bonding. It shows the sensing material region exposed to the environment [14].

2.4.4.1 Experimental details of sensor array fabrication

At room temperature, 24 nm thick SnO₂ films were deposited by pulsed laser deposition (PLD) technique under ultra high vacuum conditions (5×10^{-8} Torr) on commercially available and optically smooth

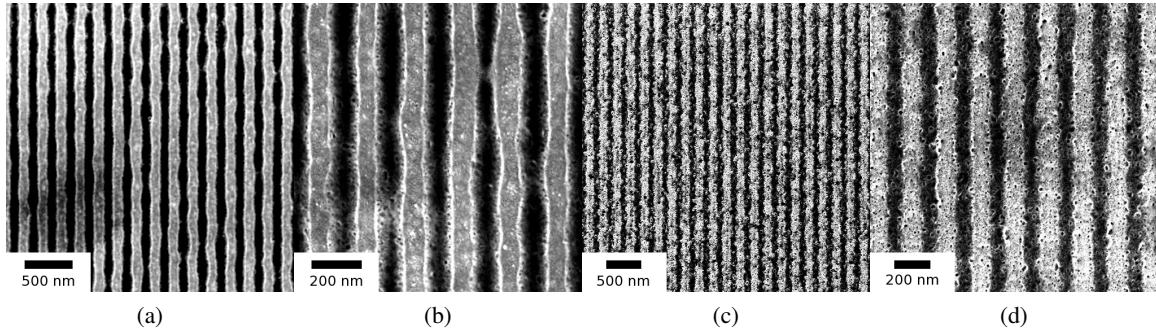


Figure 2.8: SEM images of nanowires from 42 nm film for two different E_0 with the interference angle, $\theta_i = 86^\circ$, and 3000 laser pulses. (a) $E_0 = 440 \text{ mJ cm}^{-2}$ and (b) magnified image of (a). (c) $E_0 = 535 \text{ mJ cm}^{-2}$ and (d) magnified image of (c).

400 nm thick SiO_2 on Si wafers. Thickness of the films was measured by performing step height measurements with AFM (Multiview-1000, Nanonics). Following the deposition, Nd:YAG laser at its 4th harmonic with a 9 ns pulse width and a 50 Hz repetition rate (Lab130-50, Spectra Physics) was used for laser processing. Under ambient conditions, the films were irradiated by two equally split laser beams at an interference angle of 72 degrees. The laser energy density before the split was 310 mJ/cm^2 and 3000 laser pulses were applied. Further details of the synthesis processes and characterizations can be found in an earlier work [123]. To perform sensor measurement evaluation, the electrical contacts were made on SnO_2 planar film and SnO_2 nanostructured arrays (NSA) in combination with UV-lithography and e-beam deposition. First, the contact locations were defined by the lithography, and then Cr/Au (5 nm/45 nm) layers were deposited using e-beam evaporation technique. Wire contacts were prepared on Au pads by wire bonding. The device fabrication and testing was performed by our collaborators at the University of Central Florida (UCF). The figure of the final sensor device is shown in Fig. 2.11.

2.4.4.2 Testing of Sensor Devices by UCF collaborators

The SnO_2 sensors were tested under dynamic condition by which the sensors were exposed to a calculated concentration of hydrogen gas, flowing in a closed and controlled environment (KSC NASA Test Chamber). The sensor test set-up has already been described elsewhere in detail [124]. During the testing, the four-probe technique was used to measure the resistance in air as well as in the hydrogen containing environment. The sensor test was conducted at room temperature (25 deg). Tests of the nanoarrays were accomplished in a similar manner using dynamic conditions to simulate the actual environmental conditions under which the sensors were expected to perform. At the beginning of the test, Ultra High Purity (UHP) oxygen gas was blown into the chamber at 50 Torr and 25 degree Celsius for 24 hours to remove any pre-adsorbed hydrogen and surface impurities. Next, the test was conducted by exposing the sensors to UHP Air for 15 minutes, then to UHP hydrogen gas for the same time interval with UHP nitrogen as the carrier gas. At first, cyclic tests were conducted at constant concentration (3000 ppm to zero volume percent and then repeated) of hydrogen within the mixture of UHP nitrogen. Next, the concentration of hydrogen was gradually decreased (6000 ppm, 3000 ppm, 1500 ppm, etc.) to observe the sensors response to varying

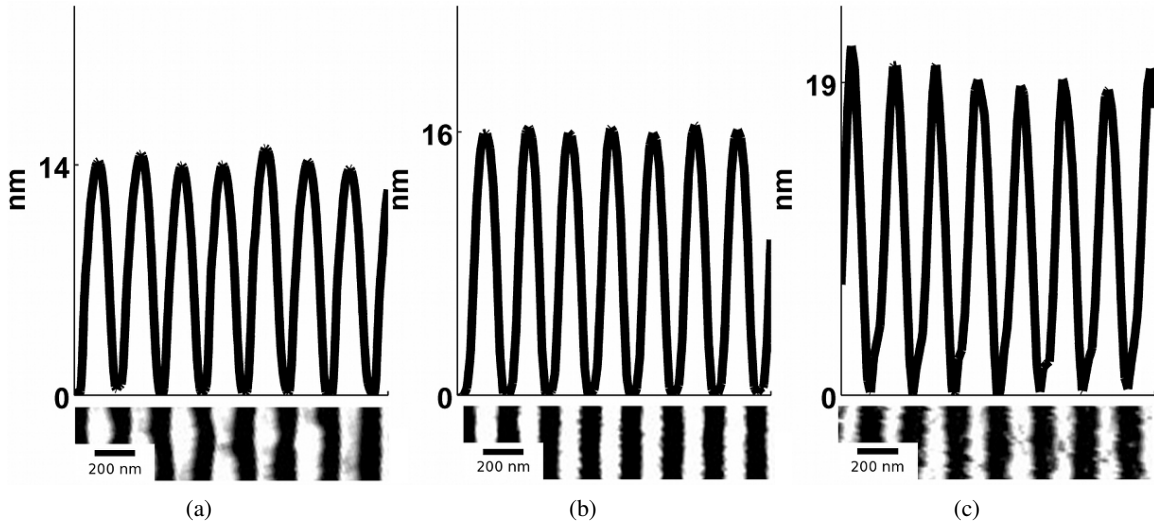


Figure 2.9: AFM line scans of the wire profiles of SnO_2 nanowires formed from three different energy densities (a) $E_0 = 440$, (b) $E_0 = 535$ and (c) $E_0 = 700 \text{ mJ cm}^{-2}$. The initial film thickness was 42 nm, the interference angle was 86° , and the number of laser pulses was 3000. The average for all measured nanowire height for each sample is (a) $h_{\text{nw}} = 14$, (b) $h_{\text{nw}} = 16$ and $h_{\text{nw}} = 19$ nm respectively.

concentrations of hydrogen and to detect the limits of each sensor's capability.

2.4.4.3 Testing Results and Discussion

The change in conductance of SnO_2 NSA and SnO_2 planar thin film sensors as a function of concentration of hydrogen at room temperature is presented in Fig. 2.12(a). The H_2 gas was varied in a wide range of concentration, ranging from 300 ppm to 6000 ppm. For SnO_2 NSA sensor, change in resistance varies significantly from 6000 ppm to 300 ppm, which demonstrates the sensor capability to detect H_2 gas at very low concentrations. On the other hand, the resistance of the film sensor does not change significantly on exposure to H_2 gas and the change in the resistance is minimal with decreasing H_2 gas concentration between 9000 to 300 ppm. Similarly, the variation the H_2 gas sensitivity of SnO_2 NSA and film sensors with respect to the hydrogen concentration is shown in Fig. 2.12(b). From the plot, the exhibited electrical response of the SnO_2 NSA to the varying H_2 concentrations shows that minimum sensitivity is around 137%. This is evidence that SnO_2 NSA are capable of detecting low H_2 concentrations even at room temperature. Typical a sensitivity of 100% for the desired hydrogen concentration is taken as a useful benchmark for a practical device. However, the electrical response of the SnO_2 film is relatively poor. Compared with the previous studies of Shukla et al., sensitivity and detection limit of hydrogen gas of SnO_2 NSA has been dramatically improved at room temperature [124]. In Fig. 2.13, the resistance variation of SnO_2 NSA and SnO_2 thin film sensors at room temperature on exposure to H_2 gas at a constant concentration at 3000 ppm are shown.

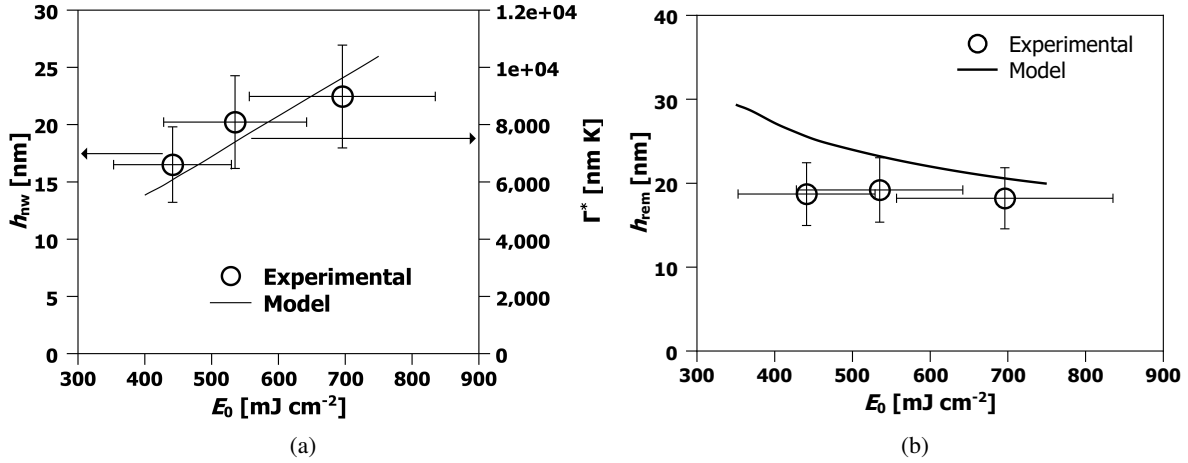


Figure 2.10: Behavior of h_{nw} and h_{rem} as a function of E_0 for 42nm films at an interference angle of 86° irradiated by 3000 pulses: (a) the experimentally determined nanowire height (open circles, left axes) and theoretically predicted behavior of the integrated evaporation difference Γ^* between regions of maxim and minima (dashed line, right axes). (b) The experimentally measured (open symbols) and theoretically predicted (line) remaining film thicknesses h_{rem} .

Cyclic exposure to fixed concentration of H_2 shows that the sensor is very robust and stable.

2.5 Discussion

In order to better understand the mechanism responsible for the formation of nanowires, an optical + thermal model was constructed to determine the temperature evolution of a multilayer system comprised of an SnO_2 thin film on a SiO_2/Si substrate irradiated by uniform as well as interfering laser beams. The first step in creating this model, shown schematically in Fig. 2.14(a), is to accurately determine the optical properties of all the materials involved, in this case the SnO_2 films, and the SiO_2 and Si substrate components. The values of the complex refractive index, N , at $\lambda = 266$ nm is reported as $N_{SiO_2} = 1.4585$ and $N_{Si} = 1.831 - 4.426i$ for the substrate materials [122, 125]. The optical properties of SnO_2 at $\lambda = 266$ nm measured by Jimenez et al. is $N = 2.04 - 0.2i$, and implies that SnO_2 films should be nearly transparent for the thicknesses and wavelengths used in this work, making pattern formation by laser-thermal heating very difficult. However, it was mentioned by the same authors in ref. [126] that the index may vary significantly depending on the method of film deposition [126]. To address this, experimental values of reflectivity, R , and transmissivity, T , for SnO_2 films of various thickness (15, 25, and 90 nm) prepared on $750 \mu m$ SiO_2 substrates was measured. The experimental R and T were compared to theoretical values calculated under the assumption of coherent layers [127]. Using a simple least squares optimization of the data, we determined that the best fit of $N = 2.0 - 0.97i$ yielded a reasonably good agreement between the measured and theoretical values of R and T , as shown in 2.14(b) and (c) respectively.

The next step to an accurate model was to find the time and position dependent energy absorption within the multilayer $SnO_2/SiO_2/Si$ system when irradiated by a pulsed laser in interference. The method outlined by Prentice [127] was modified by including the angle dependent reflectivity at the interfaces [128]. Following the same method, and accounting for the two beam interference pattern while applying a position

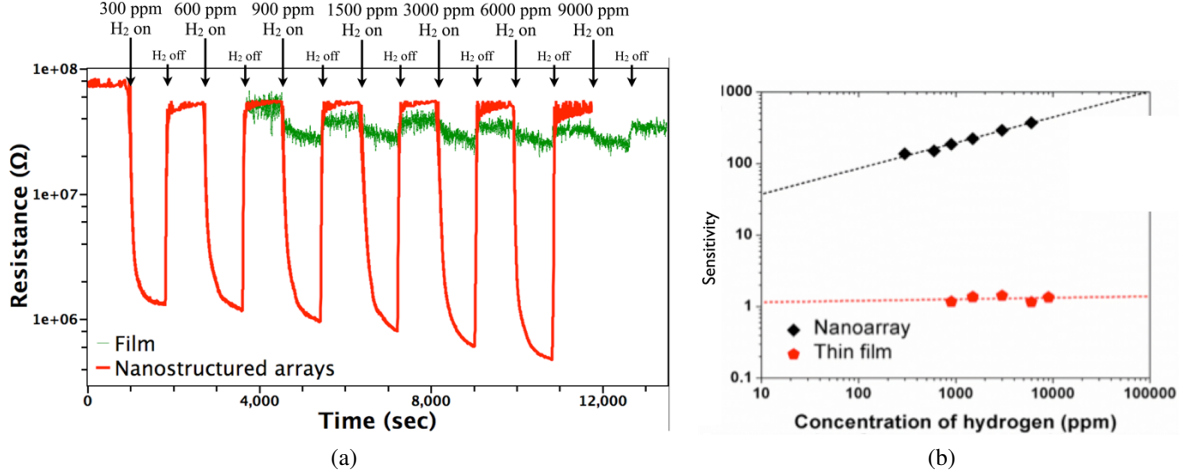


Figure 2.12: (a) The resistance variation of SnO_2 nanostructured array (red line) and SnO_2 thin film (green line) at room temperature on exposure to hydrogen gas in a wide range of concentration, ranging from 300 ppm to 6000 ppm. Change in resistance does not decrease significantly from 6000 ppm to 300 ppm, which demonstrates the sensor capability to detect H_2 gas at very low concentrations. The resistance of the film sensor does not change significantly on exposure to H_2 gas and the change in the resistance do not significantly increase with increasing H_2 gas concentration even upto 9000 ppm. (b) The exhibited electrical response of the SnO_2 NSA to the varying H_2 concentrations shows that minimum sensitivity is around 137. This is evidences that SnO_2 are more than capable of detecting lower concentration. The electrical response of the SnO_2 film is relatively insensitive [14].

dependent phase change to each beam and adding the normalized resultant electric field, E , the resultant absorption profile for a $\text{SnO}_2/400\text{nm SiO}_2/\text{Si}$ film stack can be determined [128]. The resulting normalized absorption profile is given as $\alpha^* = \alpha \frac{|E(x,z)|^2}{|E_i|^2}$, where α is the absorption coefficient of the film, $|E_i|$ is the modulus of the average incident electric field, and $|E(x,z)|$ is the modulus of the resultant electric field within the film which varies as a function of the lateral dimension, x , due to the interference pattern and the depth, z , due to absorption and reflection effects. The normalized absorption as a function of depth (z) is shown in Fig. 2.15(a), for x position corresponding to the maximum incident intensity due to complete constructive interference. The two-beam interference pattern assuming 36° off normal incidence (72° between the beams) is shown as the normalized surface absorption profile in Fig. 2.15(b), but this characteristic shape may be found for any depth. Assuming a Gaussian pulse shape, the total volumetric rate of energy absorption is given by:

$$\dot{q} = \alpha^* \frac{E_p}{\sigma \sqrt{2\pi}} e^{-\frac{(t-t_p)^2}{2\sigma^2}},$$

where E_p is the total energy per pulse per unit area, t_p is the pulse width, and the standard deviation of the pulse $\sigma = \frac{t_p}{2\sqrt{2\ln(2)}}$ [105].

This model was then applied to a 2-D thermal finite element analysis (COMSOL) including characterization of the melting of the SnO_2 film as was conducted by Trice et al. to determine the temperature evolution at every point in the film stack [105]. The thermal conductivity of SiO_2 was taken as the non-radiative

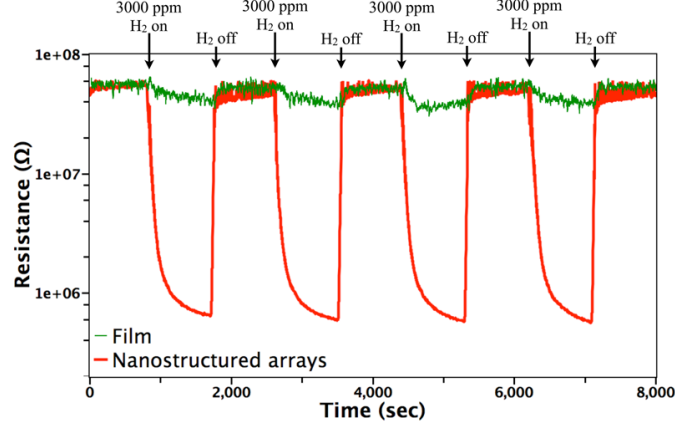


Figure 2.13: The resistance variation of SnO_2 nanostructured array (red line) and SnO_2 thin film (green line) at room temperature on exposure to hydrogen gas at a constant concentration at 3000 ppm. Cyclic exposure to fixed concentration of H_2 shows that the sensor is very robust and stable [14].

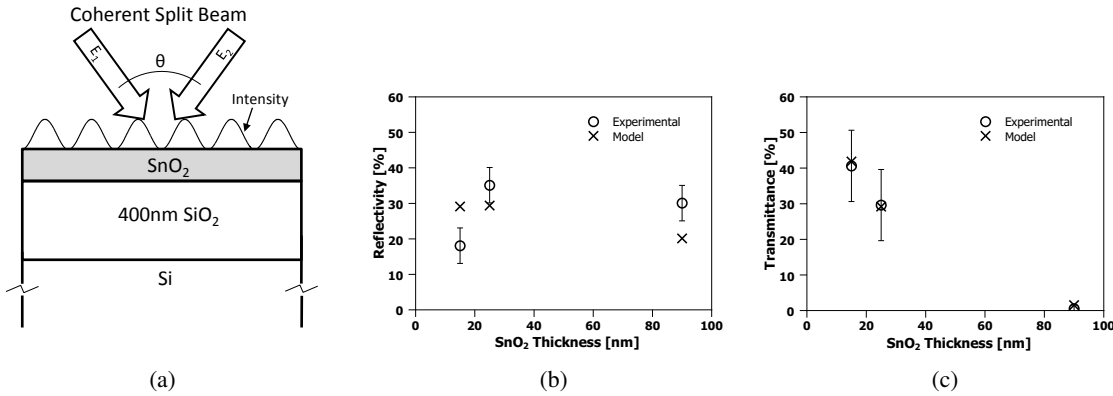


Figure 2.14: (a) Schematic of geometry used for the optical + thermal model. (b) The measured reflectivity, and (c), transmittance (open symbols) of known thicknesses of SnO_2 deposited on $750 \mu\text{m}$ quartz from optical spectroscopy. The best fits (crosses) were modeled assuming $N_{\text{SnO}_2} = 2.0 - 0.97i$.

thermal conductivity since the length scales involved are significantly shorter than wavelengths involved in radiative transport [129, 130]. The temperature dependent heat capacity of SnO_2 was determined from Pankratz [131] and density from Taylor [132]. Due to the lack of data, only the room temperature thermal conductivity of SnO_2 , $k = 10 \text{ Wm}^{-1} \text{K}^{-1}$, was available, so this value was taken as temperature independent [133]. The remaining thermal properties of SiO_2 , and those of Si were taken as the temperature dependent functions given in a material constants handbook [134]. The melting temperature of SnO_2 (1903.2°K) and the enthalpy of fusion (155.3 J g^{-1}) were employed to model the phase change by an effective heat capacity technique [134, 105]. A complete list of the optical and thermal properties used for this simulation are given in Table 2.1 and Table 2.2, respectively. Verification of the 2-D thermal model was performed by comparing the experimentally determined melt threshold for single beam irradiation at normal incidence of two samples of known thickness, which yielded 63 and 99 mJ cm^{-2} for 5 nm and 42 nm films respectively. These values

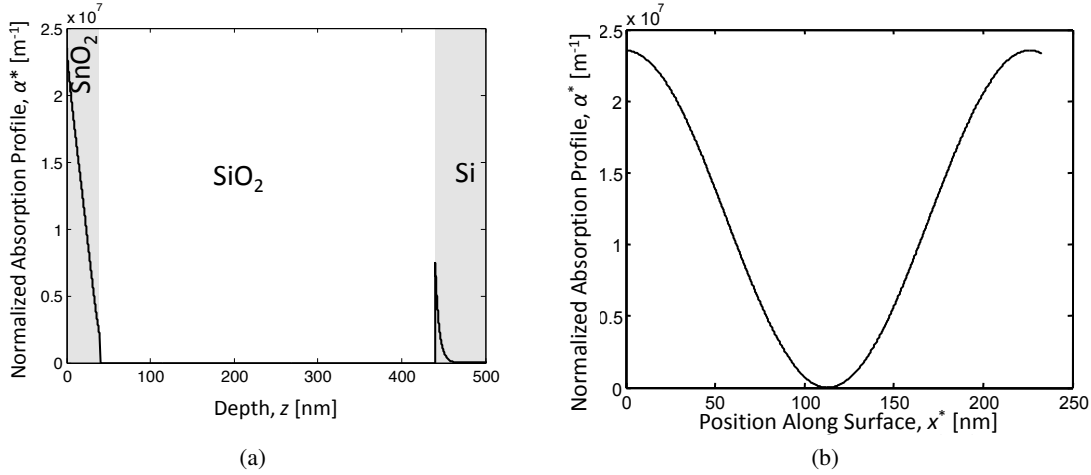


Figure 2.15: Absorption profiles of the SnO₂/SiO₂/Si stack for the case of: (a) complete constructive interference depth profile and (b) surface absorption profile.

compared favorably with the model, which predicted values of 60 and 91 mJ cm⁻².

Table 2.1: Optical values used in the simulation.

Quantity	Description	Value [Reference]
N_{SnO_2}	Index of refraction	2.0 - 0.97i (Fit,[126])
N_{SiO_2}	Index of refraction	1.45846 [122]
N_{Si}	Index of refraction	1.831 - 4.426i [125]
$\sigma = t_p/2\sqrt{2\ln(2)}$	Standard deviation	3.822 ns [105]

Applying this model to the experimental conditions outlined previously, the temperature difference between interference maxima and minima of the liquid SnO₂, ΔT , determined at the moment the entire film has melted is given in Fig. 2.16(a). The film temperature at the maxima and minima of the interference pattern for the case of average incident energy per pulse of 400 mJ cm⁻², is shown in Fig. 2.16(b) as a function of film thickness. Clearly, the thickness of the SnO₂ film has a profound effect on these temperatures. A non-monotonic variation in the temperature is seen, with a maxima occurring around a film thickness of 25 nm, and dropping sharply for thinner films. This type of temperature variation has been observed previously for ultrathin metal films on optically transparent substrates [105]. The behavior arises from the nanoscale nature of laser-film heating and can be briefly explained here as follows [12, 44]. For the case of SnO₂, the experimentally estimated skin depth δ at 266 nm wavelength is 21.8 nm (as obtained from the experimentally extracted k values). Consequently, for SnO₂ films with thickness comparable to the skin depth, the intensity of light energy absorbed will vary exponentially with thickness as $I(h_o) = I_o(1 - e^{-h_o/\delta})$, where I_o is the incident light intensity. Secondly, the effective reflectivity of light from the surface of the SnO₂ film on the SiO₂ substrate is also strongly dependent on SnO₂ film thickness. This can be understood physically by noting that at zero film thickness the reflectivity will be that of the SiO₂ substrate (which is practically zero for UV light) while it will be the value of the bulk SnO₂ (which is \gg zero) for a very thick film.

From the experimental measurements of reflectivity and estimated N values, a quantitative calculation based on evaluating the Fresnel coefficients for such $\text{SnO}_2/\text{SiO}_2$ bilayer systems yields the general nature of the thickness dependent reflectivity as $R(h_o) = r_o(1 - \exp(-a_r h_o))$, where a_r and r_o are materials-dependent parameters [128]. Third, the effective mass of the material heated $M(h_o)$ is also a strong function of film thickness for the following reason. When the film thickness is less than one thermal conduction depth, any heat generated within the nanoscopic metal film due to optical absorption will diffuse into the underlying SiO_2 substrate. Consequently, the effective mass of material heated will include the thermal mass of the film and an effective thermal mass of the substrate estimated from the length scale of thermal diffusion occurring within the substrate in the nanosecond time scales of the experiment. Therefore, the heated mass will be $M(h_o) = (\rho C_p)_m h_o + (\rho C_p)_s \sqrt{D_s^t h}$, where the subscript m and s denote metal and substrate while ρ and C_p are values of density and specific heat, D_s^t is the substrate thermal diffusivity and τ is the ns time scale of laser heating. Consequently, energy balance shows that the temperature rise will be qualitatively given by $\Delta T(h_o) = I(h_o)(1 - R(h_o))\tau/M(h_o)$. As can be noted, in this function, I increases with increasing thickness while $(1-R)$ and $1/M$ decrease with increasing thickness. As a result, a non-monotonic variation in temperature with film height h_o can be expected for any given laser intensity and in fact at a critical film thickness the temperature rise will be a maximum. This behavior, as estimated from a more accurate finite element modeling, is shown in Fig. 2.16(b). A maxima in temperature occurs around a film thickness of 25 nm, while there is a large rate of change in temperature with thickness for films on either side of this maxima.

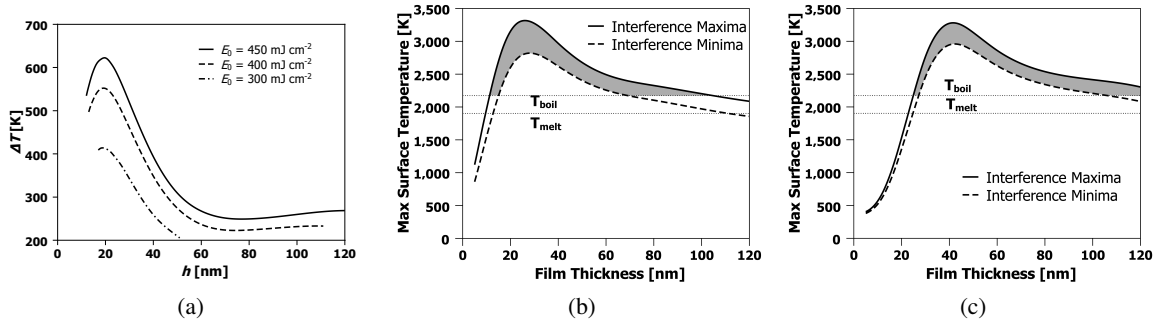


Figure 2.16: *Thermal model results showing: (a) the temperature difference between the the interference maxima and minima when the entire film has melted; (b) maximum surface temperature as a function of SnO_2 film thickness for $\theta = 72^\circ$ and $E_o = 400 \text{ mJ/cm}^2$; and (c) maximum surface temperature as a function of SnO_2 film thickness for $\theta = 86^\circ$ and $E_o = 550 \text{ mJ/cm}^2$. The shaded regions in (b) and (c) represent the integrated evaporation difference Γ^* .*

2.6 Conclusion

The nanowire array may be formed by either liquid movement due to thermocapillary (TC) forces resulting from a temperature induced surface tension gradient, or preferential evaporation of the film between the regions of high intensity (constructive interference) and low intensity. As shown in Fig. 2.16(a), the two

beam irradiation causes a temperature disparity between the regions of constructive and destructive interference. Consequently, the surface tension gradient generates marangoni or thermocapillary flow along the plane. An estimate of magnitude of contribution of TC effects on fluid flow may be directly obtained from the characteristic time scale of TC flow τ_M . As shown in ref. [135], τ_M depends on the temperature gradient on the film surface, the film thickness h_o , as well as materials parameters, and can be expressed as:

$$\tau_M = \frac{\Lambda_{laser}^2 \eta}{4 \frac{\partial \gamma}{\partial T} \Delta T h_o} \quad (2.1)$$

where Λ_{laser} , η , $\frac{\partial \gamma}{\partial T}$ and ΔT are the laser fringe spacing, dynamic viscosity of the film material, rate of surface tension change with temperature and peak-valley temperature difference, respectively. Due to the unavailability of actual dynamic viscosity and the surface tension data for SnO₂ the material constants of a known ceramic oxide, close to the position of tin oxide in the periodic table (such as lead oxide), was adapted judiciously. For lead oxide, $\eta = 2.1$ Pa·s and is $\frac{\partial \gamma}{\partial T} = -0.0968 \text{ Jm}^{-2} \text{ K}^{-1}$ and this was used to estimate the TC time scale [136]. For the case of $E_o = 400 \text{ mJ cm}^{-2}$ and $h_o = 50 \text{ nm}$, a temperate difference of $\Delta T = 530 \text{ K}$ was obtained from thermal modeling for a fringe spacing of $\Lambda_{laser} = 225 \text{ nm}$ (corresponding to $\theta_i = 72^\circ$). From this, the value of τ_M was estimated to be around 9 ns, which is comparable to the laser pulse time scale suggesting that it is reasonable to expect some contribution from TC flow under the two beam interference irradiation. However, at this stage, the experimental observations from wire formation cannot clearly differentiate between contributions from TC flow versus evaporation. Moreover, since we have observed substantial evaporation, it is also important to estimate the magnitude of contribution from preferential evaporation on the wire formation.

First, the maximum rate of evaporation at a given temperature can be estimated from the classical relation between pressure and temperature [137] as:

$$\Gamma_e = 5.834 * 10^{-2} P_e \sqrt{\frac{M}{T}} \quad (2.2)$$

where Γ_e = the mass evaporation rate in $\frac{\text{g}}{\text{cm}^2 \text{ s}}$, M is the molecular weight, and P_e is the equilibrium pressure in Torr . Assuming a 9 ns melt time, the theoretical evaporation rate for SnO₂ at its boiling temperature of 2173 K is $0.15 \text{ nm pulse}^{-1}$. Assuming a constant evaporation rate, fewer then 1000 pulses would be required to remove 100 nm of film. However, as seen from Fig. 2.16(b) the peak film temperature is non-monotonic with respect to h_o leading to a cut-off of evaporation at a critical thickness, which corresponds approximately to the film thickness where the maximum film temperature is equal to the melting point of the SnO₂. For the case of $\theta_i = 72^\circ$ and $E_o = 400 \text{ mJ cm}^{-2}$, Fig. 2.16(b), this occurs at $h = 11 \text{ nm}$. From the above discussion, the observation of a final fixed remaining thickness h_{rem} following processing of films of varying initial thickness at a given energy density E_o can also be explained qualitatively. The model predicts that for $E_o = 300 \text{ mJ cm}^{-2}$ and $\theta_i = 72^\circ$, $h_{rem} = 13 \text{ nm}$, which is in good agreement with our experimental observation shown in Fig. 2.7(b). Additionally, for the case of $\theta_i = 86^\circ$ and $h_o = 42 \text{ nm}$, h_{rem} was found to be only weakly dependent on E_o (Fig. 2.10(b), open circles), which agrees with the theoretical prediction (solid line), and the true nature of the dependence (predicted to be decreasing h_{rem} with increasing E_o)

may be masked by the inherent error in the experiment. From this analysis, one can claim that evaporation sharply drops following thinning of the film beyond the position of the temperature maxima. Interestingly, the temperature gradient also drops sharply in this region, as evident from Fig. 2.16(b). Therefore, we suggest that the self-limiting behavior occurs due to this shutting-off of evaporation and the parallel reduction in thermal gradients, which reduces TC flow.

Table 2.2: Thermal values used in the simulation. L is heat of transformation; ρ is density; k is thermal conductivity; C is heat capacity; T is temperature, and ϵ is phase change tuning parameter.

Quantity	Value [Reference]
L	155.3 J g ⁻¹ [134]
ρ_{SnO_2}	$\rho = \begin{cases} -0.1062T + 6930.86 \text{ kg m}^{-3}, & \text{if } T \leq 1773 \text{ K} \\ 6742.57 \text{ kg m}^{-3}, & \text{if } T > 1773 \text{ K} \end{cases}$ [132]
ρ_{SiO_2}	$\rho = \begin{cases} 1.43E^{-14} - T^5 5.00E^{-11} T^4 + 6.98E^{-8} T^3 - 4.71E^{-5} T^2 + 1.11E^{-2} T \\ + 2219.39 \text{ kg m}^{-3}, & \text{if } T \leq 1000 \text{ K} \\ 2217.53 \text{ kg m}^{-3}, & \text{if } T > 1000 \text{ K} \end{cases}$
ρ_{Si}	$\rho = \begin{cases} -1.37T^4 + 4.29E^{-8} T^3 - 5.43E^{-5} T^2 + 3.84E^{-3} T \\ + 2332.57 \text{ kg m}^{-3}, & \text{if } T \leq 1000 \text{ K} \\ 2311.28 \text{ kg m}^{-3}, & \text{if } T > 1773 \text{ K} \end{cases}$
k_{SnO_2}	10 W m ⁻¹ K ⁻¹ [134]
k_{SiO_2}	Extrapolated from: [129]
k_{Si}	$k = \begin{cases} -1.53E^{-17} T^4 + 4.76E^{-14} T^3 - 5.54E^{-11} T^2 + 3.02E^{-8} T \\ - 2.62E^{-6} \text{ W m}^{-1} \text{ K}^{-1}, & \text{if } T \leq 1000 \text{ K} \\ 4.40E^{-6} \text{ W m}^{-1} \text{ K}^{-1}, & \text{if } T > 1000 \text{ K} \end{cases}$ [138, 139]
C_{pSnO_2}	$C_p = \begin{cases} 1.62E^{-10} T^4 - 2.72E^{-7} T^3 - 2.96E^{-4} T^2 + 0.826T \\ + 134.45 \text{ J kg}^{-1} \text{ K}^{-1}, & \text{if } T \leq 1100 \text{ K} \\ 1.01E^{-8} T^3 - 6.21E^{-5} T^2 + 0.149T \\ + 457.63 \text{ J kg}^{-1} \text{ K}^{-1}, & \text{if } 1100 \text{ K} < T \leq 1800 \text{ K} \\ 583.97 \text{ J kg}^{-1} \text{ K}^{-1}, & \text{if } T > 1800 \text{ K} \end{cases}$ [131]
C_{pSiO_2}	$C_p = \begin{cases} -7.06E^{-12} T^5 + 1.88E^{-8} T^4 - 1.70E^{-5} T^3 - 4.46E^{-3} T^2 \\ + 1.93T + 61.49 \text{ J kg}^{-1} \text{ K}^{-1}, & \text{if } T \leq 925 \text{ K} \\ 3.13E^{-8} T^3 - 1.11E^{-4} T^2 + 0.371T + 890.24 \text{ J kg}^{-1} \text{ K}^{-1}, & \text{if } 925 \text{ K} < T \leq 2000 \text{ K} \\ 1188.24 \text{ J kg}^{-1} \text{ K}^{-1}, & \text{if } T > 2000 \text{ K} \end{cases}$ [140, 141]
C_{pSi}	$C_p = \begin{cases} -1.91E^{-9} T^4 + 5.95E^{-6} T^3 - 6.95E^{-3} T^2 + 3.77T \\ + 63.04 \text{ J kg}^{-1} \text{ K}^{-1}, & \text{if } T \leq 900 \text{ K} \\ -3.18E^{-5} T^2 + 0.187T + 769.46 \text{ J kg}^{-1} \text{ K}^{-1}, & \text{if } 900 \text{ K} < T \leq 1685 \text{ K} \\ 994.45 \text{ J kg}^{-1} \text{ K}^{-1}, & \text{if } T > 1685 \text{ K} \end{cases}$ [140, 141]
$T_{melt} (SnO_2)$	1903 K
$T_{boil} (SnO_2)$	2173 K
ϵ	10 K [105]

The thermal model can also be used to explain the behavior of h_{nw} as a function of h_o and E_o . In Fig.2.16(b) and (c), the temperature difference between the regions of maxima and minima are shown as a function of starting film thickness h_o for the 72 and 86° irradiation geometries respectively. As 2.16(b)

and (c) show, evaporation will occur at the maxima and minima locations, but at different rates because of the different temperatures. For thick films (> 25 nm or so), this evaporation rate increases as the film thins. Now, as the temperature in the maxima continues to rise, the temperature in the minima will also begin to rise as a consequence of thermal diffusion. Consequently, the minimum also enters the evaporation zone and starts thinning. Now, a parallel thinning of the maxima and minima occur, albeit at slight different rates, as given by their respective temperatures. Finally, both locations thin enough such that the evaporation stops. From Fig. 2.16(b) or (c), the two regimes can be seen to have slightly different evaporation cut-off thicknesses. If one assumes a constant evaporation rate for the entire film, so that the total evaporation time $t_{evap} \propto h_0 - h_{eff}$, and if the local evaporation rate is assumed to be relative to the modeled $T - T_{boil}$, a relative measure of preferential evaporation may be determined by integrating the relative temperature difference that exists above the melting point and the thickness. This relative evaporation difference Γ^* can be evaluated as:

$$\Gamma^* = \int_0^{h_0} T_{maxima}^*(h) - T_{minima}^*(h) \quad (2.3)$$

where

$$T^* = \begin{cases} T^* - T_{boil} & \text{if } T^* \geq T_{boil} \\ 0, & \text{if } T^* < T_{boil}, \end{cases} \quad (2.4)$$

where T_{maxima}^* and T_{minima}^* are, for a given h , the difference between the peak temperatures of the interference maxima and minima and the boiling point, and where temperatures below the boiling point result in a value of zero. If the previous assumptions are valid, the resulting integrated evaporation, Γ^* , should be proportional to h_{nw} . As shown by the open circles in 2.7(a), films of larger initial thickness exhibit a much greater h_{nw} , and are in qualitative agreement with the theoretical Γ^* , plotted as the solid line. It should be noted that the scale of Γ^* is arbitrary, but agrees with the experimentally measured data when both y axes intersect the x axis at 0. Similarly, increasing E_0 should increase Γ^* , since ΔT increases in concert with E_0 . This relationship agrees with the experimentally determined data in 2.10(a). However, due to the angle disparity between the constant energy and thickness experiments, the absolute values of Γ^* could not be compared between the two cases.

From this discussion, the non-monotonic thickness-dependent temperature behavior provides opportunity to synthesize wires under a variety of interesting laser parameters. For instance, by varying the intensity of the individual interfering beams, it is possible to modulate the temperature difference between the maxima and minima. Hence, this can be used to influence h_{nw} as well as the h_{rem} . Another important aspect of the processing of SnO_2 is the relatively small difference between the melting point and boiling point (i.e. 270 K). As a result, wire formation by pure thermocapillary flow requires stringent control on the laser energy as well as in the intensity of each of the interfering beams. These studies could form the basis for further investigations of wire formation in SnO_2 .

In conclusion, we have synthesized parallel nanowire arrays of SnO_2 on SiO_2 substrates by nanosecond pulsed laser irradiation. Such nanowires are potential candidates for improved H_2 sensor performance. The

array morphology was characterized by SEM and AFM, in conjunction with EDS and XPS measurements to evaluate concentration and stoichiometry. Due to evaporation, the final nanowire array had a lower effective SnO₂ film thickness, whose value was independent of starting film thickness for any given laser energy density, but decreased with increasing energy density. Furthermore, a self-limiting effect was observed wherein the wire formation stopped at this effective remaining film thickness. These behaviors could be explained by nanoscale effects of the laser-film heating that resulted in a highly non-monotonic film temperature dependence on film thickness. In addition to the nanowire height, the structure of the nanowires was dependent on the amount of evaporation, with large initial thicknesses producing consistent nanowires and small thicknesses, where no evaporation takes place, producing clusters of nanoparticles. These results show that fabrication of large nanowire arrays can be achieved by careful analysis of the thermal behavior in conjunction with experiments. Also, the SnO₂ nanostructured arrays based hydrogen sensor was tested under dynamic conditions of hydrogen environment. The electrical response of SnO₂ towards hydrogen at low concentration at room temperature operation was improved in the nanostructured arrays as compared to the film. The results suggest that SnO₂ nanostructured arrays has the potential to produce highly functional hydrogen sensor at room temperature for practical applications.

Chapter 3

Thermodynamic modeling of thin metallic liquid films dewetting

(Reported to J. Appl. Phys. 108, (2010))

Thermodynamic model for the dewetting instability in ultrathin films

3.1 Summary

The spontaneous pattern formation via the classical spinodal dewetting instability in ultrathin films is a nonlinear process. However, the physical manifestation of the instability in terms of characteristic length and time scales can be described by a linearized form of the initial conditions of the film's dynamics. Alternately, the thermodynamic (TH) approach based on equating the rate of free energy decrease to the rate of frictional loss via viscous dissipation [de Gennes, C. R. Acad. Paris **298**, 111 (1984)] can give similar information. Here we have evaluated dewetting in the presence of film-thickness- (h) dependent thermocapillary forces. Such a situation can be found during pulsed laser melting of ultrathin metal films where nanoscale effects lead to a local h -dependent temperature. The TH approach provides an analytical description of this thermocapillary dewetting. The results of this approach agree with those from linear theory and experimental observations provided the minimum dissipation is equated to the rate of free energy decrease. The flow boundary condition that produces this minimum dissipation is when the film-substrate tangential stress is zero. The physical implication of this finding is that the spontaneous dewetting instability follows the path of minimum rate of energy loss.

3.2 Introduction

Investigations of thin film morphology evolution and control is of fundamental and technological interest. In particular, spontaneous self-organizing processes [142] that lead to nanostructure formation in a reliable

way have attracted tremendous attention. The resulting nanostructures can have novel behavior as well as be utilized in a wide variety of technologies, such as, energy harvesting [143, 144, 145], biomedicine [146, 147], spintronics [148], photonics [34] and magnetism [149, 5]. One example of a self-organizing process is the spontaneous dewetting of a continuous liquid film from a surface. A scientific understanding of dewetting has implications to many industrial applications, including in the deicing of airplane wings with non-wettable surfaces, in preventing hydroplaning of automobiles on wet roads due to thin continuous layer of water and in designing chemicals to prevent the break-up of the lachrymal film that protects the cornea of the eye. Another growing application of dewetting is in the fabrication of nanoscale structures in a robust, controllable and cost-effective manner. The extensive studies of polymer thin films and growing number of investigations of dewetting in metallic thin films is indicative of this technological interest and also to the need for a deeper understanding of the phenomenon [150, 151, 41, 152, 153, 104, 154, 10, 43, 105].

The classical dewetting instability in thin films can be interpreted as a competition between two energy terms. For the case of a large number of polymer or metallic films studied, these two energies correspond to the surface tension and the attractive intermolecular dispersion force between the film-substrate and film-vacuum interfaces mediated by the film material. As shown first by Vrij [96, 97], the instability can be described from an energetic viewpoint by evaluating the thermodynamic free energy change of the system under perturbations to the film height. The prediction from such an energy analysis is that for certain perturbation wave vectors, the film enters an unstable state and thus, can spontaneously dewet. As a result, studies of dewetting have focused largely on the fluid dynamics of the film, through which it is possible to obtain the relationship between the rate of growth or decay of surface perturbations to their wave vector, i.e. the dispersion relation. However, the fluid dynamics for even the simplest dewetting scenario, such as the example above, is a highly nonlinear process, and, while addressable by many numerical techniques [155, 156, 157, 99], is often evaluated through a linear analysis in order to achieve physical insights into dewetting. An alternate approach to quantitatively evaluate dewetting is thermodynamics. Fluid flow pathways can be analyzed through thermodynamic considerations in which the conversion of useful internal energy to external energy loss via heat, such as by viscous dissipation, is used to quantify the behavior [158, 159].

In this work, we show that such an approach can provide meaningful insight into the nature of fluid flow as well as the energy pathway for dewetting instabilities. Specifically, we have applied the thermodynamic formulation to the case of dewetting in which film thickness dependent Marangoni or thermocapillary forces are also present. Such a situation has been observed in the melting of thin metallic films by nanosecond pulsed lasers [12, 44]. In our thermodynamic analysis the rate of thermodynamic free energy decrease due to film thickness fluctuations is balanced with the rate of energy loss due to viscous flow, i.e. viscous dissipation. This leads to an analytical description of the dewetting process without explicit need to solve the height evolution dynamical equation from the Navier-Stokes (NS) equation. The thermodynamic and linear approach show identical results for classical dewetting. For thermocapillary dewetting, the two approaches agree only if the minimum viscous dissipation is evaluated. This minimum was found to occur for a particular flow boundary condition, which related the pressure gradient with the thermocapillary forces, and resulted in zero tangential stress at the film-substrate interface. Besides this physical insight into the fluid flow, the thermodynamic analysis also showed that the dewetting pathway is one in which the rate of

energy loss is minimized.

3.3 Theory

For completeness, we first begin by summarizing the derivation of the thin film fluid velocity for a one-dimensional (1D) incompressible fluid from the NS equation within the lubrication approximation. A complete analysis is provided in ref. [160]. In this approximation the average or unperturbed thickness h_o of the film is much smaller than the in-plane dimension (x), as a result of which, the only velocity change of importance occurs along the thickness or z -direction. Furthermore, because of the small thickness of the film, inertial effects can be neglected and so the flow is dominated by the viscous effects. Using the above approximations, the NS equation for the steady-state condition ($\rho \frac{dv}{dt} = 0$) in the x -direction is given by:

$$\nabla P = \eta \frac{d^2 v}{dz^2} \quad (3.1)$$

where v is the x -component of the liquid velocity, $\nabla P = \frac{dp}{dx}$ is the pressure gradient in the direction of flow x , and η is the dynamic viscosity. By integrating the velocity v as a function of height z we get:

$$v = \nabla P \frac{z^2}{2\eta} + az + b \quad (3.2)$$

Typical boundary conditions used to analyze the classical dewetting instability are the no-slip condition at the film-substrate, so $v(h=0) = 0$, and a stress-free boundary condition at the top film surface. The no-slip condition results in $b = 0$. At the top surface, we introduce the h -dependent Marangoni effect by equating the shear stress to the surface tension gradient: $\eta \frac{dv}{dz}|_{h_0} = \frac{d\gamma(h)}{dh} \frac{dh}{dx} = \gamma_h \frac{dh}{dx} = (\gamma_h h')|_{h_0}$, where, $\gamma(h)$ is h -dependent surface tension of the film-vapor interface, $|\gamma_h| = \left| \frac{d\gamma}{dh} \right|$ is the magnitude of the height coefficient of surface tension, and $\frac{dh}{dx} = h'$ is the thickness/height gradient along the flow direction, with all quantities evaluated at the average film thickness h_o . From this, the velocity and velocity gradient in the z -direction can be respectively expressed as:

$$v = \frac{\nabla P}{2\eta} z^2 - \frac{\nabla P h_0 - \gamma_h h'}{\eta} z \quad (3.3)$$

and

$$\frac{dv}{dz} = \frac{\nabla P}{\eta} z - \frac{\nabla P h_0 - \gamma_h h'}{\eta} \quad (3.4)$$

Based on this, one can now easily evaluate the rate of energy loss due to viscous liquid flow, i.e. the viscous dissipation, per unit volume \dot{e} occurring in the film. This quantity is given by [161]:

$$\dot{e} = \eta \left(\frac{dv}{dz} \right)^2 = \frac{(\nabla P)^2}{\eta} z^2 - \frac{2\nabla P (\nabla P h_0 - \gamma_h h')}{\eta} z + \frac{(\nabla P h_0 - \gamma_h h')^2}{\eta} \quad (3.5)$$

For the case of classical dewetting, i.e. in which Marangoni forces are absent ($\gamma_h = 0$), the viscous

dissipation will be:

$$\dot{e}_C = \frac{(\nabla P)^2}{\eta} (z - h_o)^2 \quad (3.6)$$

where the superscript denotes classical.

Next, we can evaluate the rate of thermodynamic free energy change ΔF for fluctuations/perturbations to the initial height of the film. Since we are primarily concerned with the dewetting instability, we will use the classical approach proposed by Vrij where-in the film-vapor surface tension energy competes with the attractive dispersion energy. Film height perturbations will increase the top film surface area and so surface tension increases the overall thermodynamic free energy of the film. On the other hand, the long range attractive dispersion energy varies as $A/2\pi h^4 (= \Pi'')$, where A is the Hamaker coefficient with negative sign, leading to an overall decrease in thermodynamic free energy. As Vrij showed, it is the free energy decrease resulting from competition between these two energy terms that drives the dewetting instability. Here, we evaluate the rate of this free energy change by expressing the height perturbations as Fourier components of type:

$$h(x, t) = h_0 + \varepsilon e^{\sigma t} e^{-ikx} \quad (3.7)$$

where the perturbation has an amplitude of ε , a characteristic temporal decay rate σ and a corresponding wave vector k . In this work, we explore the thermodynamic solution for a thermocapillary/Marangoni problem where the surface tension is dependent on the local height, but its derivative with respect to the film height ($\gamma_h = d\gamma/dh$) is independent of the x -position on the surface. Consequently, the surface tension change does not contribute to a change in free energy. This can be shown as follows. The standard procedure is to calculate the rate of total free energy change due to the height perturbation and evaluate it over one wavelength of the perturbation [96]. In this case, the resulting rate of energy change will be:

$$\Delta F_{single\ wavelength} = \int_0^\lambda \left(\frac{1}{2} \gamma \left| \frac{\partial h}{\partial x} \right|^2 + \frac{1}{2} \Pi'' \Delta h^2 + \frac{1}{2} \gamma_h \Delta h \right) dx \quad (3.8)$$

One can immediately see that since γ_h is independent of the x -position along the film, the integral of the third term is $\int_0^\lambda \frac{1}{2} \frac{d\gamma}{dh} \varepsilon e^{-ikx + \sigma t} dx = 0$. Consequently, to calculate the rate of change in the free energy, we can ignore the contribution from γ_h , and express it as the difference due to the initial and perturbed film thickness at any position x [97] as:

$$\Delta \dot{F} = \frac{\partial}{\partial t} \left[\frac{1}{2} \gamma \left| \frac{\partial h}{\partial x} \right|^2 + \frac{1}{2} \Pi'' \Big|_{h_o} \Delta h^2 \right] = \sigma \left(\gamma k^2 + \frac{A}{2\pi h_0^4} \right) \varepsilon^2 e^{2(\sigma t - ikx)} \quad (3.9)$$

The first term in the expression on the right hand side is the rate of increase of surface tension energy, and the second one is the rate of change in energy from the dispersive interaction.

3.4 Results and Discussion

3.4.1 Dispersion relation for classical dewetting

Here we compare the characteristic dewetting length scales obtained from fluid dynamics versus the thermodynamic approach. The typical approach to obtain the dispersion relation between the rate σ and wave vector k has been to describe the rate of change in film height based on the NS equation and mass conservation [96, 97]. For the classical dewetting instability, i.e. without Marangoni effects, the resulting dynamics is described by the equation [162, 43]:

$$3\eta \frac{\partial h}{\partial t} = -\nabla \cdot \left(\gamma h^3 \nabla \cdot \nabla^2 h - \frac{A}{2\pi h} \nabla h \right) \quad (3.10)$$

As is evident, this equation is non-linear in h and presents considerable challenges towards achieving an analytical description of dewetting that could provide simple but physically insightful information about the instability. Consequently, a prevalent approach is a solution afforded by linear stability analysis. Hence, after an expansion of the right hand side of Eq. 3.10:

$$3\eta \frac{\partial h}{\partial t} = \quad (3.11)$$

$$(-k^2 \varepsilon e^{\sigma t - ikx}) \left(\gamma k^2 (h_o^3 + 6h_o^2 \varepsilon e^{\sigma t - ikx} + 9h_o \varepsilon^2 e^{2(\sigma t - ikx)} + 4\varepsilon^3 e^{3(\sigma t - ikx)}) + \frac{Ah_o}{2\pi(h_o + \varepsilon e^{\sigma t - ikx})^2} \right)$$

and applying by keeping terms only linear in the perturbation amplitude ε , as required by LSA, Eq. 3.11 reduces to :

$$3\eta (\varepsilon \sigma e^{\sigma t - ikx}) = (-k^2 \varepsilon e^{\sigma t - ikx}) \left(\gamma k^2 h_o^3 + \frac{A}{2\pi h_o} \right) \quad (3.12)$$

Consequently, the resulting dispersion relation is given by [12]:

$$\sigma_C^{LSA} = -\frac{h_o^3 k^2}{3\eta} \left(\gamma k^2 + \frac{A}{2\pi h_o^4} \right) \quad (3.13)$$

The characteristic (or classical) dewetting length scale Λ_C^{LSA} can be obtained from the dispersion relation by the maxima condition $\frac{d\sigma}{dk} = 0$ and leads to:

$$\Lambda_C^{LSA} = \left(-\frac{8\pi^2 \gamma h_o^3}{\frac{A}{2\pi h_o}} \right)^{1/2} = \sqrt{-\frac{16\pi^3 \gamma}{A} h_o^2} \quad (3.14)$$

where the superscript refers to LSA.

On the other hand, the thermodynamic (TH) approach is based on equating the rate of free energy change (Eq. 3.9) to the total viscous dissipation in the film. We can calculate the total viscous dissipation per unit area \dot{E} for the liquid film by integrating over the film thickness as follows:

$$\dot{E}_C = \int_0^{h_0} \dot{e}_C dz = \frac{(\nabla P)^2}{3\eta} h_0^3 \quad (3.15)$$

The next, and important, step in evaluating this integral is to relate the pressure gradient to the film height through a volume conservation argument. Volume conservation requires that the rate of change of film height $\partial h/\partial t$ be related to the flux of liquid flow $J(x)$ as $\partial h/\partial t = -\nabla \cdot J(x)$. To evaluate this we have used the thin film lubrication approximation in which flux can be written in terms of the height-averaged liquid velocity $\langle v \rangle$ as [160]:

$$J(x) = h_o \langle v \rangle = h_o \cdot \left(\frac{1}{h_o} \int_0^{h_o} v dz \right) = -\frac{\nabla P}{3\eta} h_o^3 \quad (3.16)$$

from which we can express the volume conservation equation as:

$$\frac{\partial h}{\partial t} = -\nabla \cdot J = \frac{\nabla^2 P}{3\eta} h_o^3 \quad (3.17)$$

By rearranging terms we get the desired relation for the pressure gradient as follows:

$$\nabla P = \int \nabla^2 P dx = \frac{i}{k} \left(\frac{3\eta\sigma}{h_o^3} \right) \epsilon e^{\sigma t - ikx} \quad (3.18)$$

where we have made use of Eq. 3.7. Using this expression in Eq. 3.15, the total dissipation is:

$$\dot{E}_C = -\frac{3\eta}{h_o^3 k^2} \sigma^2 \epsilon^2 e^{2(\sigma t - ikx)} \quad (3.19)$$

Then, equating Eq. 3.19 with the rate of decrease of free energy, Eq. 3.9, $\Delta \dot{F} = \dot{E}_C$, and expressing the result in terms of σ we get the dispersion relation from the thermodynamic approach:

$$\sigma_C^{TH} = -\frac{h_o^3 k^2}{3\eta} \left(\gamma k^2 + \frac{A}{2\pi h_o^4} \right) \quad (3.20)$$

from which, the classical dewetting length scale Λ_C^{TH} can be expressed as:

$$\Lambda_C^{TH} = \left(-\frac{8\pi^2 \gamma h_o^3}{\frac{A}{2\pi h_o}} \right)^{1/2} = \sqrt{-\frac{16\pi^3 \gamma}{A} h_o^2} \quad (3.21)$$

where the superscript and subscript refers to thermodynamic. As expected, the fluid dynamics described by LSA and the TH approach give identical results for the classical dewetting instability [163, 158]. On the other hand, as we show next, dewetting with Marangoni (or Thermocapillary) forces requires a more stringent evaluation of the viscous dissipation in order to provide results comparable to LSA.

3.4.2 Dispersion relation for thermocapillary dewetting from thermodynamics

As in the previous section, we analyze the LSA and TH approaches for dewetting in the presence of thickness-dependent Marangoni effects. In order to relate our work to experimental observations, we describe LSA results for the case when ultrathin metal films on SiO₂ substrates are melted by nanosecond ultraviolet wavelength laser pulses [41, 104]. In this situation, there is a strong thickness-dependent reflection and absorption of light by the thin metal film which leads to a local h -dependent temperature of the liquid metal film [105]. In addition, as reported previously, the temperature gradient along the plane of the film, dT/dx , generated by this nanoscale heating effect, can have a positive or negative sign depending upon the initial film thickness h_o [12]. With this, the boundary condition describing the h -dependent Marangoni effect can be rewritten in the form of a thermocapillary effect as follows:

$$\eta \frac{dv}{dz} \Big|_{h_o} = \frac{d\gamma(h)}{dh} \frac{dh}{dx} = - |\gamma_T| T_h h' \quad (3.22)$$

Where $\gamma_T = \frac{d\gamma}{dT}$ is the temperature coefficient of surface tension, $T_h = dT/dh$ is the film height-dependent temperature and $h' = dh/dx$. Given that all metals have a negative value of γ_T , we have expressed the boundary condition in a more conventional form using $\gamma_T = -|\gamma_T|$. In this scenario, the resulting dynamical equation of the film height is given by:

$$3\eta \frac{\partial h}{\partial t} = -\nabla \cdot \left(\gamma h^3 \nabla \cdot \nabla^2 h - \frac{A}{2\pi h} \nabla h + \frac{3}{2} h^2 \nabla \gamma \right) \quad (3.23)$$

Applying steps similar to the classical case (see Eq. 3.11), the right hand side of Eq. 3.23 is:

$$\begin{aligned} 3\eta \frac{\partial h}{\partial t} = & (-k^2 \epsilon e^{\sigma t - ikx}) \left(\gamma k^2 (h_o + \epsilon e^{\sigma t - ikx})^2 (h_o + 4\epsilon e^{\sigma t - ikx}) \right. \\ & \left. + \frac{Ah_o}{2\pi (h_o + \epsilon e^{\sigma t - ikx})^2} + 3 |\gamma_T| T_h (h_o + \epsilon e^{\sigma t - ikx}) \left(\frac{h_o}{2} + \frac{3}{2} \epsilon e^{\sigma t - ikx} \right) \right) \end{aligned} \quad (3.24)$$

which, upon applying LSA, reduces to:

$$3\eta (\epsilon \sigma e^{\sigma t - ikx}) = (-k^2 \epsilon e^{\sigma t - ikx}) \left(\gamma k^2 h_o^3 + \frac{A}{2\pi h_o} + \frac{3}{2} h_o^2 |\gamma_T| T_h \right) \quad (3.25)$$

and the resulting dispersion relation is[12]:

$$\sigma_{TC}^{LSA} = -\frac{h_o^3 k^2}{3\eta} \left(\gamma k^2 + \frac{A}{2\pi h_o^4} + \frac{3}{2} \frac{|\gamma_T| T_h}{h_o} \right) \quad (3.26)$$

From Eq. 3.26 the characteristic dewetting length scale in the presence of thermocapillary effects, Λ_{TC}^{LSA} , can be expressed as:

$$\Lambda_{TC}^{LSA} = \frac{2\pi}{k} = \left(-\frac{16\pi^3 \gamma}{A + 3\pi |\gamma_T| h_o^3 T_h} \right)^{1/2} h_o^2 \quad (3.27)$$

where the superscript TC denotes thermocapillary.

Next we evaluate the length scale using the TH approach based on evaluating the the total viscous dissipation per unit area \dot{E} for the liquid film. First, the dissipation per unit volume expressed in terms of the thermocapillary boundary condition is:

$$\dot{e}_{TC} = \eta \left(\frac{dv}{dz} \right)^2 = \frac{\nabla P^2}{\eta} (z - h_o)^2 - 2\nabla P \frac{|\gamma_T | T_h h'}{\eta} (z - h_o) + \frac{(|\gamma_T | T_h h')^2}{\eta} \quad (3.28)$$

The total viscous dissipation per unit area \dot{E} for the liquid film is now:

$$\dot{E}_{TC} = \int_0^{h_o} \dot{e}_{TC} dz = \frac{\nabla P^2}{3\eta} h_o^3 + \nabla P \frac{|\gamma_T | T_h h'}{\eta} h_o^2 + \frac{(|\gamma_T | T_h h')^2}{\eta} h_o \quad (3.29)$$

Again, the next step in evaluating this integral is to relate the pressure gradient to the film height through volume conservation arguments, as done for the classical case.

$$J(x) = h_o \langle v \rangle = h_o \cdot \left(\frac{1}{h_o} \int_0^{h_o} v dz \right) = -\frac{\nabla P}{3\eta} h_o^3 - \frac{|\gamma_T | T_h h' h_o}{2\eta} \quad (3.30)$$

from which we can express the volume conservation equation as:

$$\frac{\partial h}{\partial t} = -\nabla \cdot J = \frac{\nabla^2 P}{3\eta} h_o^3 + \frac{|\gamma_T | T_h h'' h_o^2}{2\eta} \quad (3.31)$$

By rearranging terms and substituting the height perturbation, Eq. 3.7, into above we get:

$$\nabla^2 P = \frac{3\eta}{h_o^3} \epsilon e^{\sigma t - ikx} + \frac{3|\gamma_T | T_h k^2}{2h_o} \epsilon e^{\sigma t - ikx} \quad (3.32)$$

The pressure gradient along the x-direction can now be obtained by integrating Eq. 3.32 as follows:

$$\nabla P = \int \nabla^2 P dx = \frac{i}{k} \left(\frac{3\eta \sigma}{h_o^3} + \frac{3|\gamma_T | T_h k^2}{2h_o} \right) \epsilon e^{\sigma t - ikx} \quad (3.33)$$

Then, on substituting the above relation for pressure gradient into Eq. 3.29, we get the total viscous dissipation:

$$\begin{aligned} \dot{E}_{TC} = & \left\{ - \left(\frac{3\eta}{h_o^3 k^2} \sigma^2 + \frac{3|\gamma_T | T_h}{h_o} \sigma + \frac{3(|\gamma_T | T_h)^2 k^2 h_o}{4\eta} \right) \right. \\ & \left. + \left(\frac{3\eta |\gamma_T | T_h}{h_o^3} \sigma + \frac{3(|\gamma_T | T_h)^2 k^2}{2h_o} \right) \frac{h_o^2}{\eta} - \frac{h_o}{\eta} (|\gamma_T | T_h)^2 k^2 \right\} \epsilon^2 e^{2(\sigma t - ikx)} \end{aligned} \quad (3.34)$$

Finally, equating Eq. 3.34 with the rate of decrease of free energy, Eq. 3.9 and rearranging the equation in terms of σ we get an analytical dispersion expression for thermocapillary dewetting as:

$$\sigma^2 + \frac{h_0^3 k^2}{3\eta} \left(\gamma k^2 + \frac{A}{2\pi h_0^4} \right) \sigma + \left(\frac{h_0^3 k^2}{3\eta} \right) \frac{(|\gamma_T| T_h)^2 k^2 h_0}{4\eta} = 0 \quad (3.35)$$

It is important to note that Eq. 3.35, which comes from the thermodynamic approach, differs from the LSA result, Eq. 3.26. One can note that there is substantial difference between the two solutions. The TH approach is quadratic in σ as well as $|\gamma_T| T_h$ (Eq. 3.35), while, in the LSA case (Eq. 3.26) it is linear in both quantities. Consequently, the TH approach does not directly lead to the linear dependence on $|\gamma_T| T_h$ as evident from LSA (Eq. 3.26). This is especially important since, as noted earlier, the thermal gradients generated by pulsed laser heating can have positive or negative signs and hence lead to fundamentally different dewetting behaviors [12, 44]. Since the TH dispersion is a quadratic function of the thermal gradient, its behavior will be independent of the sign of the thermal gradient and so does not agree with LSA. As we show next, it is necessary to evaluate the characteristics of dissipation in order to get the correct behavior from TH.

3.4.2.1 Dispersion using minimum viscous dissipation

In the classical case, the total viscous dissipation is uniquely defined by the magnitude of the pressure gradient for any given film thickness, as evident from Eq. 3.15. On the other hand, the total dissipation for thermocapillary dewetting is not unique, and, in fact, varies with the magnitude of the thermal gradient for any given pressure gradient, as evident from Eq. 3.29. It is this behavior that is responsible for the above discrepancy between LSA and TH and can be resolved by evaluating the minimum viscous dissipation.

The minimum viscous dissipation for the fluid being subjected to pressure gradients can be estimated from the differential condition $d\dot{e}/d\nabla P = 0$. Using Eq. 3.28, this leads to the condition $\nabla P(z - h_0) = |\gamma_T| T_h h'$. The general solutions satisfying the above equality can be evaluated for various values of height z in relation to the thickness h_o . First, the condition $z = h_0$ does not yield a unique relation between ∇P and $|\gamma_T| h'$ and is therefore not a useful solution in the context of the dissipation. On the other hand, the choice of $z = 0$, yields the case of $\nabla P = -\frac{|\gamma_T| T_h h'}{h_0}$. By utilizing Eq. 3.4, one can see that the physical interpretation of this condition is that the tangential stress at the film-substrate interface at $z = 0$ is zero. The resulting viscous dissipation for thermocapillary dewetting will now be (from Eq. 3.28):

$$\dot{e}_{TC}^m = \frac{(\nabla P z)^2}{\eta} \quad (3.36)$$

where the superscript m signifies a minimum. One can verify that this is a minima by noting that the second derivative $d^2 \dot{e}_v / d^2 \nabla P$ is positive. Therefore, the minimum dissipation per unit area of the film \dot{E}_{TC}^m can be obtained as:

$$\dot{E}_{TC}^m = \int_0^{h_o} \dot{e}_{TC}^m dz = \frac{(\nabla P)^2 h_0^3}{3\eta} \quad (3.37)$$

Using the form of ∇P from Eq. 3.33, the relevant form of \dot{E}_{TC}^m is:

$$\dot{E}_{TC}^m = - \left(\frac{3\eta}{h_0^3 k^2} \sigma^2 + \frac{3|\gamma_h|}{h_0} \sigma + \frac{3(|\gamma_h|)^2 k^2 h_0}{4\eta} \right) \varepsilon^2 e^{2(\sigma t - ikx)} \quad (3.38)$$

Finally, by equating the rate of free energy change ΔF (Eq. 3.9) and the minimum viscous dissipation rate \dot{E}_{TC}^m (Eq. 3.38), we obtain an analytical form of the dispersion relation as:

$$\sigma^2 + \frac{h_0^3 k^2}{3\eta} \left(\gamma k^2 + \frac{A}{2\pi h_0^4} + \frac{3|\gamma_T| T_h}{h_0} \right) \sigma + \frac{h_0^3 k^2}{3\eta} \frac{3}{4\eta} (|\gamma_T| T_h)^2 h_0 k^2 = 0 \quad (3.39)$$

This result is clearly different from Eq. 3.35 because now, the linear behavior with $|\gamma_T| T_h$ is also present. Next, we evaluate this quadratic equation in σ for various magnitudes of the thermal gradients and show that it is identical to the LSA results for large thermal gradients. By defining $f = \gamma k^2 + A/2\pi h_0^4$ and $g = (3|\gamma_T| T_h)/h_0$, the roots of the dispersion relation are:

$$\sigma_{\pm} = -\frac{h_0^3 k^2}{6\eta} (f + g) \pm \frac{h_0^3 k^2}{6\eta} \sqrt{(f + g)^2 - g^2} \quad (3.40)$$

1. Minimum dissipation approach for classical case (i.e. $T_h = 0$)

By substituting $T_h = g = 0$ in Eq. 3.40, the resulting relevant root is:

$$\sigma_- = -\frac{h_0^3 k^2}{3\eta} \left(\gamma k^2 + \frac{A}{2\pi h_0^4} \right) \quad (3.41)$$

As expected, this result is identical to the result for the classical dewetting instability.

2. Minimum dissipation approach for strong thermal gradients

In the case when the magnitudes of the thermal gradients are larger than the attractive dispersion forces, i.e. for example when $3|\gamma_T T_h| \geq |A/2\pi h_0^4|$, then we have $|g| > |f|$. This is the condition found in the experimental cases reported earlier [12, 44], and we can obtain an approximate solution from Eq. 3.40 as follows:

$$\sigma_{\pm} \approx -\frac{h_0^3 k^2}{6\eta} (f + g) \pm \frac{h_0^3 k^2}{6\eta} \sqrt{g^2 - g^2} = -\frac{h_0^3 k^2}{6\eta} (f + g) \quad (3.42)$$

or

$$\sigma_{TC}^{TH} = -\frac{h_0^3 k^2}{3\eta} \left(\gamma k^2 + \frac{A}{2\pi h_0^4} + \frac{3|\gamma_T| T_h}{h_0} \right) \quad (3.43)$$

From Eq. 3.43, the characteristic wavelength Λ_{TC}^{TH} obtained from the maxima in the dispersion given by $d\sigma/dk = 0$ is:

$$\Lambda_{TC}^{TH} = \sqrt{-\frac{16\pi^3\gamma}{A + 6\pi|\gamma_T|T_h h_o^3} h_o^2} \quad (3.44)$$

Comparing with the LSA result, Eq. 3.27, the only difference is in the factor of two multiplying the thermal gradient term. More importantly, the functional dependence on h_o , A , γ and $|\gamma_T|T_h$ remains the same, confirming that the minimum dissipation approach gives similar physical characteristics for the dewetting instability. An important benefit of utilizing the thermodynamic approach is also evident here. From the above dissipation analysis it is clear that there are multiple choices for the dewetting pathway in regards to the rate of dissipation. However the instability clearly picks the path which minimizes the rate of this dissipation, or in other words, minimizes the overall rate at which energy is lost in the dewetting process. We have also plotted the behavior of the dispersion relation, Eq. 3.43 for Co films on SiO₂ substrates with the various materials parameter values being: Hamaker coefficient $A = -1.41 \times 10^{-18}$ J, $\gamma = 1.88$ J/m² and $\gamma_T = -4.8 \times 10^{-3}$ J/m² - K. Fig. 3.1(a) plots the growth rate σ versus wave number k for the dispersion relation Eq. 3.43. The data was evaluated for Co film of thickness 8 nm and various values of the gradient T_h , including $T_h = 0$, $T_h > 0$ and $T_h < 0$, as indicated on the plot. In Fig. 3.1(b)) we have plotted the characteristic length scale Λ_{TC}^{TH} for Co films on SiO₂ as a function of varying thickness and various T_h . The decrease in length scale with increase in the magnitude of $T_h < 0$ is evident. In Fig. 3.1(c) the cut-off wavelength $\Lambda_{cut-off}^{TH}$ as a function of varying thickness and various T_h is plotted. The cut-off wavelength corresponds to the intersection of the growth rate with the wave number axis in Fig. 3.1(a).

3. Minimum dissipation approach for weak thermal gradients

In the case when the magnitudes of the thermal gradients are smaller then the attractive dispersion forces, i.e. for example when $3|\gamma_T T_h| < |A/2\pi h_o^3|$, then we have $|g| < |f|$. In this situation, we can approximate Eq. 3.40 as follows:

$$\sigma_{\pm} \cong -\frac{h_o^3 k^2}{6\eta}(f+g) \pm \frac{h_o^3 k^2}{6\eta} \sqrt{f^2 - g^2} \cong -\frac{h_o^3 k^2}{6\eta}(f+g) \pm \frac{h_o^3 k^2}{6\eta} f \left(1 - \frac{g^2}{2f^2}\right) \quad (3.45)$$

where we have used the binomial approximation $(1 - (g/f)^2)^{1/2} \sim (1 - g^2/2f^2)$. Here we find again that the dispersion is considerably different from the LSA result of Eq. 3.26.

3.5 Conclusion

We have theoretically evaluated the classical and thermocapillary dewetting instability in thin fluid films via a thermodynamic approach. In this, the rate of change of free energy is equated to the viscous dissipation in the thin film. The thermodynamic approach leads to an analytical expression for the dispersion without

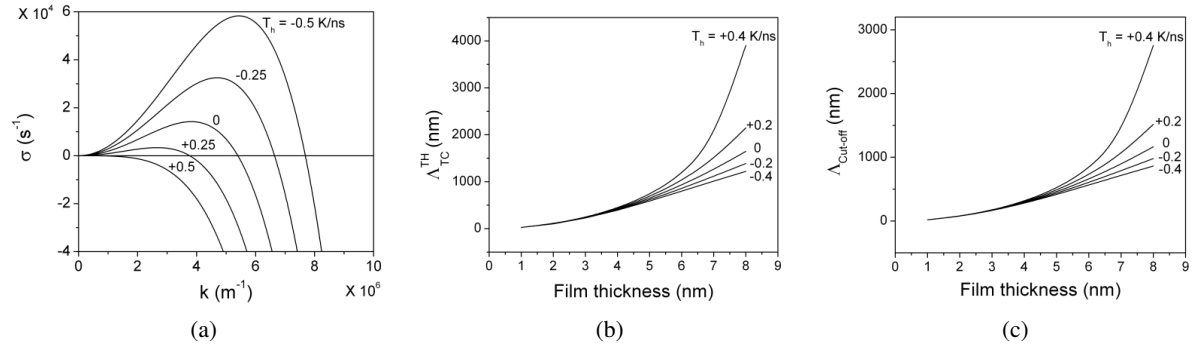


Figure 3.1: (a) Plot of the growth rate versus wave number for the dispersion relation obtained from the dissipation approach for strong thermal gradients. The data was evaluated for Co film of thickness 8 nm and various values of the gradient T_h , as indicated on the plot. (b) Plot of the characteristic length scale Λ_{TC}^{TH} for Co films on SiO₂ as a function of various T_h . (c) Plot of the cut-off wavelength $\Lambda_{Cut-off}$ for Co films on SiO₂ as a function of various T_h . The cut-off wave number corresponds to the intersection of the rate with the wave number axis in Fig. (a).

the need for explicit solution of the height evolution dynamical equation from NS within the lubrication approximation. We have compared results from this approach to existing results obtained by linearization of the fluid dynamics of the thin film. For the case of classical dewetting in the presence of surface tension and long range attractive forces, the thermodynamic approach predicts identical behavior to that from linear analysis. We have also evaluated dewetting in the presence of film-thickness dependent temperature variations. Such a situation can be found during dewetting of thin metallic films melted by a nanosecond ultraviolet pulsed laser. In this condition, a film thickness dependent reflection and absorption leads to thermocapillary forces along the plane of the film. In this scenario we found that the thermodynamic approach agrees with linear analysis provided the minimum viscous dissipation is evaluated. The fluid flow condition that gives minimum viscous dissipation is one where the film-substrate tangential stress is zero. In the context of dewetting in the presence of film thickness dependent thermocapillary forces, the thermodynamic approach clearly illustrates that the instability chooses a pathway which minimizes the rate of energy loss in the system. This results shows that the thermodynamic approach based on evaluating the rates of free energy change and energy loss is a simple but potentially powerful way to gain physically meaningful insight into such spontaneous pattern formation processes.

Chapter 4

Implementation and testing of surface magneto-optical Kerr effect (SMOKE) system

(Reported to Proc. SPIE, 7767, 77670Q (2010))

Magnetic measurement of pulsed laser-induced nanomagnetic arrays using Surface Magneto-Optic Kerr effect

4.1 Summary

Efficient and dependable characterization methods of magnetic-plasmonic nanostructures are essential towards the implementation of new nanoscale materials in magneto-optical applications. Surface magneto-optic Kerr effect (SMOKE) is a powerful characterization technique, because of its simplicity and high sensitivity to even monolayer thick magnetic materials. It relies on the measurement of polarization and absorption changes of reflected light in the presence of a magnetic field. A homebuilt SMOKE system was successfully installed and tested on plasmonic-ferromagnetic (PF) composites to characterize their magnetization properties. The system allows SMOKE measurements in various configurations (i.e. polar and longitudinal) in a magnetic field of up to 0.7 T. Here we have measured the magneto-optical Kerr rotation in multimetal systems comprised of Ag and Co arranged in various geometries and shapes. Specifically, thin film structures in bilayer and single layer composite geometry (with various compositions), as well as nanoparticles of Ag-Co, were investigated for Kerr rotation at 635 nm wavelength. The co-deposited film with 67% Co showed Kerr rotation of 6×10^{-3} degrees, which was higher than that from bilayer structures with same effective amount of Co and Ag. Furthermore, nanoparticles showed a factor of 2 or higher Kerr rotation compared to composite films of similar Co composition ranging between 35 to 100%. Systematic differences in saturation and coercivity were observed for the different samples. These results demonstrated that SMOKE is a reliable technique to rapidly characterize the magnetic behavior of nanoparticle arrays.

4.2 Introduction

Accurate and simple characterization of the functional behavior of nanomaterials is an important task. Magnetic materials are used in a variety of basic and technological fields, including as chemical sensors, probes of transport behavior of materials, and in information processing. The magnetization behavior of nanostructured materials with complex shapes, crystalline states, and internal state of strain, are of ongoing interest in the continuing drive to improve and advance the science and technology of materials behavior. For that reason, particular attention has been given to surface magneto-optic Kerr effect (SMOKE) as a tool to investigate magnetism of nanostructures. SMOKE is a relatively straightforward characterization technique, and provides a reliable means of probing magnetic ultra thin films and nanostructures. SMOKE offers some important advantages suited for nanostructures, including its high sensitivity and the ability to locally probe the surface [89, 164]. SMOKE is more sensitive than superconducting quantum interference devices (SQUID) magnetometry [165] for studying nanoscopic volume of magnetic materials. In addition, the experimental SMOKE setup is relatively simple and cost-effective and is therefore accessible to a wide variety of researchers. Essentially, SMOKE operates on the principle of a complex rotation of the plane of polarization of linearly polarized incident light upon reflection from the surface of magnetic material [79, 166]. The rotation is linearly proportional to the magnetization of the material within the probing region of the light [79, 166]. Hence, the measured rotation values as a function of applied magnetic field yields the magnetic hysteresis loop.

One of the advantages of the SMOKE system is that the probing mechanism is based on magneto-optical (MO) effects. In the long term our groups research is interested in investigating new materials for high M-O effects, which have applications in chemical and biomolecular sensing applications. One candidate material is a plasmonic-ferromagnetic (PF) material which simultaneously shows ferromagnetism, SPR (which is the collective resonant oscillation of free electrons), and magneto-optical (MO) response. Investigators have shown that PF material shows enhanced M-O effect at the plasmon resonance frequency. Hence, the PF material can utilize the power of SPR sensing with the added benefit of improved sensitivity and detection limits based on measuring the relatively enhanced MO response at the resonance condition. According to previous studies, in order to design PF materials, SPR materials (Au, Ag, Cu) and M-O materials (Co, Fe, Ni, Fe₂O₃, YIG) need to be combined together as composites, i.e. without chemical binding to form alloys or compounds [74, 75, 80, 81]. One potential combination to get such PF materials is a mixture of a ferromagnetic metal like Co, with a plasmonic material like Ag. From the binary phase diagram, Co and Ag is an immiscible system, both in their liquid phase as well as solid phase. Therefore combining Co with Ag in various concentrations can potentially lead to MO materials with variable SPR frequencies.

In this study, the SMOKE system was built in house with components purchased from various vendors. The system was integrated with a computer interface via LabVIEW™ and was tested. Co-deposited and bilayered Co-Ag films were prepared on SiO₂/Si substrates. The magneto-optical (MO) signals, specifically Kerr signals were measured with varying film type (bilayer vs composite) and composition using SMOKE at 635 nm wavelength. Furthermore, the Kerr signal dependence on the shape of PF materials was also studied by comparing response from the film and nanoparticles. The functionality of the SMOKE system was verified by measuring Kerr rotation hysteresis loop of the samples.

4.3 SMOKE system

Details of the automated surface magneto-optical Kerr effect (SMOKE) system operating at room temperature are discussed, with specifics of the hardware software.

4.3.1 Theory

Before going through the details of SMOKE system, a brief history and mechanism of magneto-optical (M-O) effects is discussed. In general, the M-O effects are interactions between light and matter when the matter is under a magnetic field. There are several types of M-O effects including Faraday, Kerr, Cotton-Mouton and Voigt effects.

4.3.1.1 Faraday effect / Cotton-Mouton effect

In 1845 Michael Faraday discovered that when linearly polarized light passes through a glass in a direction parallel to an applied magnetic field, the plane of polarization is rotated [167]. The angle of rotation, θ , is proportional to the magnitude of the magnetic field, H and the distance t , which is the distance travelled by light in the medium. The rotation was given by:

$$\theta = VHt$$

where V is the Verdet constant and varies between 0.1 to 10 minute/Oe cm [79]. Since glass is a diamagnetic material, its Verdet constant is relatively small, of the order of 1×10^{-4} degree/A [79]. For a ferromagnetic material, the angle of rotation is proportional to the magnetization M as follows:

$$\theta = KMt$$

where K is the Kundt constant, and is typically around 350 degrees/gauss-cm. Similarly, the Cotton-Mouton effect (or Voigt effect) is the observation of magnetic birefringence when a magnetic field is applied perpendicular to the path of light. In comparison to the Faraday effect it is a much weaker effect, and is proportional to the square of the field.

4.3.1.2 Kerr effect

John Kerr discovered the change of polarization state of reflected light from a polished electromagnet pole in 1877 [168]. In the Kerr effect, linearly polarized light is incident upon the magnetic sample, and the reflected light is elliptically polarized and rotated with respect to the initial angle of linearly polarized incident light. There are three types of magneto-optical Kerr effect depending on the orientation of the magnetization vector relative to the plane of incidence and the surface. When the magnetization vector is normal to the surface, it is called the polar effect. When the magnetization vector is parallel to the reflective surface and parallel or perpendicular to the plane of incidence, it is the longitudinal or transverse effect, respectively. All Kerr effect configurations are shown in Fig. 4.1.

In general, magneto-optical Kerr effect (MOKE) technique has been used widely for the study of bulk magnetic nanostructures. The bulk scale magnetic samples can be characterized by the MOKE technique, which measures change in the state of polarization of polarized light from a surface of the samples. On the other hand, SMOKE technique applies to the case when the sample thickness is less than the skin depth, typically ranging from a few monolayers to few tens of nanometers. This is because when the sample film becomes extremely thin, the Faraday effect for transmitted beams reflected from the substrate, and the associated interference, becomes important. Several works have been done to formulate SMOKE system, which include the traditional Kerr and Faraday effects [89, 169, 170]. A general expression for the Kerr signal, which was developed by Zak et al. can be found here [169].

4.3.2 Experimental setup

In Fig. 4.2(a) and (b) are the experimental schematics of the SMOKE apparatus. The basic set-up consists of a vibration free table which houses the electromagnet, electronics [consisting of two lock-in amplifiers, photoelastic modulator (PEM), and detector] and the optical components (the monochromatic 635 nm diode laser light source, lenses, and glan-thompson polarizers). The randomly polarized monochromatic light passes sequentially through a linear polarizer inclined at a desired angle and an objective lens to decrease beam spot size to $80\ \mu\text{m}$. The polarizer angle is set to produce p-polarized light. A sample holder is located at the center of two adjustable pole pieces of the electromagnet, and the sample orientation with respect to the external magnetic field direction can be freely adjusted. Fig. 4.2(a) describes the polar geometry, where the external magnetic field direction is perpendicular to the sample plane. Fig. 4.2(b) describes the longitudinal geometry, where the external magnetic field direction is parallel to the sample plane. The plane of incidence is parallel to the field in both orientations. The reflected light, after interacting with the sample surface, passes through the PEM and another linear polarizer, which functions as an analyzer. The analyzer angle is set to 45° . The PEM at 50 kHz provides a reference signal ($1f = 50\ \text{kHz}$ and $2f = 100\ \text{kHz}$) for each lock-in amplifier. The light is detected by a biased high speed silicon detector and the output AC signal is sent to the lock-in amplifier (Stanford Research Systems, SR-830 & SR-530) to filter out unwanted noise. The DC signal from the lock-in amplifier goes to a computer through GPIB bus. The bipolar power supply for the electromagnet is remotely controlled by the computer. The digital interface card makes it possible to control the power supply output by means of digital input signals via the GPIB bus using SCPI commands from the computer. Therefore, the final output is a plot of the intensity of light versus the strength of the magnetic field. This SMOKE system is remotely and automatically controlled through a LabVIEW™ driver. Typically, multiple magnetic field loops were made for the measurements in order to improve the signal-to-noise ratio.

In Table 4.1, all the hardware used in the SMOKE system is listed. The hardware with IEEE-488 port was connected through GPIB cables with the PC.

4.3.2.1 The Kerr rotation and ellipticity from experimental data

Here, we explain how the raw experimental data is converted into Kerr rotation and ellipticity [171]. In order to measure the Kerr rotation and Kerr ellipticity directly from the reflected light intensity, I , we employed a

Table 4.1: *List of hardware used in the SMOKE system.*

Name	Manufacture / Model	Specs
Electromagnet	GMW/ 5403	Pole diam: 76 mm, Max continuous power: 50A/25V
Power Supply & GPIB digital interface card	Kepeco / BOP 20-20M & BIT 4886	Pow. Supply:: DC output range: ± 20 V & ± 20 A GPIB card:: Resolution: 15 bits, Rise/Fall time: $< 100 \mu$ sec
Diode Laser	Thorlabs / LDM635	$\lambda = 635$ nm, 4 mW, Short-term stability (30 min): 0.01 dB, Long-term stability (24 hrs): 0.1 dB
Glan-Thompson polarizer	Thorlabs / GTH10M	Extinction Ratio: 100,000:1, Calcite
Biased Si detector	Thorlabs / DET100A	Peak Response: 0.65 A/W, Rise/Fall Time: 43ns
Lock-in Amplifier	Stanford Research Systems / SRS830 digital lock-in amplifier	Dynamic Reserve: > 100 dB, Input Noise: $6 \text{ nV}/\sqrt{\text{Hz}}$ @1 kHz, 60/120 Hz notch filters
Lock-in Amplifier	Stanford Research Systems / SRS530 analog lock-in amplifier	Dynamic Receive: > 100 dB, Input Noise: $6 \text{ nV}/\sqrt{\text{Hz}}$ @1 kHz, 60/120 Hz notch filters
Photo elastic modulator	Hinds Instruments / I/FS50 (optical head) & PEM-100 (controller)	Fused silica, Nominal frequency: 50 kHz, RS232 interface
GPIB controller	National Instruments / GPIB-USB-HS	IEEE 488.1 transfer rates: Up to 1.8 Mbps, Buffer size: 64 bits
CCD TV Camera	ELMO / TEB4404	
30X close focus microscope with CCD adapter		Magnification (30x), Working distance (80 mm)

photo-elastic modulator (PEM). The complex Kerr signal is given from the Kerr angle, θ_K , and the ellipticity, ϵ_K , which are both contained in the light intensity detected by the detector, which can be expressed as [171]:

$$I_f(t)/I_0 - 1 = 2J_1(A_0)\epsilon_K \sin \omega t + 2J_2(A_0)\theta_K \cos \omega t$$

where, J_n 's are Bessel function of n th order, I_0 represents DC light intensity, ω is the angular frequency of the PEM, and A_0 is the retardation amplitude of the PEM. Hence, by measuring three voltages V_{dc} , V_f and V_{2f} , the Kerr rotation and ellipticity can be obtained as [171]:

$$\theta_K = \frac{\sqrt{2} V_{2f}}{4J_2 V_0}$$

and

$$\epsilon_K = \frac{\sqrt{2} V_{1f}}{4J_1 V_0}$$

4.3.2.2 Software: Interfacing SMOKE system with PC using LabVIEW

The main front panel of the LabVIEW™ program is shown in Fig. 4.3(a) and (b). The front panel is a GUI that can input all hysteresis measurement parameters and obtain output of the measurement by plotting the hysteresis in real time [Fig. 4.3(a)]. Several measurement parameters, number of hysteresis loops, points per hysteresis loop, iterations per point and range of magnetic field need to be defined before the measurement. Hardware setting parameters, SMOKE setting parameters and sample descriptions can be also saved in an output file [Fig. 4.3(b)]. Following the SMOKE measurement, output data and parameters are saved in the output file.

Fig. 4.5 shows the block diagram of the program, which consists of functional-nodes, hardware drivers and connection wires. All processes of the LabVIEW program including hardware control, dataflow, plotting and data saving are designed and written in the block diagram. For example, the electromagnet power supply and two lock-in amplifiers are controlled by the program through the LabVIEW™ driver. The data in the output file can be automatically imported and analyzed by MATLAB™ GUI. MATLAB™ code performs several data adjustments, such as linear drift adjustment, Kerr signal adjustment and magnetic field vs. voltage curve adjustment. For example, an issue that often arises during SMOKE measurement is a linear shift in the data. This is because of a number of nearly untraceable instabilities in the system such as mechanical vibration, light source instability and electric noise. The linear shift adjustment accurately aligns the data to clarify the hysteresis loops, as demonstrated in Fig. 4.6.

Fig. 4.4(a) shows the static plot of the hysteresis loops from magnetic field vs. the Kerr rotation, θ_K , and ellipticity, ε_K , respectively. Fig. 4.4(b) shows the hysteresis loop after averaged multiple loop measurements.

4.4 Sample preparations and testing

Co and Ag films were deposited using electron beam evaporation technique on commercially available optically smooth SiO₂/Si substrates. The thickness of thermally grown SiO₂ layer was 400 nm. Before film deposition, the substrates were ultrasonically cleaned. Three different types of Co-Ag bimetallic structures were deposited. For Co/Ag/SiO₂ and Ag/Co/SiO₂ structures, the thickness of Co and Ag films were fixed at 6 nm and 3 nm, respectively. For co-deposited Co-Ag structure, thickness of Co film was varied from 4 to 6 nm, and Ag film was varied from 0 to 4 nm. The deposition rate of the e-beam was obtained by performing step height measurement using atomic force microscope (AFM). Following deposition, the samples were irradiated at normal incidence with a pulsed laser beam. The Q-switched Nd:YAG pulsed laser with 266 nm wavelength, 9 ns pulse width and 50 Hz repetition rate was used. The laser energy density of 100 mJ/cm² was used, so that all three different film structures could be completely melted. Approximately 10,000 laser pulses were irradiated on the films to form hemispherical nanoparticles which are in the final state of spontaneous self-organized structures. A scanning electron microscope (SEM, Zeiss Merlin) was used to characterize the nanoparticles.

Surface magneto-optic Kerr effect (SMOKE) technique was employed to measure Kerr rotation from the Co-Ag films and nanoparticles. The longitudinal geometry with 17.6° incident angle and p-polarized incident light was utilized for all the measurements [164, 89].

4.5 Results and discussion

In tables 4.2, 4.3, and 4.4, the results of Kerr rotation (θ_k) measurement for three different experimental comparisons are summarized. In Table 4.2, the variation in θ_k for a composite film with Co volume composition varying from 67 to 100 % is shown. In table 4.3, the bilayer arrangement is compared to a composite film with the same overall ratio of Co to Ag. In Table 4.4, the composite film is compared to the nanoparticles with composition varying between 35 to 100%.

4.5.1 Co-deposited Co-Ag films

In Fig. 4.7, the Kerr rotation in degrees is shown for the composite film as a function of increasing Co volume composition between from 67% to 100%. From SMOKE measurements, we observed the rotation angle, θ_k , increases with increasing Co concentration.

Table 4.2: *Table of co-deposited Co-Ag films parameters on SiO₂/Si substrates, including Co weight percentage and amount of Co and Ag in terms of film thickness. Experimentally measured Kerr rotation, θ_k , values are included.*

Sample	Co (wt. %)	Co (nm)	Ag (nm)	θ_k (degree)
Codep-100	100	6	0	10×10^{-3}
Codep-75	75	6	2	9×10^{-3}
Codep-67	67	6	3	6×10^{-3}

4.5.2 Bilayer vs co-deposited Co-Ag

A list of the different Co-Ag film structures and Kerr signal, θ_k , values are given in Table 4.3. By comparing Kerr signals in terms of structure difference, co-deposited Co-Ag film exhibits highest θ_k value among three samples. Ag/Co/SiO₂ sample shows second highest θ_k value.

Table 4.3: *Table of Co-Ag films with same sample parameters but different film structures: Co/Ag/SiO₂, Ag/Co/SiO₂ and co-deposited Co-Ag films. Experimentally measured Kerr rotation, θ_k , values of each sample are presented.*

Sample	Co (wt. %)	Co (nm)	Ag (nm)	θ_k (degree)
Co/Ag/SiO ₂	67	6	3	3×10^{-3}
Ag/Co/SiO ₂	67	6	3	5×10^{-3}
Co-deposited/SiO ₂	67	6	3	6×10^{-3}

4.5.3 Film vs nanoparticles

In Fig. 4.9(a) and (b), SEM image of the nanoparticles and histogram of the particle size distribution are presented. Average particle diameter is 40 ± 10 nm, 147 ± 25 nm and 178 ± 35 nm. In order to identify the distribution of Co and Ag in each nanoparticle, x-ray mapping analysis in the SEM was performed. In Figs. 4.10(a)-(c), the spatial map of (a) combined Co and Ag, (b) only Co and (c) only Ag in the arrays are shown. From the analysis, the presence of both Co and Ag in each particle was confirmed. In Fig. 4.8, the Kerr rotation in degrees is shown for the co-deposited Co-Ag films and nanoparticles as a function of increasing Co volume composition between from 35% to 100%. From SMOKE measurements, we observed the rotation angle, θ_k , increases with increasing Co concentration for both films and nanoparticles cases. Interestingly, the trend indicates the magnitude of the Kerr rotation is larger for the particles compared to the films. Also, we confirmed that the SMOKE system is capable of detecting the Kerr signal of the Co-Ag composite with Co weight percentage as low as 35%.

Table 4.4: *Table of co-deposited Co-Ag films and Co-Ag nanoparticle arrays with different composition. Each nanoparticle array was synthesized from the Co-Ag film with same composition. Measured Kerr rotation, θ_k , values are listed.*

Sample	Co (wt. %)	Co (nm)	Ag (nm)	Diameter (nm)	θ_k (degree)
Film100	100	4	0	-	2.5×10^{-3}
Film50	50	4	4	-	1×10^{-3}
Film35	35	4	7.5	-	1×10^{-3}
Particle100	100	-	-	40 ± 10	5×10^{-3}
Particle50	50	-	-	147 ± 25	2.7×10^{-3}
Particle35	35	-	-	178 ± 35	2×10^{-3}

4.6 Conclusion

We have successfully installed a homebuilt SMOKE system. Automated SMOKE measurement system was designed and built using LabVIEW and MATLAB GUI. The system can be operated for both polar and longitudinal geometries, and it has capability to detect both the Kerr rotation, θ_k , and ellipticity, ϵ_k , simultaneously. The system can perform multiple hysteresis loops measurement and is capable of real time

data analysis. Following the installation, we have measured the magneto-optical Kerr signal on plasmonic-ferromagnetic (PF) composites by using the SMOKE system. Co-Ag composites films and nanoparticles with different composition, structure and shape were synthesized. The co-deposited films showed increase in Kerr rotation with increasing Co volume composition. We found that the co-deposited film showed the highest Kerr rotation values among co-deposited and bilayer structures with same effective amount of Co and Ag. Further, arrays of Co-Ag hemispherical nanoparticles were prepared by using pulsed laser synthesis technique. SEM micrographs and x-ray mapping analysis confirmed that nanoarrays have well defined monomodal nanoparticles, and each nanoparticle is made of both Co and Ag elements. The nanoparticle showed a factor of 2 or higher Kerr rotation compared to composite films of same Co composition. These results demonstrated that SMOKE is a reliable technique to rapidly characterize the magnetic behavior of nanoparticle arrays.

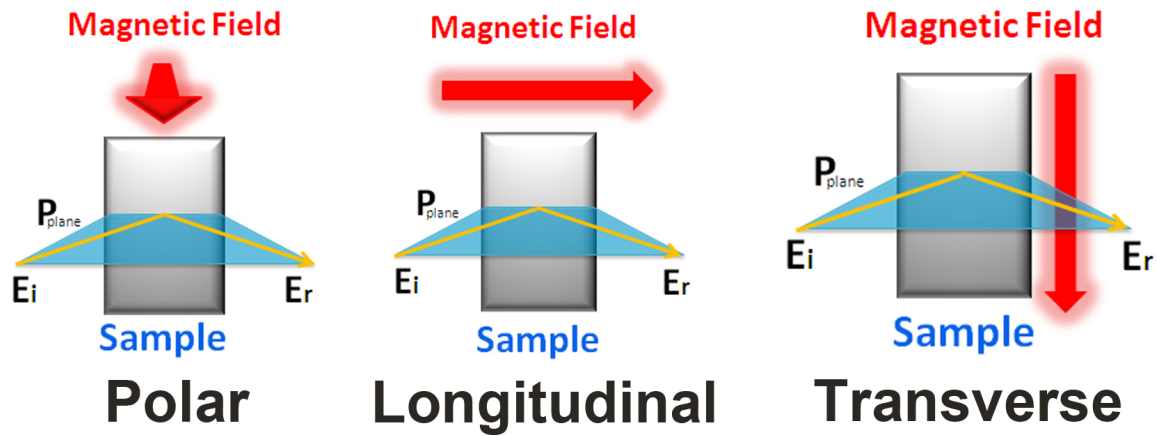


Figure 4.1: Magneto-optical Kerr effects taking place when light reflected from surface of a magnetized material: (left) polar, (center) longitudinal and (right) transverse effects. E_i , E_r and P_{plane} denote incident and reflected electric fields and plane of incidence, respectively [15].

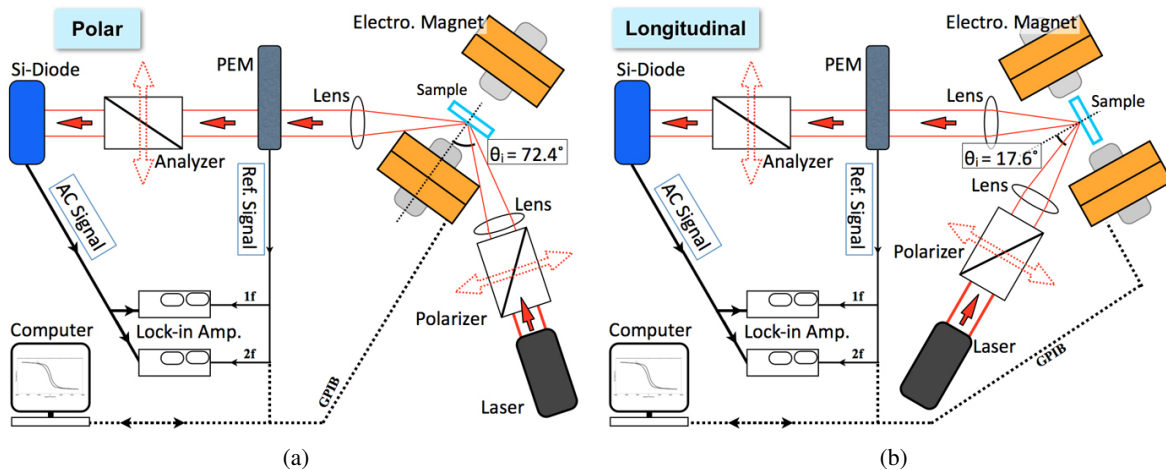
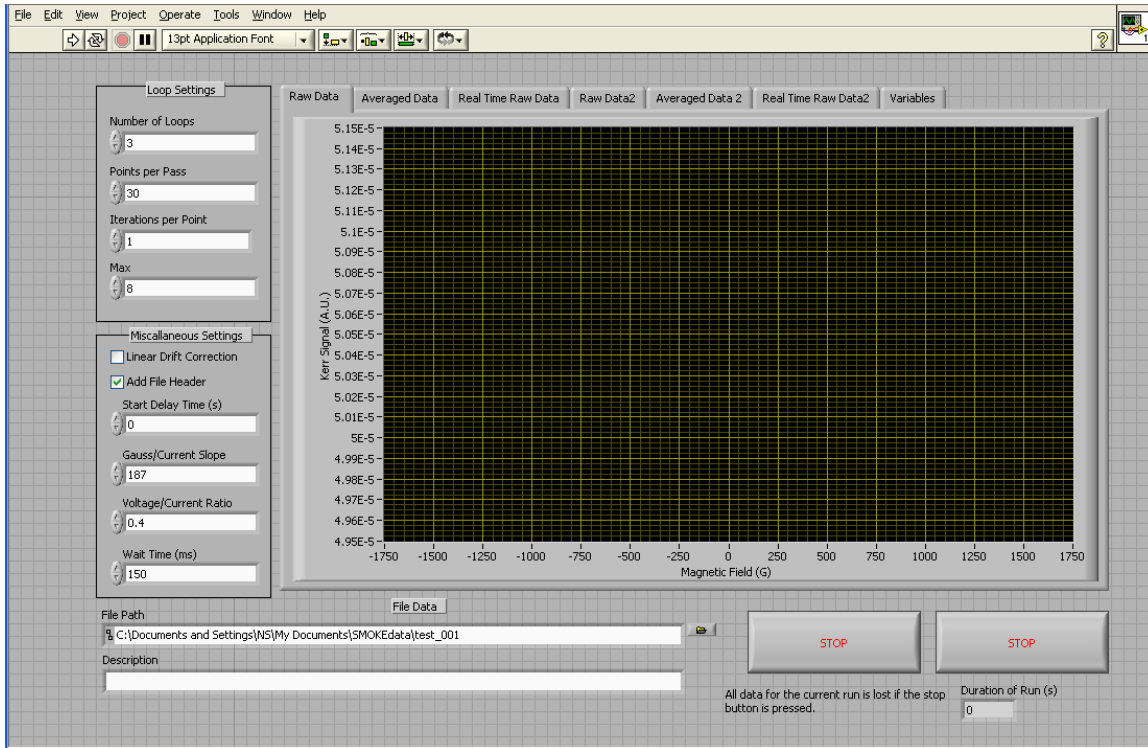
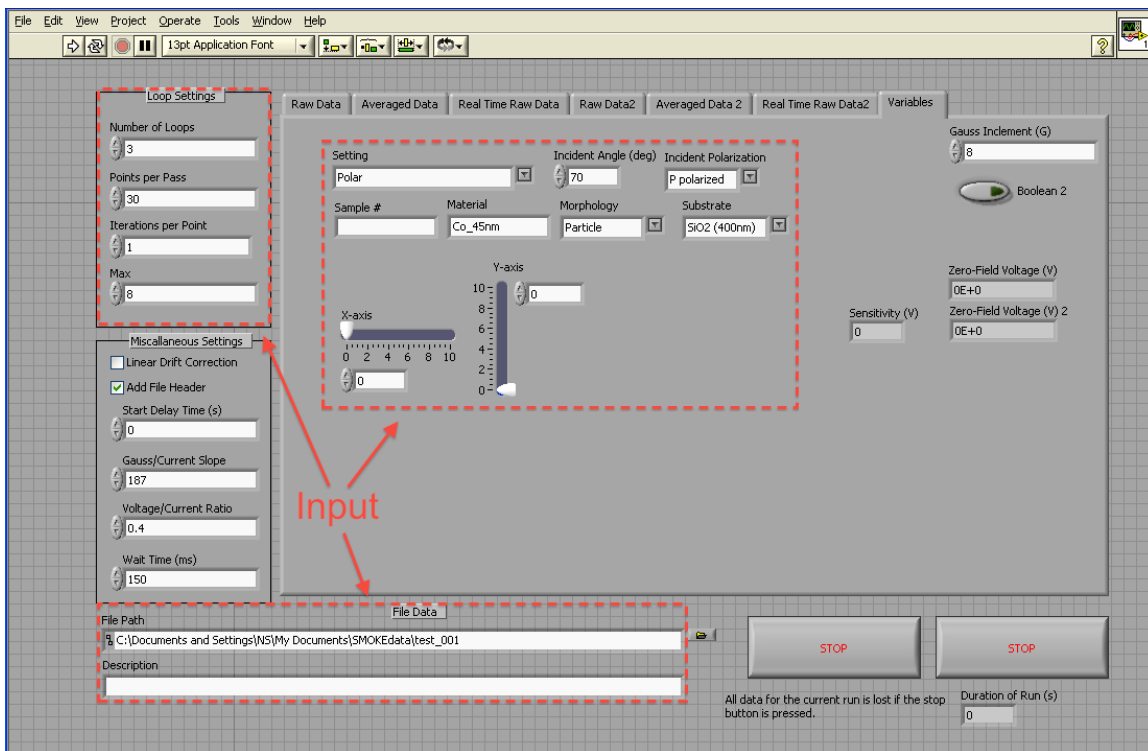


Figure 4.2: Schematic of the SMOKE system in (a) polar and (b) longitudinal geometries.



(a)



(b)

Figure 4.3: Front panel of LabVIEW GUI. (a) Main control and (b) measurement parameters input (indicated with red boxes) panels.

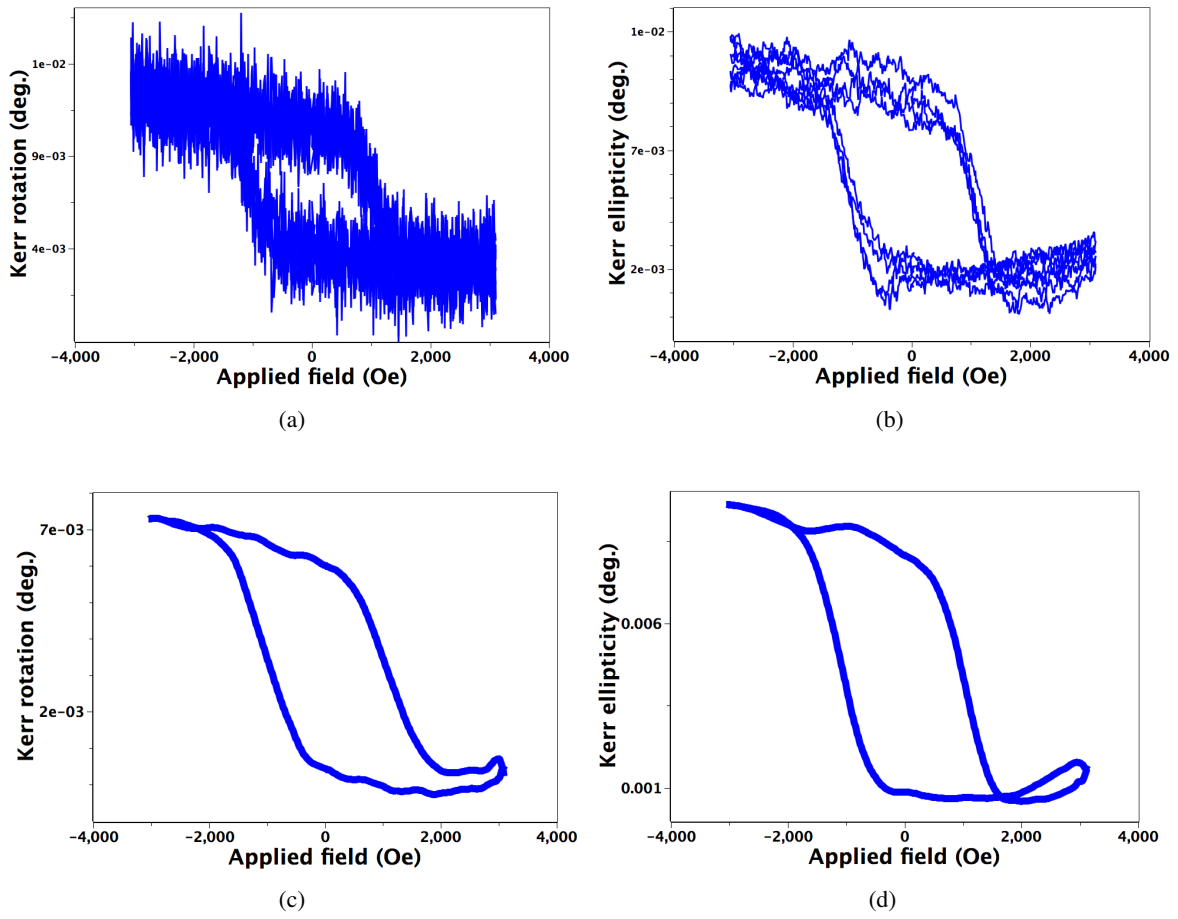


Figure 4.4: *Raw SMOKE hysteresis loops of (a) Kerr rotation and (b) ellipticity, respectively. Averaged SMOKE hysteresis loops of (c) Kerr rotation and (d) ellipticity.*

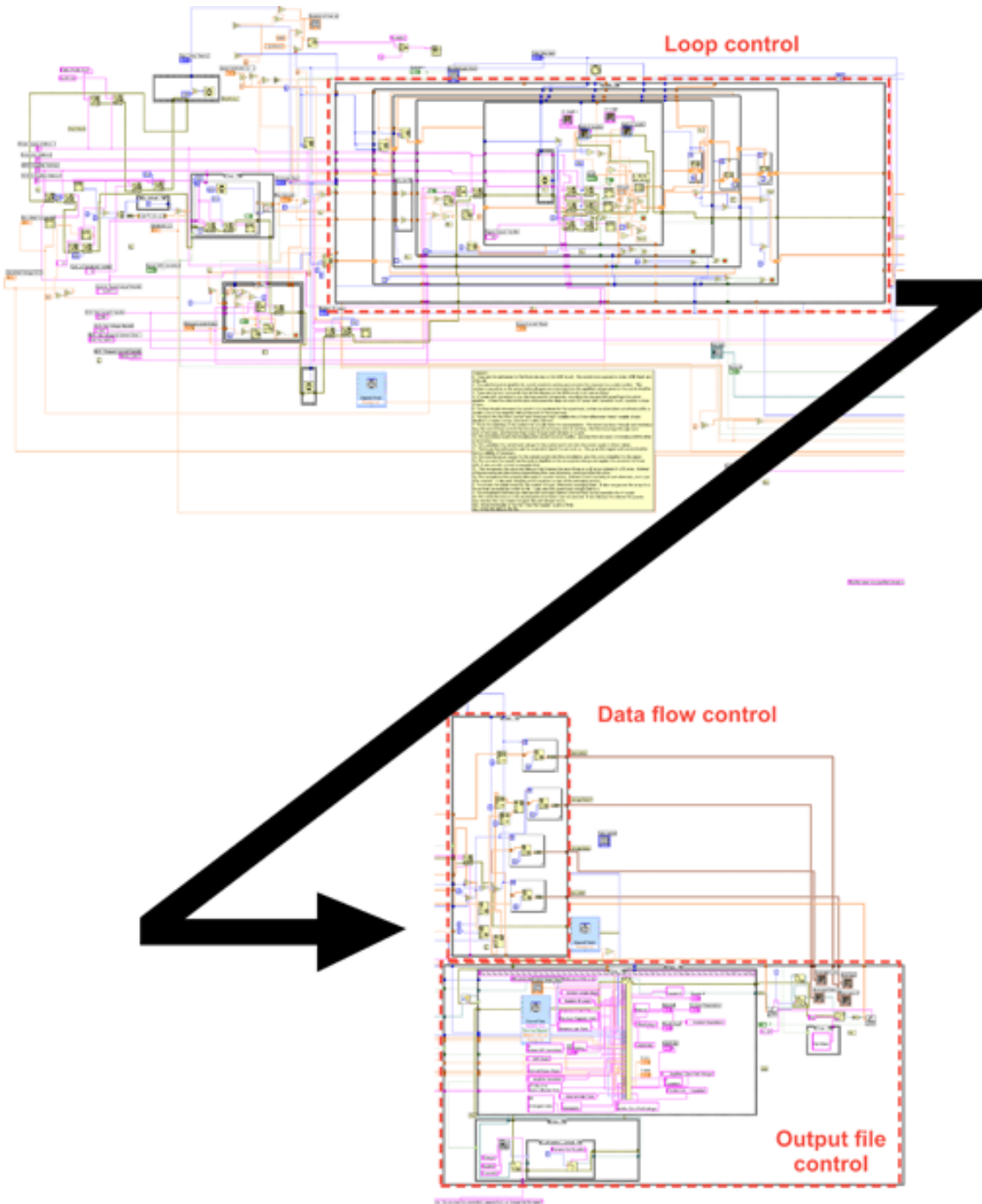


Figure 4.5: *The block diagram of the LabVIEW GUI. Each red box indicates sub-diagram: hysteresis sweep control, dataflow control and output file control diagrams.*

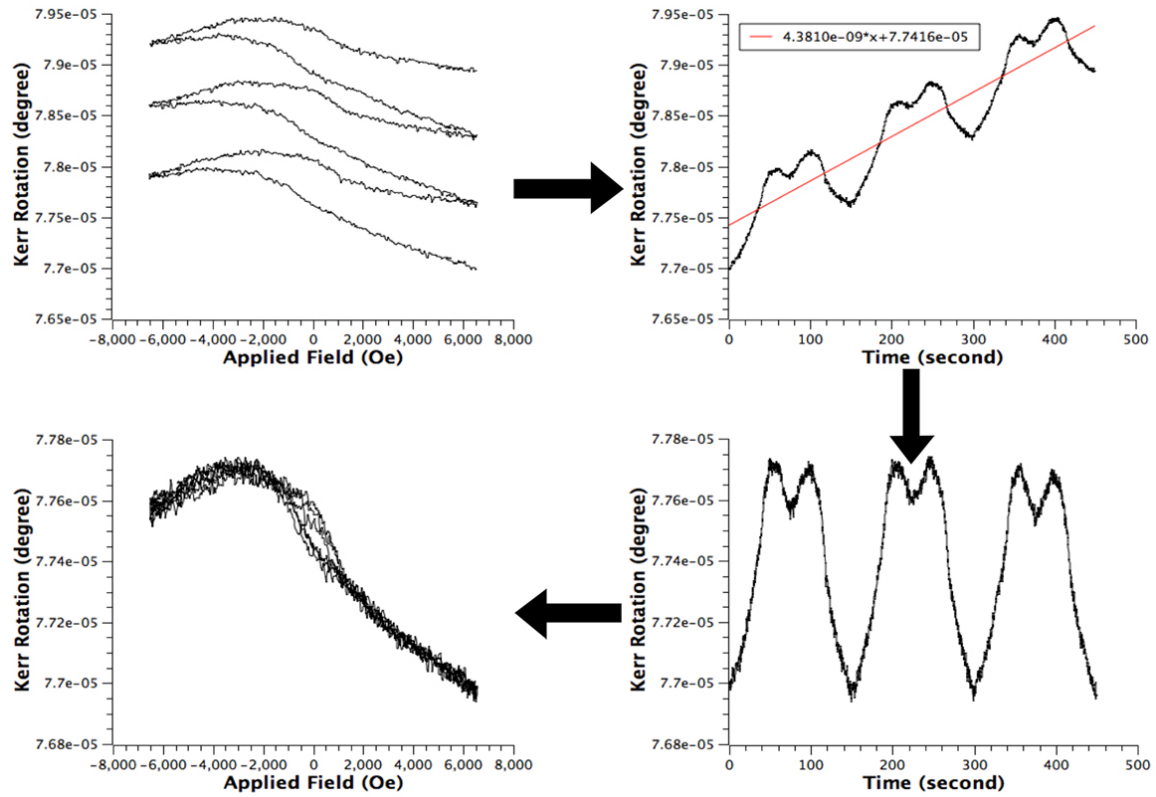


Figure 4.6: Processes of linear drift adjustment. (top-left) Raw data of Kerr signal vs. applied field hysteresis loops with linear drift. (top-right) Converting the plot to Kerr signal vs. time, and finding the slope value from linear fit. (bottom-right) The linear slope is adjusted. (bottom-left) Re-plotted Kerr signal vs. applied field hysteresis loops.

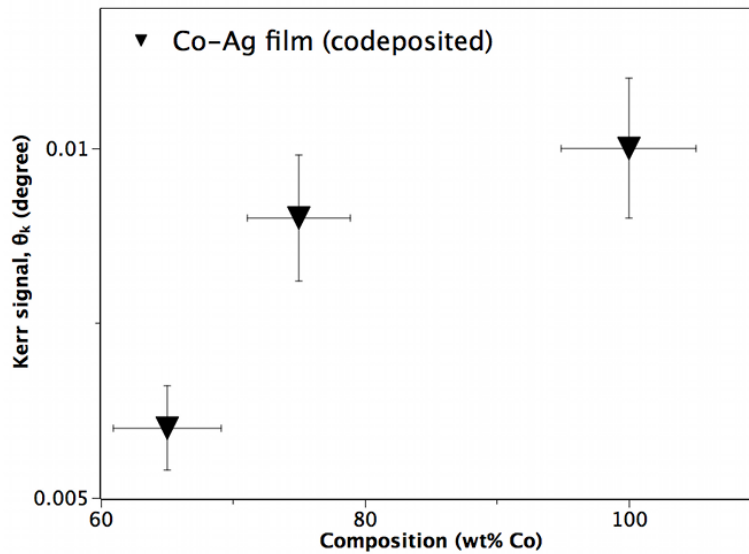


Figure 4.7: The measured Kerr signal of co-deposited Co-Ag films on SiO_2/Si with respect to Co weight percentage.

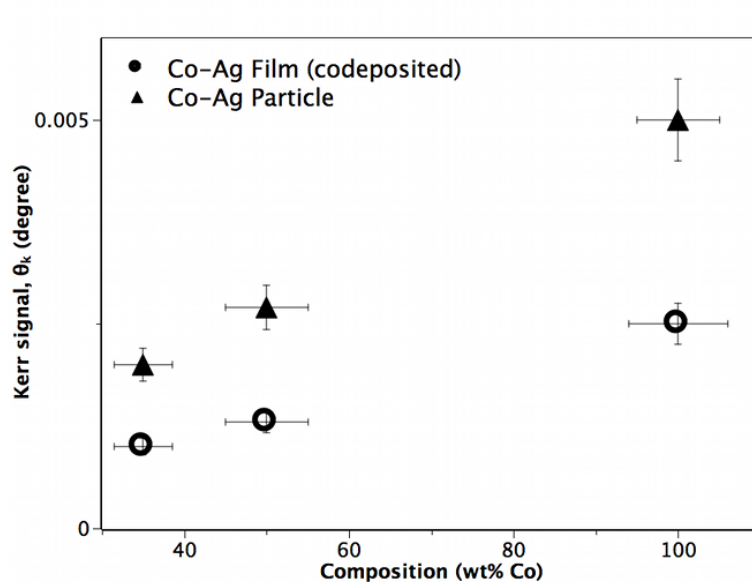


Figure 4.8: The measured Kerr signal of co-deposited Co-Ag films and nanoparticles as a function of Co weight percentage.

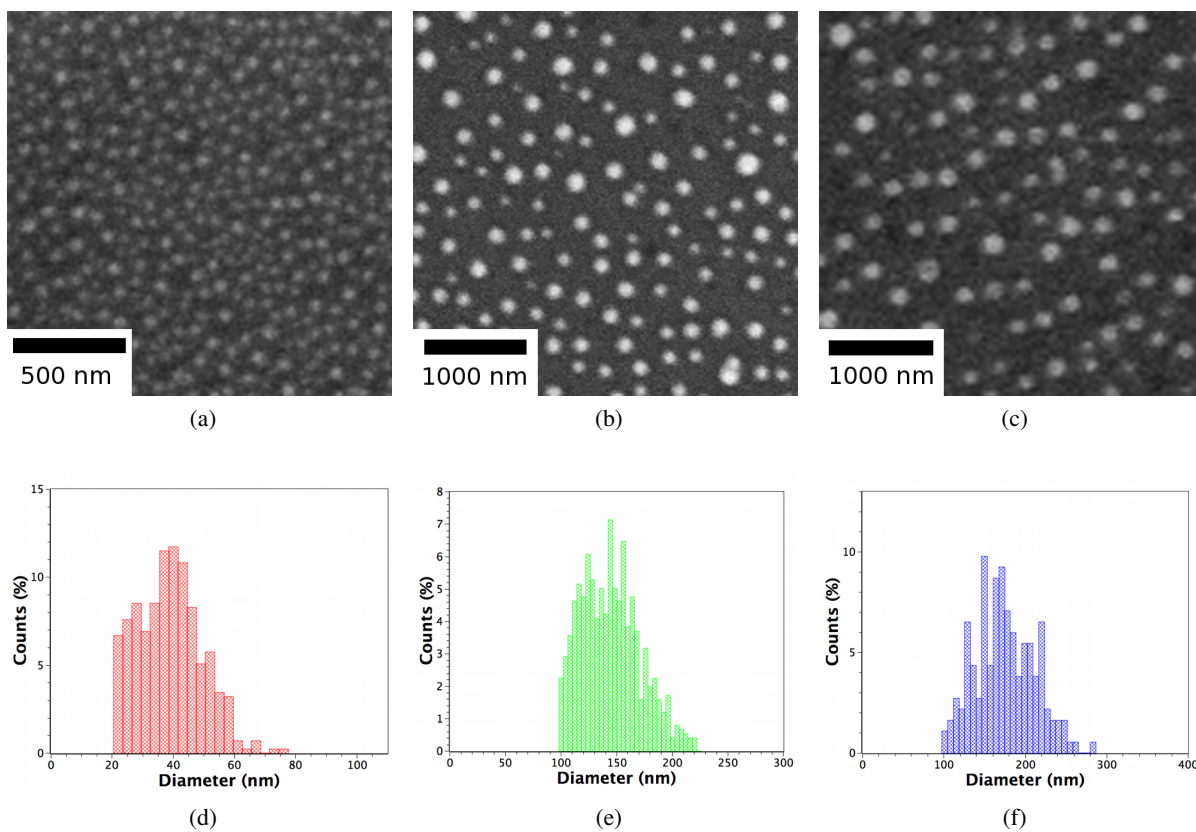


Figure 4.9: SEM micrograph of arrays of Co-Ag nanoparticles with different Co weight percentage: (a) 100 %, (b) 50 % and (c) 35 %. The corresponding size distribution of nanoarrays obtained: (d) [from image (a)], (e) [from (b)] and (f) [from (c)].

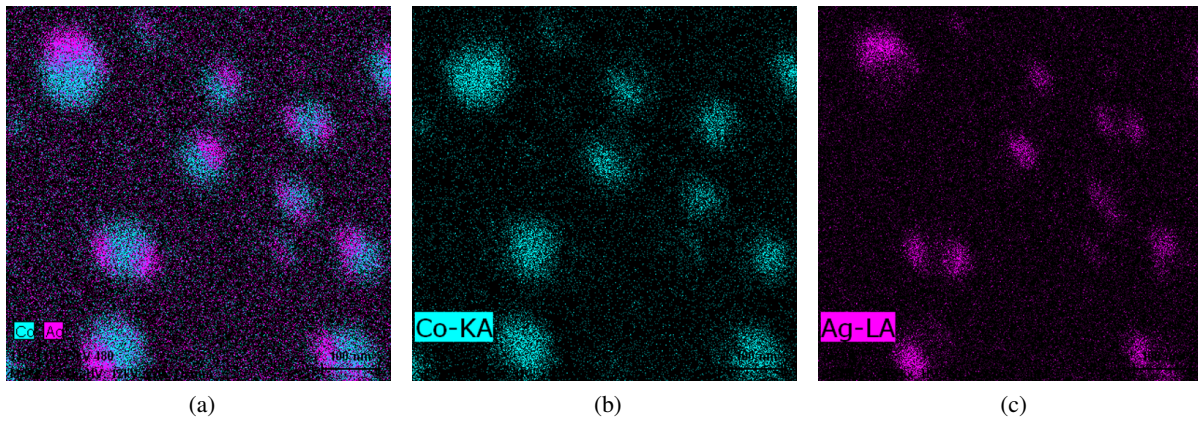


Figure 4.10: *Energy-dispersive X-ray mapping taken in SEM on the arrays of nanoparticles obtained from dewetting of co-deposited Co-Ag film. The image (a) is combined elemental maps of Co and Ag; (b) is the elemental maps of Co; (c) is the elemental maps of Ag. The size of images is 600 nm x 600 nm. The array of nanoparticles obtained from the thickness combinations of Co : Ag = 6 : 2 nm.*

Chapter 5

Magnetic properties of Co nanowires and nanoparticle arrays synthesized by pulsed laser melting

5.1 Summary

Nanosecond pulsed laser irradiation of thin films can induce formation of various nanostructures. Here, we have used the technique to fabricate nanostructures of ferromagnetic materials such as Co and Ni hemispherical nanoparticles and arrays of Co nanowires, nanorods and nanoparticles. In order to study the magnetic hysteresis behavior of the nanostructures, surface magneto-optic Kerr effect (SMOKE) characterization technique was utilized. While SMOKE has been applied in the past to investigate the magnetic information of continuous films, there is little work on applying it to characterize arrays of nanostructures with variable shape and size. First, arrays of magnetic nanoparticles of hemispherical shape and varying average size and size-dependent magnetic orientation was synthesized by the pulsed laser dewetting of Co and Ni material on SiO₂ substrates. SMOKE measurements were performed for a variety of different particle sizes and material. Systematic differences in saturation and coercivity were observed as a function of size and material. Next, periodic arrays of Co nanowires, nanorods and nanoparticles were fabricated by pulsed laser interference irradiation technique. In addition to SMOKE, magnetic force microscope (MFM) was used to investigate the magnetic domain properties. Magnetic domain orientation was found to depend on the in-plane aspect ratio of the nanostructure. We determined that the magnetic orientation was out-of-plane for shapes with aspect ratio ranging from 1 to 1.4 and transitioned to an in-plane orientation for aspect ratios greater than 1.4 (such as in nanorods and nanowires). Our results also showed that polycrystalline Co nanowires showed much higher coercivity and remanence as compared to bulk and thin film materials, as well as shapes with smaller aspect ratio. This result was attributed mainly to the shape anisotropy. These results demonstrated that nanosecond pulsed laser synthesis is capable of fabricating various nanostructures in a simple, robust and rapid manner and that SMOKE is a reliable technique to rapidly characterize the magnetic behavior of nanostructures.

5.2 Introduction

As discussed in Ch 1 (Sec. 2.2), when the size of magnetic material is reduced to length scales comparable with the magnetic domain wall or exchange force distance, the material starts exhibiting unusual magnetic behaviors. In addition to the size, other factors such as shape, crystalline state, and internal state of strain, influence magnetism, and hence their study is of continuing interest towards improving and advancing the science and technology of magnetic materials behavior. Specifically, the control of nanoscale magnetic anisotropy, which prompts the magnetization to point in desired directions, can be viewed as a fundamental requirement towards realizing functional nanomagnetic materials. This is because anisotropy determines properties such as superparamagnetism (the thermally activated switching of single-domain magnetization), the single-domain magnet size, and hard versus soft magnetic behavior. For instance, a magnetic nanowire with comparable width to the domain wall and micron size length presents large coercivity, large anisotropy and high remanence due to the shape and the magnetocrystalline anisotropy [172]. Similarly, arrays of hemispherical magnetic nanoparticles exhibit size dependent magnetization due to the large size dependent magnetostriction strain and the microstructure [5]. These properties in turn determine the choice of materials in a variety of applications, such as perpendicular or longitudinal high density magnetic storage [173], non-volatile and high speed magnetic memories (MRAM) [174, 175], opto-electronics [176] and biological applications [177, 178, 179, 180]. As has been well appreciated for many decades, magnetic anisotropy has contributions from magnetocrystallinity, shape, and magnetoelastic effects, which, either independently or through coupling with each other, determine the stable magnetic state.

In this study we have used surface magneto-optic Kerr effect (SMOKE) [89] and magnetic force microscopy (MFM) to characterize magnetic properties and anisotropy of ferromagnetic nanostructures. Arrays of hemispherical ferromagnetic nanoparticles and Co nanowires of various lengths were prepared by a nanosecond laser dewetting and interference techniques, respectively [43, 9, 5, 105]. SMOKE is a relatively straightforward characterization technique, and provides a reliable means of probing magnetic ultra thin films and nanostructures. SMOKE offers some important advantages suited for nanostructures, including its high sensitivity and the ability to locally probe the surface [89]. SMOKE is more sensitive than superconducting quantum interference devices (SQUID) magnetometry [165] for studying nanoscopic volume of magnetic materials. In addition, the experimental SMOKE setup is relatively simple and cost-effective and is therefore accessible to a wide variety of researchers. Essentially, SMOKE operates on the principle of a complex rotation of the plane of polarization of linearly polarized incident light upon reflection from the surface of magnetic material [79, 166]. The rotation is directly related to the magnetization of the material within the probing region of the light [79, 166]. We have used a home built SMOKE set-up to measure the magnetic behavior of arrays of Co and Ni nanostructures [As detailed in Ch 4]. The hysteresis loop was measured from the behavior of the Kerr signal vs. applied field (H), and was measured for the polar and longitudinal geometries to provide average magnetization direction of the probed area of the array.

The magnetic behavior study of various Co nanostructures, including thin films, and periodic arrays of wires, rods and particles, showed large dependence on the type (i.e. shape) of nanostructure. For instance, magnetization reversal measurements by SMOKE for Co arrays of nanowires with different average nanowire lengths showed that coercivity and remanence fields depend on aspect ratio of nanowires. MFM

studies revealed that the magnetic domains are oriented along the wire direction, and the SMOKE analysis indicated a large coercivity and high remanence when the external field was applied parallel to the wire. Over all, these results demonstrated that SMOKE is a reliable technique to rapidly characterize the magnetic behavior of nanostructures. Besides, the pulsed laser synthesis is able to fabricate various nanostructures in a robust and cost-effective manner.

5.3 Experimental Details

5.3.1 Synthesis of nanoparticle arrays by nanosecond pulsed laser dewetting

Nanosecond pulsed laser irradiation of ultrathin metal films on dewetting substrates, such as SiO₂, result in self-organized patterns, ultimately leading to an array of nanoparticles with well defined size and inter-particle spacing and a polycrystalline nanostructure [104, 43]. In the case of ferromagnets like Co and Fe, we have previously seen by MFM measurements that the particles are hemispherical in shape and are single domain in the size range of 40 to 200 nm [181, 5]. In the experimental approach, ultrathin films of the metal, typically between 1 to 10 nm in thickness, are deposited by electron beam or pulsed laser deposition in high vacuum conditions onto commercially obtained, optical quality, SiO₂/Si wafers consisting of 400 nm thick thermally grown oxide layer on polished Si(100) wafers [112, 5]. Following the deposition, the films are irradiated in vacuum with approximately 10,000 pulses from a 266 nm ultraviolet laser having a pulse length τ_p of 9 ns at energies sufficient to melt the metal film. For this irradiation condition, the heating and cooling rate of the metal film is of the order of 10^{10} K/s. As a result of this rapid cooling, the metal nanoparticles are quenched in and retain some residual in-plane biaxial strain due to the thermal expansion mismatch between the metal and underlying SiO₂ substrate. Consequently, as was quantitatively shown earlier [5, 113], the magnetization direction of single domain particles show a variety of orientations ranging from in-plane for small particles (40 to 75 nm for Co) and out-of-plane for larger particles (75 to 150 nm for Co). While magnetic energy based on shape anisotropy arguments would predict in-plane orientation for hemispherical particles, out-of-plane orientation was also observed. This was attributed to large magnetostrictive contribution due to the residual in-plane strains, which could explain the out-of-plane orientation. Furthermore, the size-dependence was attributed to a size-dependent nanostructure of the particle, i.e. smaller particles had smaller grains. A competition among the various magnetic anisotropy energies (magnetocrystalline, shape, and magnetostrictive), which is dependent on the grain size and number of grains in the nanoparticles, resulted in an effective in-plane anisotropy direction for the smaller particles and out-of-plane orientation for the larger particles. Here, we have investigated arrays of Co and Ni prepared by the above approach through the SMOKE technique. For the case of Co, arrays with average particle diameters of 43 ± 31 nm (labelled NP1) and 66 ± 25 nm (labelled NP2) have been investigated by SMOKE. Ni arrays with average particle diameter of 70 ± 24 nm (labelled NP3) was also investigated.

The morphology was characterized by scanning electron microscopy (SEM) in a Hitachi S4300N, and by atomic force microscopy (AFM) in a Nanonics MultiView 1000. The magnetic properties were characterized by physical properties measurement system (PPMS) and Surface Magneto-optic Kerr effect (SMOKE). The details of the MFM and PPMS measurements have been published elsewhere [5].

5.3.2 Synthesis of 1-D nanowire arrays by two beam interference irradiation

Two beam interference irradiation on nanometer thick metal films induces sine-wave like thermal profile across the film plane [9, 123]. This leads to extrinsically induced thermocapillary flow and eventually to a pattern of periodic nanowires. Further laser irradiation of the nanowires ultimately leads to break up into nanoparticles with well defined interparticle spacing due to the Rayleigh instability [9]. In the experiment, 6 nm thick Co films (labelled TF) were deposited on commercially available and optically smooth 400 nm SiO₂ on Si(100) wafers by using the electron-beam evaporation technique under ultra-high vacuum (UHV) conditions. The substrates were ultrasonically cleaned with acetone and isopropanol before deposition. The film was deposited through a periodic array of contact masks made with nylon with square openings of 280 μm by 280 μm size and spaced at a distance of 400 μm . By this step, a patterned surface comprising of a large of number of film islands were created. The film thickness was calibrated by performing step-height measurements with atomic force microscopy (AFM). Following the deposition, two beam laser interference irradiation was performed under ambient conditions. The irradiation was performed with 266 nm ultraviolet (UV) laser having a 9 ns pulse and laser energy density sufficient to melt the Co film. A single laser beam was split into two equal energy density beams using a 50-50 beam splitter and was incident on the film at an inclusive angle of 45.7° in a plane perpendicular to the substrate plane. The resulting theoretical interference spacing for this geometry was 343 nm. As shown from our previous study of the nanostructures formation as a function of the number of laser pulses n , the film starts rupturing with spatially periodic structures at length scales comparable to the interference spacing. Longer irradiation yields the formation of a periodic array of nanowires. Continued irradiation results in the break-up of these nanowires into a mixture of nanoparticles and nanorods, and then into a spatially ordered arrangement of nanoparticles in the final stage [9, 123]. Here, the number of laser pulses was varied between $25 < n < 150$ to create arrays of nanowires, nanorods, and nanoparticles. This process can be explained on the basis of the various mechanisms of fluid motion. When irradiating the metal film with a two-beam interference pattern, the resulting periodic laser intensity induces a transient and periodic sinusoidal-like thermal gradient along the plane of the film which creates a surface tension gradient. Consequently, thermocapillary (Marangoni) convection of the molten Co resulting in the formation of long, cylindrical-like, nanowires. Further irradiation causes the Rayleigh instability, in which cylinders are unstable to certain wavelengths, and the nanowires break up into nanoparticles [9].

The various nanostructure morphologies were characterized by scanning electron microscopy (SEM) in a Hitachi S4300N and a Zeiss Merlin, and by atomic force microscopy (AFM) in a Asylum MFP-3D. The magnetic switching behavior of the nanostructure arrays were characterized by SMOKE system, and the magnetic domain orientation with respect to the substrate was determined from the bright and dark contrast of the magnetic force microscopy (MFM) in a Asylum MFP-3D.

5.3.2.1 SMOKE measurements

Surface magneto-optic Kerr effect (SMOKE) technique was employed to analyze the magnetic anisotropy of the various Co nanostructure arrays [89]. A monochromatic 635 nm diode laser light passed through a glan-thompson polarizer, an aperture and finally, an objective lens to decrease the beam size to approximately 80 μm . The incident angles, θ_i , for polar and longitudinal geometries were $\theta_i = 72.4^\circ$ and 17.6° ,

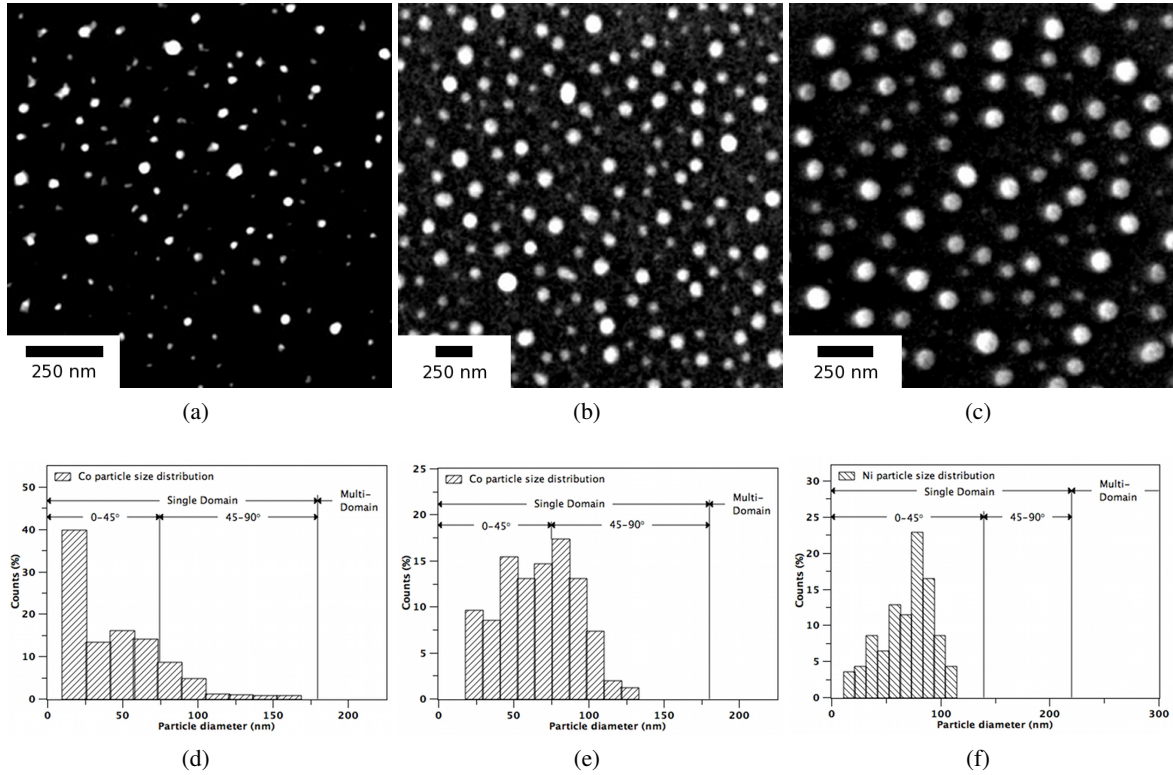


Figure 5.1: (a), (b), and (c) SEM images of Co arrays S1, Co array S2 and Ni array S3, respectively. (d), (e), and (f) The particle size distribution of corresponding to S1, S2, and S3 respectively. The average particle size D_{avg} estimated from the histograms are 53 nm (S1), 71 nm (S2) and 74 nm (S3).

respectively [Fig. 4.2(a) & (b) (subsec. 4.3.2)]. For arrays of hemispherical Co and Ni nanoparticles (NP1, NP2 and NP3), the laser spot size was appropriate to cover an array of the nanoparticles. SMOKE measurements were performed on the samples in two different geometries, polar and longitudinal. For arrays of nanowires, similarly, SMOKE measurements were performed in polar and longitudinal geometries. In the longitudinal geometry, the external magnetic field was applied parallel and perpendicular to the wire direction in order to determine preferential magnetization direction. Details of the technique have been detailed elsewhere [164, 89].

5.4 Results

5.4.1 SEM, AFM and MFM

The SEM images of arrays of hemispherical small diameter Co (NP1, 43 ± 31 nm), large diameter Co (NP2, 66 ± 25 nm) and Ni (NP3, 70 ± 24 nm) nanoparticles are shown in Fig. 5.1. This and similar SEM images were used to analyze the size distribution of the particles in the array. The histograms on the right side of each SEM image represent the particle size distribution with the average particle size D_{avg} of 43, 66 and 70 nm in diameter, respectively for the three samples. Krishna et al. revealed using MFM measurements that Co nanomagnets are single domain and have in-plane magnetization till 75 nm and then out-of-plane up

to 180 nm in diameter [5]. Similarly the Ni nanomagnets are single domain and have in-plane magnetization till 140 nm and out-of-plane up to 220 nm in diameter. Beyond those sizes, the particles are multi-domain in nature.

The SEM images of 6 nm thick Co film (TF), arrays of Co nanowires, nanorods/nanoparticles (labelled NRNP), and ordered nanoparticles (labelled ONP) are shown in Figs. 5.2(a)-(e). The Co film was irradiated by the number of laser pulses n to fabricate nanowires ($n = 5$ to 25), NRNP ($n = 25$ to 150) and ONP ($n < 150$). Two different types of nanowires are shown in Figs. 5.2(b) and (c). One has two thinner parallel wires with a groove connecting both wires, which was named “grooved-wire” (labelled GW) [Fig. 5.2(b)] while the other one, was named “single-wire” (labelled SW) [Fig. 5.2(c)]. Thermocapillary convection generates flow of the melted Co towards each interference minima, hence GW structure appears prior to the final formation of the SW at the minima.

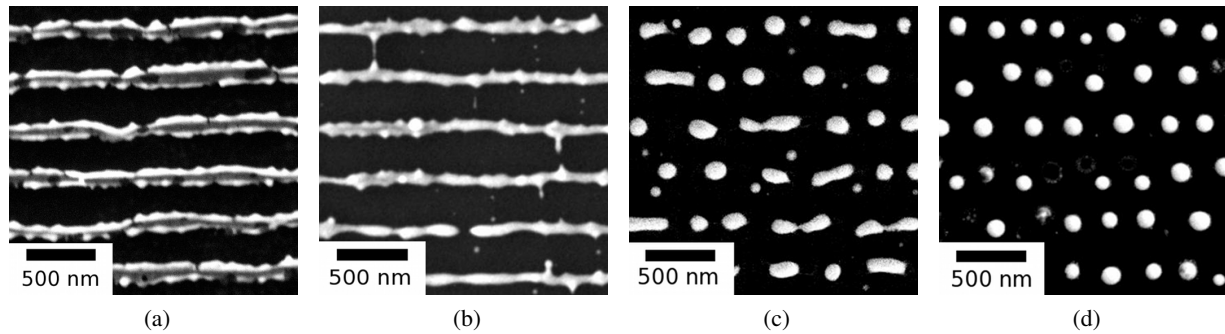


Figure 5.2: SEM images of Co arrays of (a) grooved-wire, (b) single-wire, (c) rods/particles and (d) particles, respectively. (Co rich and SiO₂ rich regions correspond to bright and dark contrasts)

For Co nanowires (GW & SW), nanorods/nanoparticles (NRNP), and ordered nanoparticles (ONP), the SEM images were used to analyze the shape and size distribution of the nanostructures in each array. In Figs. 5.3(a) and (b), each histogram represents the size distribution of single-wire, nanorods and nanoparticles width and length. From Fig. 5.3(a), the average width of the single-wire and nanorod are similar size, only [~9 % difference, however the average width (= diameter) of nanoparticles is ~29 % larger than other two. From Fig. 5.3(b), the average length of the single-wire is 78 % and 92 % larger than the nanorod and nanoparticle, respectively. The arrays of both nanowires had an average spacing of 377 ± 27 nm. The array of the single-wire and grooved-wire had 92 ± 6 nm and 35 ± 5 nm (width of thin elongated part but not width of the groove) average width, respectively. From Fig. 5.2(d), the average spacing of ordered nanostructures along perpendicular to the nanowire direction was measured to be 369 ± 23 nm. Also, the average length and width of nanorods was estimated to be 351 nm and 82 ± 8 nm, while the average diameter of the particles was estimated to be 132 ± 24 nm, respectively. From Fig. 5.2(e), the array of ordered nanoparticles (ONP) had an average diameter of 130 ± 21 nm.

The AFM height profile of Co nanostructures are shown in Figs. 5.4(a) - (d). From the AFM image contrast in Fig. 5.4(a), the groove-like morphology at the center of the each wire can be observed, however due to the comparable tip size ($R = 50$ nm) to the groove width and depth, 50 and 60 nm, the AFM image could not resolve the groove height profile clearly. Additionally, the MFM domain image of Co nanowires

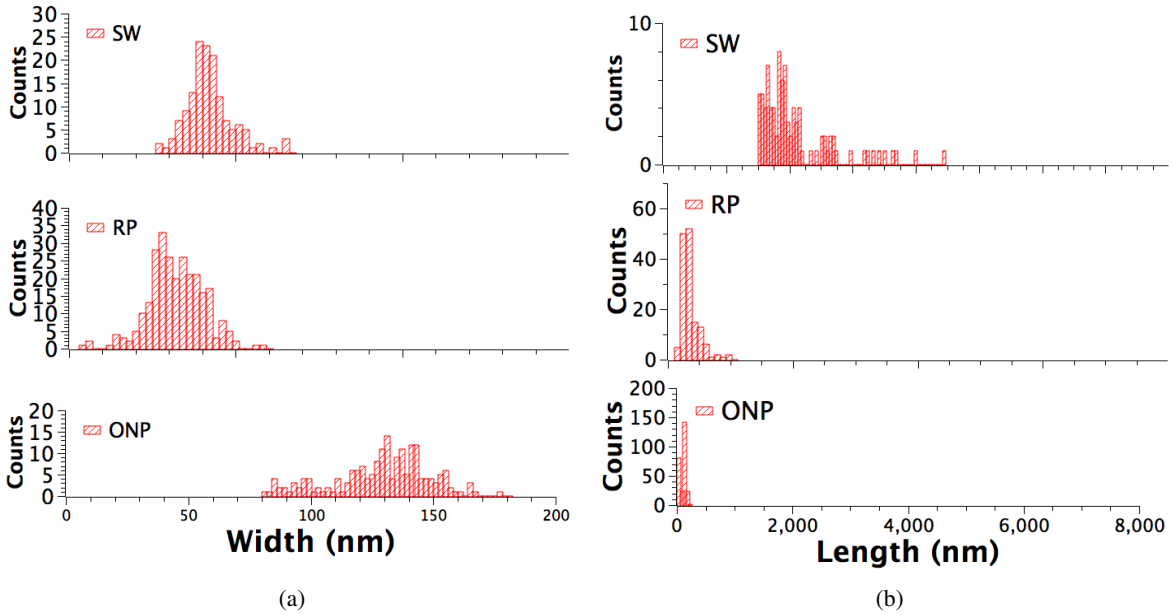


Figure 5.3: The nanostructure size distribution of (a) width and (b) length of Co single-wire, nanorod and nanoparticle arrays. The average width and length of wires and rods and diameter of particles estimated from the histograms are $W = 92$, $L = 1600$ nm (single-wire), $W = 82$ nm, $L = 357$ nm (rods) and $D = 132$ nm (particles), respectively.

and nanoparticles are shown in Figs. 5.4. The domain structures of the single-wire indicates the parallel domain orientations along the wire direction, which is not consistent with the results of Henry et al. [6]. On the other hand, from Fig. 5.4(d), Co nanoparticles have out-of-plane magnetization and independent from the ordered direction.

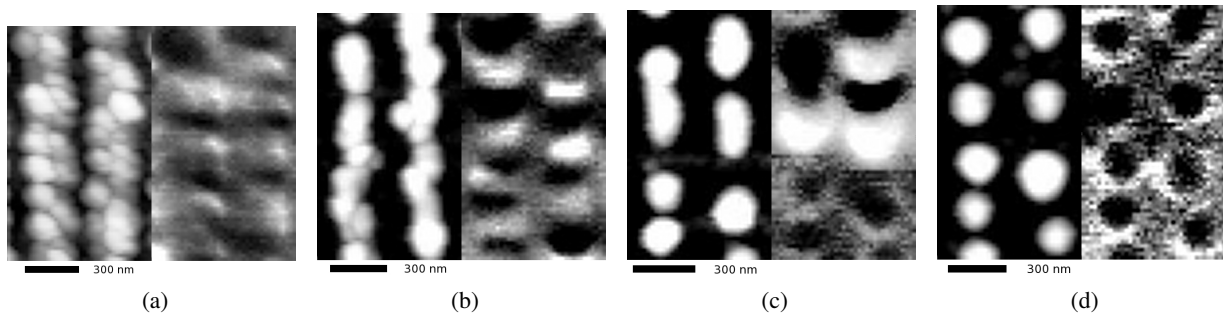


Figure 5.4: AFM (left) and MFM (right) images of Co (a) grooved-wire, (b) single-wire, (c) rods/particles and (d) particles arrays, respectively.

5.4.2 SMOKE

The primary goal of our SMOKE measurements was to confirm the large area magnetic anisotropy behavior of each of the three arrays. From SMOKE, the Kerr signal vs magnetic field H hysteresis loop can be generated, which in turn provides the average saturation field H_S and coercivity H_C of the arrays over the region probed by the optical beam. When this measurement is done in the polar and longitudinal geometries, it is possible to differentiate between ease of domain rotation along the out-of-plane direction versus in-plane orientations. In other words, when the array has smaller magnetic saturation field in polar geometry versus longitudinal, it would indicate easier out-of-plane magnetization axis. Similarly, an easier in-plane axis would result if the smaller saturation field was found for the longitudinal geometry. In fact, when SMOKE measurements are done as a function of angle, the exact orientation of the magnetic axis could, in principle, be determined.

5.4.2.1 Co and Ni nanoparticles (NP1, NP2 and NP3)

Fig. 5.5(a) shows a Kerr signal vs H hysteresis loop of Co array NP1 for two different SMOKE geometries. The solid lines represent the data for polar geometry, and the dashed lines for longitudinal geometry. The overall characteristics of the SMOKE hysteresis loops indicates the array of particles in NP1 has predominantly in-plane magnetization properties, consistent with the average particle size of the array of 53 nm. H_S values in polar and longitudinal geometries are 3870 and 920 G, and their relative difference is 76 %. This area averaged behavior is consistent with previous MFM results, which showed that for Co, particles with diameter < 75 nm shown preferential in-plane orientation.

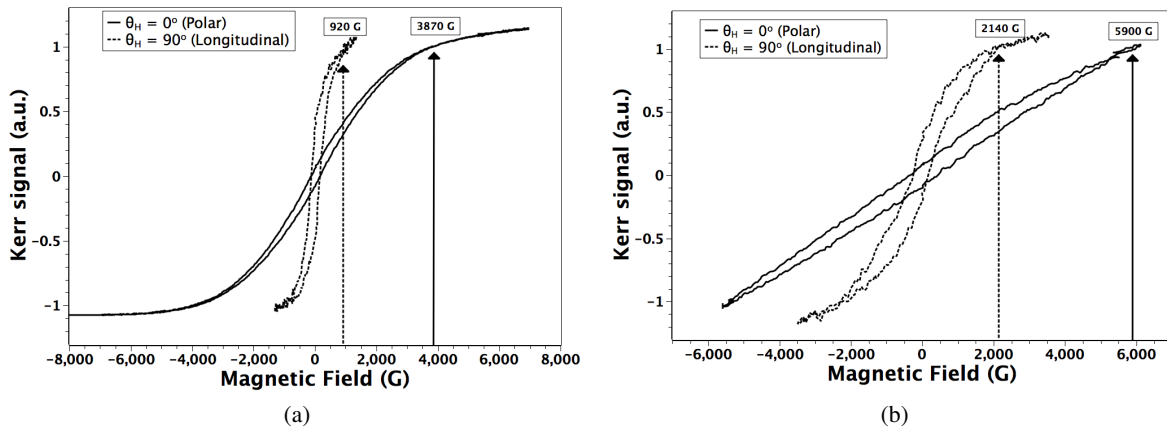


Figure 5.5: Kerr signal - H hysteresis loops for arrays of Co hemispherical nanoparticles on SiO₂ (sample S1). The solid lines represent the data for polar geometry and the dashed lines for longitudinal geometry. The average diameter of the particle was 53 nm in diameter. (b) Hysteresis loop for arrays of Co hemispherical nanoparticles on SiO₂ (sample S2). The solid lines represent the data for polar geometry and the dashed lines for longitudinal geometry. The average diameter of the particle was 71 nm in diameter.

Next, Co array NP2, with larger average particle diameter of 71 nm was studied. Fig. 5.5(b) shows a Kerr signal vs H hysteresis loop of sample NP2 in two different geometries. H_S values in polar and longitudinal geometries are 5900 and 2140 G, and their relative difference is 64%. This hysteresis curves behavior

indicates that the sample NP2 has an in-plane magnetic shape anisotropy with the easy magnetization axis in-plane direction. Coercivity field H_C in polar and longitudinal are 385 and 200 G, and their relative difference is 48 %. This result is also consistent with previous MFM results which indicate that particles with average diameter < 75 nm should be preferentially in-plane. Also, we compared the difference in saturation fields for the two Co arrays having different average particle sizes. Fig. 5.6 compares the hysteresis for the two Co arrays. The smaller size array, NP1 has smaller in-plane saturation field then NP2, as seen in the longitudinal measurement [Fig. 5.6(b)]. This supports the previous MFM observations that as size increases, the magnetization tends to rotate towards the out-of-plane direction [5]. In addition, from figure 5.6 one can see that the coercivity and saturation field is larger for NP2 than NP1 in both orientations. It indicates that for S1, almost all particles are oriented in-plane, whereas for S2, some particles (presumably smaller) have easy axis in-plane, while the others (bigger) have out-of-plane orientation. The SMOKE signal for S2 is a mixture of both components, while for S1 it is dominated by one component only.

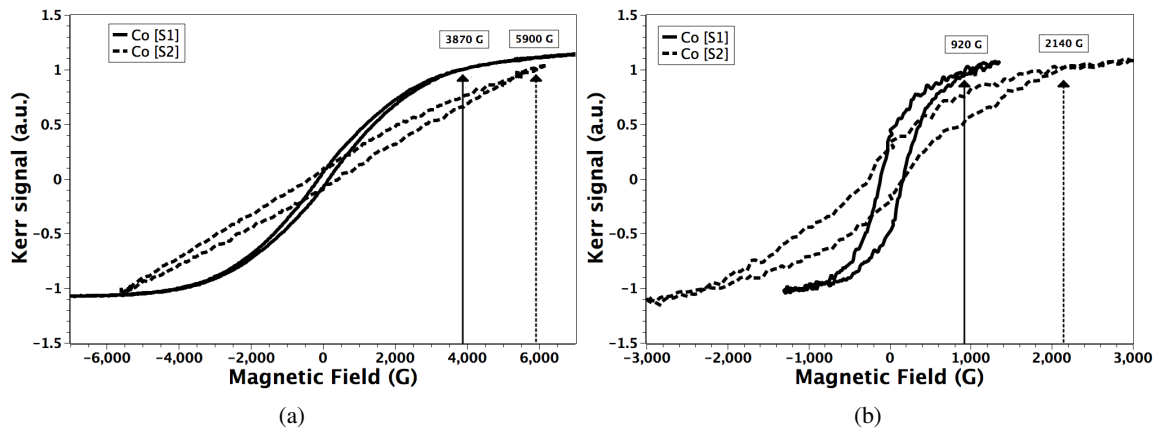


Figure 5.6: Hysteresis loops for the arrays of Co particles (sample S1 and S2) in (a) polar and (b) longitudinal geometries. The solid lines represent the data for S1 and the dashed lines for S2.

Lastly, we studied the magnetic behavior of Ni (NP3) arrays with similar average particle diameter as the Co (NP2) array. The Kerr signal hysteresis loops of sample NP3 in two different geometries are shown in Fig. 5.7(a). From these measurements, the array shows lower saturation field for the in-plane orientation measurement suggesting that the easy-axis of magnetization lies preferentially along the in-plane direction. Again, this is consistent with MFM observations. The H_S values in polar and longitudinal geometries are 2870 and 1160 G, and their relative difference is 60 %. Coercivity field H_C in polar and longitudinal are 190 and 360 G, and their relative difference is 47 %. In Fig. 5.7(b) and (c), Kerr signal vs H hysteresis loops of sample NP2 (Co, 71 nm) and NP3 (Ni, 74 nm) for the two θ_H values are presented. This comparison revealed the dependence of hard and soft ferromagnetic materials on magnetization properties of nanoparticles. The presence of the easy magnetization axis along the in-plane direction in both arrays, NP2 and NP3 is evident. However, quantitatively, H_S and H_C values of two samples in each geometry are different due to the intrinsic material property difference. By comparing relative difference of H_S at polar and longitudinal geometries between sample NP2 and NP3, we get 64 and 60 % respectively. NP2 gives larger relative difference

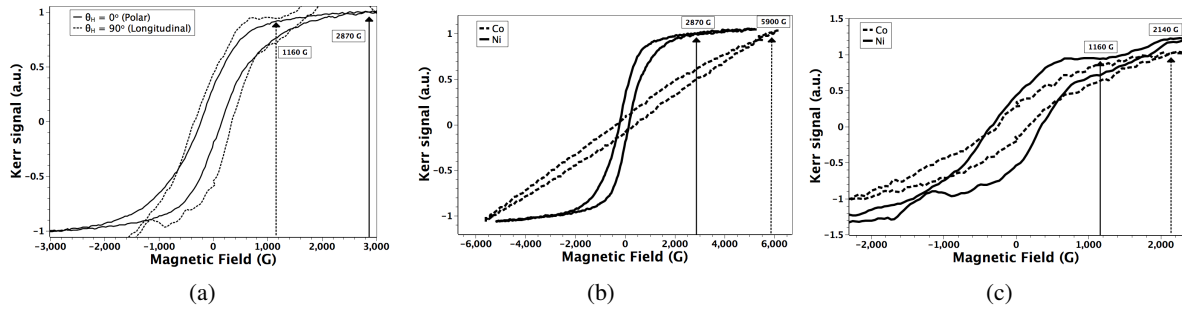


Figure 5.7: (a) Hysteresis loop for arrays of Ni hemispherical nanoparticles on SiO₂ (sample S3). The solid lines represent the data for polar geometry and the dashed lines for longitudinal geometry. The average diameter of the particle was 74 nm in diameter. (b) Comparison of hysteresis loops for the arrays of Co and Ni particles (sample S2 and S3) in polar and (c) longitudinal geometries. The dashed line represents S2 and the solid line represents the data for S3. The arrows mark the saturation points on the hysteresis curves.

compared to NP3 likely due to hard and soft ferromagnet property difference. The cobalt array NP2 quite evidently, is harder to switch than the Ni array NP3, which is consistent with Ni being softer than Co.

5.4.2.2 Co nanostructures (TF, SW, NRNP, ONP and GW)

Magnetic anisotropy behavior of Co nanostructure arrays was also measured by SMOKE to obtain the average saturation field H_S and coercivity H_C of the arrays over the region probed by the optical beam. The focused laser beam has approximately 60 μm spot size, therefore SMOKE probed around 200 nanowires at once. By comparing results from the two different orientations of nanostructures with respect to the external magnetic field direction in the longitudinal geometry, information of preferential magnetization direction and domain orientation was also obtained.

Fig. 5.8(a) shows a Kerr signal - H hysteresis loops of Co grooved-wire (GW) [Fig. 5.2(a)] array for two different SMOKE geometries. The red lines represent the data for the parallel magnetic field with respect to the wire direction in the longitudinal geometry (L^{\parallel}) and the blue lines for the field perpendicular to the wires in the longitudinal geometry (L^{\perp}). The overall characteristics of the SMOKE hysteresis loops indicates the array of GW has predominantly parallel magnetization to the wire direction, which is consistent with domain orientations from MFM image. Coercivity fields in the L^{\parallel} and L^{\perp} geometries are $H_c^{\parallel} = 1000$ Oe and $H_c^{\perp} = 432$ Oe, and saturation fields are $H_s^{\parallel} = 2.1$ and $H_s^{\perp} = 2.2$ kOe, respectively. The larger coercivity and the lower saturation when the field is applied \parallel to the nanowire compared to \perp case indicates Co GW has a preferential magnetic orientation along the wire axis. This magnetic behavior is consistent with previous studies [6, 71, 182].

Fig. 5.8(b) shows hysteresis loop of ordered Co particles array [Fig. 5.2(d)] for three different geometries. The inset plot shows the hysteresis loops of the L^{\parallel} , L^{\perp} and polar geometries. Coercivity values in the L^{\parallel} and L^{\perp} are negligible, and saturation fields are $H_s^{\parallel} = 4.2$ kOe and $H_s^{\perp} = 4.1$ kOe, respectively. Almost identical hysteresis loops in the L^{\parallel} and L^{\perp} geometries suggest that *the nanoparticle array no longer has the*

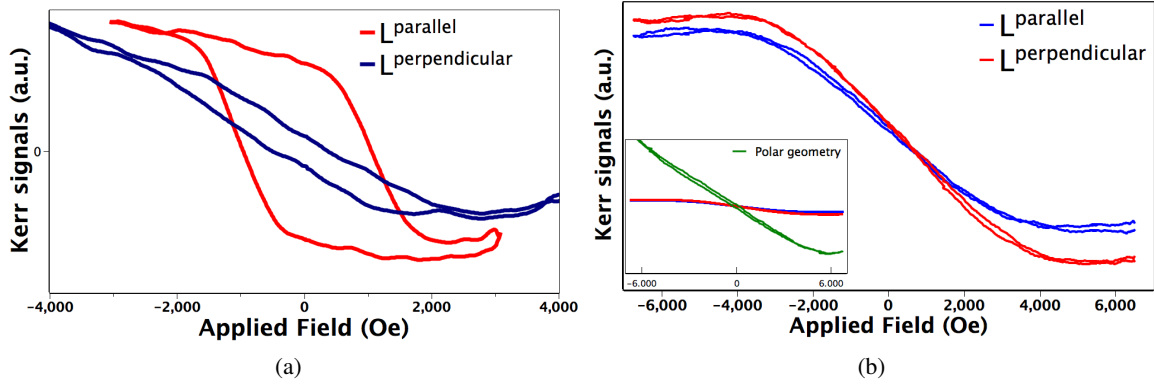


Figure 5.8: *Hysteresis loops for the arrays of Co (a) nanowire and (b) particles. (a) Comparison between hysteresis loops for the nanowire array in the L^{\parallel} and L^{\perp} geometries. (b) Comparison between hysteresis loops for the particle array in the L^{\parallel} and L^{\perp} geometries.*

shape anisotropy along the sample plane due to the hemispherical shapes. Also the Kerr signals are stronger in the polar geometry compared to the longitudinal one.

Fig. 5.9(a) shows hysteresis loops of each nanostructure array including the grooved-wire, single-wire and rods/particles in the L^{\parallel} geometry. The hysteresis indicates that the coercivity value decreases when going from wires to rods, or as the aspect ratio decreases. The inset plot shows the hysteresis loops of the nanostructures including the particles. The grooved-wire ($H_c^{\parallel} = 1000$ Oe), which has different shape and geometry with the single-wire has higher coercivity than the single-wire ($H_c^{\parallel} = 670$ Oe). Also, the single-wire, which has the larger aspect ratio than the rod ($H_c^{\parallel} = 340$ Oe) has higher coercivity. From the inset plot, the hysteresis indicates that the relative Kerr signal value among different nanostructures is not different in the longitudinal geometry. Fig. 5.9(b) shows the hysteresis loops of the grooved-wire, rods/particles and particles arrays in the polar geometry. The hysteresis indicates that the Kerr signal value increases when the morphology changes from wires to particles.

5.5 Discussion

5.5.1 Co and Ni nanoparticle arrays

The primary goal of this portion of the study was to further investigate the magnetic anisotropy behavior of arrays of Co and Ni nanoparticles prepared by pulsed laser synthesis using the SMOKE technique. Previous measurements by our group primarily focused on the use of MFM to ascertain the size-dependent anisotropy of hemispherical shaped particles ranging in size from 20 to 200 nm [181, 5, 113]. Those results clearly showed that particles which were single domain had a size-dependent magnetization direction. In the case of Co, the particles had in-plane orientation up to 75 nm diameter, and then were preferentially out-of-plane above that. Here, for the first time, the SMOKE technique was used to investigate this anisotropy. We confirmed for the case of Co nanoparticles (NP1 and NP2), with average diameters of 43 and 66 nm respectively, that the area averaged behavior was consistent with MFM results in that the particles with diameter < 75 nm shown preferential in-plane orientation. Also, the array NP1, had a larger saturation field

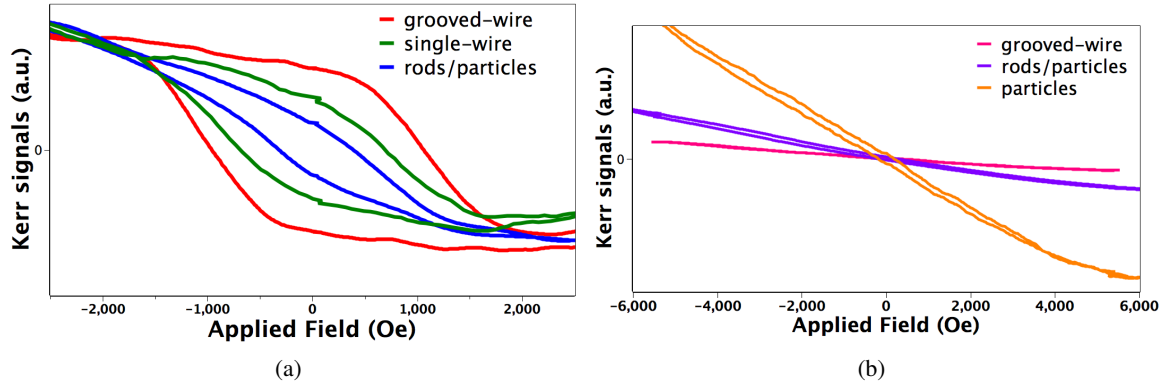


Figure 5.9: Hysteresis loops for the arrays of Co nanowires (single- and grooved-wire), rods/particles and particles. (a) Comparison between hysteresis loops for the four different nanostructure arrays in the L^{\parallel} geometry. (b) Comparison between hysteresis loops for grooved-wire, rods/particles and particles arrays in the polar geometry. In both (a) and (b), the red lines represent the data for grooved-wire, the green lines for single-wire, the blue lines for rods/particles and the violet lines for only particles.

in the out-of-plane or polar direction then the larger array NP2 [Fig. 5.6(a)]. Likewise, NP1 had smaller in-plane saturation field than NP2, as seen in the longitudinal measurement [Fig. 5.6(b)]. This observation also supported the previous MFM observations that as size increases, the magnetization tended to rotate towards the out-of-plane direction [5]. The comparison of the behavior of Co (NP2) and a similarly sized Ni array (NP3) revealed the dependence of hard and soft ferromagnetic materials on magnetization properties of the nanoparticles. The presence of the easy magnetization axis along the in-plane direction in both array NP2 and NP3 was evident. However, quantitatively, H_S and H_C values of two samples in each geometry were different due to the intrinsic material property difference. As would be predicted, the Co array was harder to switch than the Ni array, consistent with Ni being softer than Co.

5.5.2 Dependence of magnetic domain properties on aspect ratio

The relation between the in-plane aspect ratio (AR) value and the magnetic domain property of each nanostructure was studied. The in-plane AR is defined as the ratio of the width of a nanostructure to its length. From AFM and MFM image, the AR of a nanostructure and corresponding magnetic domain and magnetization orientation can be obtained. In Fig. 5.10, the histogram represents the AR distribution of nanostructures with its magnetic domain and magnetization orientation. First, the histogram indicates that the single domain and multi-domain nanostructure exists in the range of $1 < AR < 3$ and $AR \geq 3$, respectively. Secondly, the histogram shows the locations of out-of-plane and in-plane magnetizations. The single domain and out-of-plane (OP) magnetization is in the range of $1 < AR < 1.4$, the single-domain with in-plane magnetization is observed for $1.4 \leq AR < 3$, while the multi-domain in-plane magnetization exists for $AR \geq 3$.

5.5.3 The chain of spheres model

In order to understand the relation between coercivity values and average length of the nanostructure, we employed the chain of spheres model developed by Jacobs and Bean [16, 70]. In the model, it is assumed that

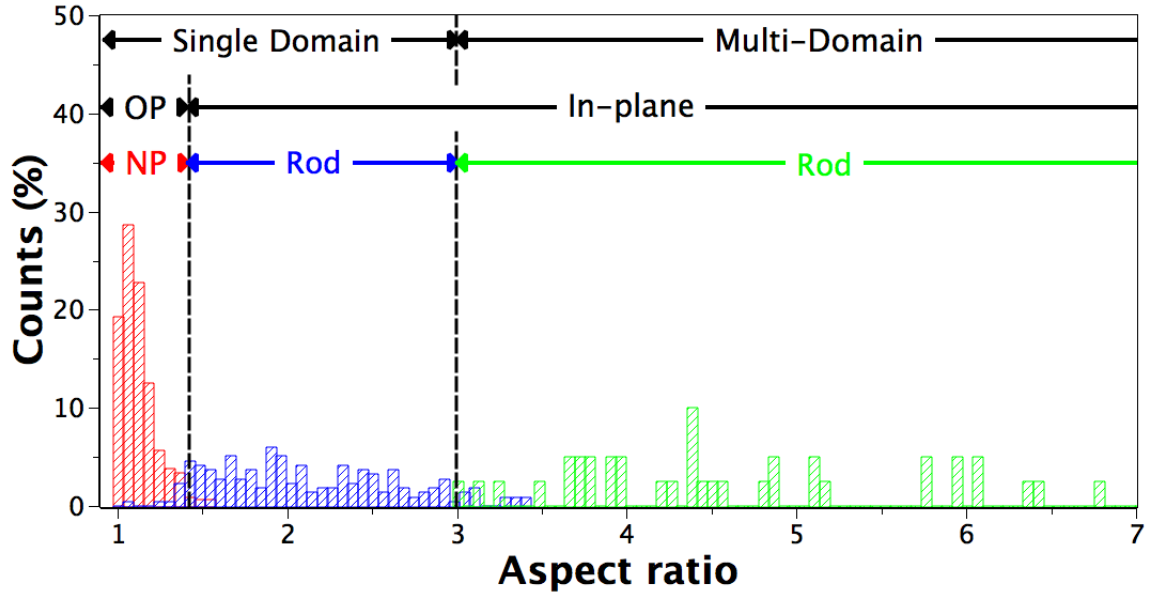


Figure 5.10: Histogram of the in-plane aspect ratio (AR) distribution of nanostructures along with the nature of magnetic domain (single- vs multi-domain) and their magnetization orientation. The histogram indicates that the single domain and multi-domain nanostructure exists in the range of $1 < AR < 3$ and $AR \geq 3$, respectively. The AR values for out-of-plane and in-plane magnetization, as well as multi-domain magnetization are also shown

each nanowire and rod are made of continuous single domain spheres, the chain of spheres, where only point contact occurs between the spheres and hence, the exchange force can be treated as being discontinuous at the boundary. Therefore, magnetization reversal can be assumed to occur independently for each particle in the chain of spheres [16, 71]. According to the model, the coercivity can be obtained from the below expressions:

$$H_n = \left(\frac{\mu}{a^3}\right) (6K_n - 4L_n) \quad (5.1)$$

$$L_n = \sum_{j=1}^{\frac{1}{2}(n-1) \leq j \leq \frac{1}{2}(n+1)} \frac{[n - (2j - 1)]}{n(2j - 1)^3}, \quad (5.2)$$

$$K_n = \sum_{j=1}^{n_j} \frac{(n - j)}{nj^3}, \quad (5.3)$$

$$\mu = M_s \left(\frac{4\pi}{3}\right) \left(\frac{a}{2}\right)^3 \quad (5.4)$$

where μ is the dipole moment of a sphere; a is the sphere diameter, n is the number of spheres in the nanowire or rod, i and j are integers from 1 to n , and M_s is the saturation magnetization of Co.

From the histograms in Fig. 5.3, the single-wire, nanorod, and nanoparticle had average aspect ratio of 1.1, 4.2 and 17 (aspect ratio = length / width), respectively. In this calculation, the number of spheres, n , is

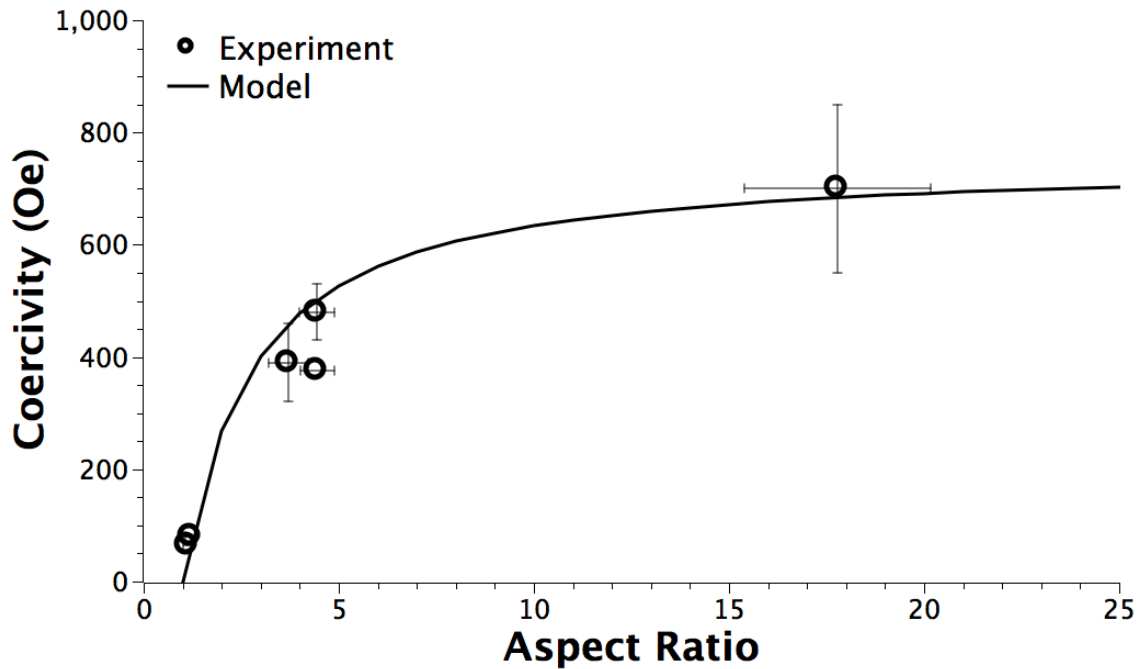


Figure 5.11: Measured values of the in-plane coercivity of Co nanowire, nanorod, and nanoparticle arrays (open circles) compared to the theoretical trend in coercivity obtained by the chain-of-spheres model [16].

equivalent to the aspect ratio. From the histogram, both the single-wire and nanorod have comparable width ($\sim 6\%$ difference), hence $n \approx$ aspect ratio. In Fig. 5.11, experimentally measured coercivity values of nanostructures with respect to the aspect ratio are plotted. Then, the experimental coercivity were compared to the theoretical values calculated from the model. The solid line represents the best fit line of the experimental data points with respect to the aspect ratio based on the model. The trend of the experimental data points and the model calculation result agree well. In addition, the intrinsic coercivity value, $H_{ci} (= \mu/a^3)$, can be calculated from the fitted data. Interestingly, $H_{ci,fit} = 250$ (Oe) is three times smaller than the previously reported value [183, 16]. One explanation can be the difference in width of our structures compared with the previous study. The average width of our samples are approximately 85% smaller then the width of nanowires of the previous study, and could be the reason for this mismatch [71].

5.6 Conclusion

In conclusion, we successfully fabricated various nanostructures of ferromagnetic materials (Co and Ni) like arrays of nanowires, nanorods and nanoparticles using nanosecond pulsed laser synthesis technique. The magnetic switching behavior and domain property of the arrays of ferromagnetic nanomaterials were studied using SMOKE and MFM characterization techniques. The study of hemispherical shaped Co and Ni nanoparticles with varying average size showed that systematic differences in saturation and coercivity were observed as a function of size and material. Second, the study of periodic arrays of Co nanowires, nanorods and nanoparticles showed that magnetic domain properties depends on the aspect ratio. We found that the magnetization direction was out-of-plane for the aspect ratio, $1 < AR < 1.4$ and transitioned to an

in-plane orientation for the aspect ratios greater than 1.4. From the hysteresis loop measurements of Co nanostructure arrays using SMOKE, large in-plane magnetic anisotropy was observed for Co nanowires along the wire direction. On the other hand, no large in-plane magnetic anisotropy was observed for Co nanoparticles. This result was mainly attributed to the shape anisotropy. Besides, the relation between the nanostructure coercivity and the aspect ratio was predicted by the chain of spheres model.

Chapter 6

Summary and Future work

6.1 Summary

This chapter first summarizes the key findings of this thesis and outlines some future directions of research based on results that were obtained during the research (sec. 6.2). The scientific and technological motivation of this research was presented in the introductory message in chapter 1. Primarily, synthesis of nanostructures by pulsed laser melting, both under two-beam interference irradiation as well as single beam irradiation, and the subsequent characterization of their structure and physical properties was undertaken.

- One of the materials focused upon was SnO₂ (Ch 2) and the formation of 1D periodic arrays of surface height modulation was investigated with the goal of forming nanowires for hydrogen sensing. We successfully detailed the mechanisms of surface structure formation by comparing experimental results pertaining to the variation in nanostructure characteristics such as height and width and its dependence on laser energy density and film thickness. One of the primary findings was that evaporation of SnO₂ was the most significant contributor to the pattern formation as compared to surface or bulk mass transport in the solid or liquid phase. As a result of the non-monotonic dependence of temperature on local film height, the synthesis process was self-limiting since it stopped as soon as the local film height reached a lower thickness value, that corresponded to the film going below its evaporation regime. This finding was confirmed by performing numerical modeling of the thermal behavior of the pulsed laser interference heating of the films.
- In Ch 3, we adapted the viscous dissipation approach for fluid flow, as developed by de Gennes and others [158, 159] and specifically applied it to the process of spontaneous thin film spinodal dewetting for pulsed laser heating, which can introduce novel non-isothermal behavior [12]. The motivation for this work was to realize a more physically insightful, but at the same time, a simple route to understand the behavior of fluids during the spinodal dewetting process. The central concept was that by equating the rate of free energy decrease to the rate of frictional loss via viscous dissipation can give information on the characteristic spinodal dewetting length and time scales as well as other attributes of the flow. Here we successfully applied it to the case of nanosecond pulsed laser melting for situations in which a film-thickness- (h) dependent thermocapillary force arises. The results of

this modeling agreed with those from linear theory as well as experimental observations provided the minimum dissipation was equated to the rate of free energy decrease. We found that the flow boundary condition that produces this minimum dissipation was when the film-substrate tangential stress was zero. The physical implication of this finding was that the spontaneous dewetting instability follows the path of minimum rate of energy loss. Subsequently, this model was utilized by a member of our group to describe the first experimental study of spinodal dewetting in multilayer metallic liquids [184].

- In Ch 4, we detailed the successful implementation of a home-built SMOKE system, inside a magnetic field of 0.7 T, for measurement of magnetic and magneto-optical properties of surfaces and nanostructures with various magnetic field orientations. We successfully measured the Kerr rotation from Co-Ag thin films and nanoparticles as a function of composition. Films made by co-deposition of Co and Ag showed higher Kerr rotation than bilayer film structures with same effective amount of Co and Ag. Furthermore, nanoparticles showed a factor of 2 or higher Kerr rotation than composite films of similar Co composition ranging between 35 to 100%.
- Finally, in Ch 5, we studied the magnetic properties of nanostructures of Co and Ni, specifically hemispherical nanoparticles and arrays of Co nanowires, nanorods and nanoparticles, prepared by the pulsed laser process. Magnetic hysteresis was studied by SMOKE. While SMOKE has been applied in the past to investigate the magnetic information of continuous films, there was little work, prior to this investigation, on applying it to characterize arrays of nanostructures with variable shape and size. SMOKE measurements as a function of different particle size and material, showed systematic differences in saturation and coercivity. The key result was a confirmation of the single-domain orientation anisotropy as a function of size, which was previously discovered via MFM measurements by a previous member of the group [5, 113]. Periodic arrays of Co nanowires, nanorods and nanoparticles were fabricated by pulsed laser interference irradiation, and, in addition to SMOKE, MFM was used to investigate the magnetic domain properties. The key result here was that domain orientation was found to depend on the in-plane aspect ratio of the nanostructure. It was determined that the magnetic orientation was out-of-plane for shapes with in-plane aspect ratio ranging from 1 to 1.3 and transitioned to an in-plane orientation for aspect ratios greater than 1.4 (such as in nanorods and nanowires). These results also demonstrated that nanosecond pulsed laser synthesis is capable of fabricating various nanostructures in a simple, robust and rapid manner and that SMOKE is a reliable technique to rapidly characterize the magnetic behavior of nanostructures.

6.2 Future directions

6.2.1 In₂O₃-doped SnO₂ NSA based hydrogen sensor

In the previous chapter (Ch. 2), we discussed in details of synthesis of 1-D SnO₂ nanostructured arrays (NSA) and H₂ gas sensing evaluations. In the near future, we will also incorporate Indium-oxide (In₂O₃) as a dopant into SnO₂ NSA to enhance even further the sensitivity to hydrogen gas detection. In fact, Shukla

et al. showed hydrogen gas sensing with the concentration of 100 ppm at low operating temperature (25 °C) using In₂O₃-doped SnO₂ thin film sensor [56]. Doping SnO₂ with oxides having tri- or di-valent metal ions will increase oxygen-ion vacancy concentration to keep the charge-balance. This increase of the vacancy enhances adsorption of oxygen-ions (O⁻) on the surface. Hence increasing depletion layer thickness leads to maximize hydrogen gas sensitivity.

6.2.2 Wavelength-dependent SMOKE of plasmonic-ferromagnetic (PF) composites

A group in Spain has shown that nanostructures made by combining strongly plasmonic materials like Au and Ag along with the ferromagnetic elements (Co, Fe or Ni) can show resonant magneto-optical phenomenon, such as the Kerr effect [83]. One of the primary findings of these studies has been that the proximity of the plasmonic and ferromagnetic metal leads to energy transfer between the two and can be seen in the field on literature on this topic has primarily focused on making layered structures (thin films) or patterned dots of these layered structures, made by lithography. In our group's research, we have been working extensively on the Ag-Co system, both from the perspective of understanding self-organization in multi-metal systems as well as determining the physical structure of the nanomaterials. Recently, work in collaboration with Western Kentucky University has shown that Ag-Co nanoparticles fabricated by the multilayer laser dewetting process can have unique structures, including stacked, core-shell and embedded states [185]. Ongoing experimental work by one of the collaborators has shown by transmission electron microscopy investigations that indeed, many different types of nanoparticle structures might be forming, as shown in Fig. 6.1 [17, 186]. Furthermore, our group has already published results that show that the localized plasmon resonance of such particles is a function of composition [187]. Therefore, it will be of tremendous interest to study the incident light wavelength-dependent Kerr rotation of such nanostructures in the future.

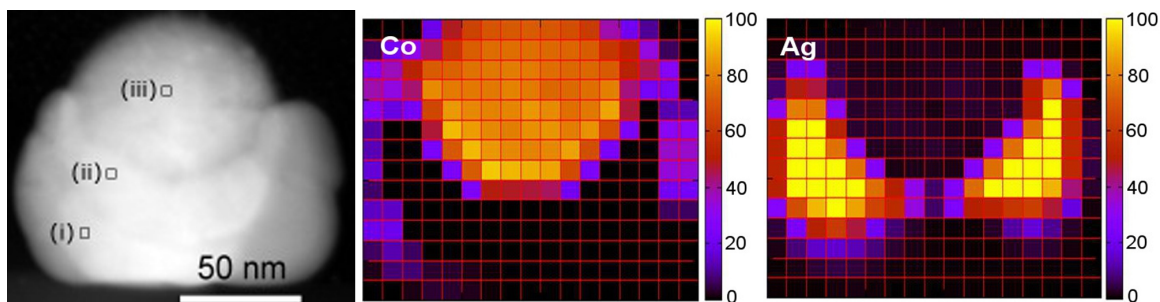


Figure 6.1: (left) *Cross-sectional TEM image of a Ag-Co nanoparticle made from Co-Ag bilayer films showing contrast variation indicating polycrystallinity within the particle.* (center) *Co and (right) Ag EELS elemental maps of the enclosed region shown in left image, exhibiting the immiscibility of Co and Ag in each other.* *The contrast bar shows the variation of atom % of Ag and Co individually in different locations. The size of elemental map image is 5.9 nm x 5.9 nm [17].*

In order to perform wavelength-dependent MOKE measurements, broadband optical spectroscopy will be employed to identify the LSPR wavelength (λ_p) of the PF nanoparticles. Standard UV-Vis spectroscopy

techniques can be used for measurement of transmission and reflection spectra, from which the LSPR information can be obtained. Subsequently, the Kerr rotation of the PF nanoparticles can be quantified by the SMOKE measurements performed with different light wavelengths. In this technique, light of a fixed polarization is incident on the nanoparticle array, and the changes in the reflected light, including polarization rotation, absorption or an intensity change, is measured under varying magnetic field strength and orientation. By measurements at different light wavelength, including the LSPR wavelength (λ_p) it will be possible to generate the wavelength-dependent reflectivity and determine if large magnitudes of Kerr rotation, which is important for sensing applications. SMOKE measurements will also yield the hysteresis behavior of the PF material.

List of References

- [1] H. Krishna, N. Shirato, C. Favazza, and R. Kalyanaraman, “Energy driven self-organization in nanoscale metallic liquid films,” *Phys. Chem. Chem. Phys.*, 2009.
- [2] N. Barsan, D. Koziej, and U. Weimar, “Metal oxide-based gas sensor research: How to?,” *Sensors and Actuators B: Chemical*, vol. 121, pp. 18–35, 1 2007.
- [3] A. Kolmakov, D. O. Klenov, Y. Lilach, S. Stemmer, and M. Moskovits, “Enhanced gas sensing by individual SnO_2 nanowires and nanobelts functionalized with Pd catalyst particles,” *Nano Letters*, vol. 5, pp. 667–673, 2012/02/14 2005.
- [4] S. Seal University of Central Florida.
- [5] H. Krishna, C. Miller, L. Longstreth-Spoor, Z. Nussinov, A. K. Gangopadhyay, and R. Kalyanaraman, “Unusual size-dependent magnetization in near hemispherical Co nanomagnets on SiO_2 from fast pulsed laser processing,” *Journal of Applied Physics*, vol. 103, no. 7, p. 073902, 2008.
- [6] Y. Henry, K. Ounadjela, L. Piraux, S. Dubois, J. M. George, and J. L. Duvail, “Magnetic anisotropy and domain patterns in electrodeposited cobalt nanowires,” *The European Physical Journal B - Condensed Matter and Complex Systems*, vol. 20, no. 1, pp. 35–54, 2001-03-19.
- [7] S. Camazine, J.-I. Deneubougr, N. R. Franks, J. Sneyd, G. Theraulaz, and E. Bonabeau, *Self-organization in biological systems*. Princeton University Press, 2001.
- [8] A. M. Zhabotinsky and A. N. Zaikin, “Autowave processes in a distributed chemical system,” *Journal of Theoretical Biology*, vol. 40, pp. 45–61, 7 1973.
- [9] C. Favazza, J. Trice, R. Kalyanaraman, and R. Sureshkumar, “Self-organized metal nanostructures through laser-interference driven thermocapillary convection,” *Applied Physics Letters*, vol. 91, no. 4, p. 043105, 2007.
- [10] G. Reiter, “Dewetting of thin polymer films,” *Physical Review Letters*, vol. 68, pp. 75–78, 01 1992.
- [11] R. Seemann, S. Herminghaus, and K. Jacobs, “Gaining control of pattern formation of dewetting liquid films,” *J. Phys. Cond. Matt.*, vol. 13, p. 4925, 2001.

- [12] J. Trice, C. Favazza, D. Thomas, H. Garcia, R. Kalyanaraman, and R. Sureshkumar, "Novel self-organization mechanism in ultrathin liquid films: theory and experiment," *Phys. Rev. Lett.*, vol. 101, no. 1, p. 017802, 2008.
- [13] T. Jean-Marc, C. Mohammed, H. Luc, L. Philippe, D. Jacques, and G. Jean-Marie, "Characterization of tin oxides by x-ray-photoemission spectroscopy," *Phys. Rev. B*, vol. 46, pp. 2460–2466, Jul 1992.
- [14] R. McCormack, N. Shirato, U. Singh, S. Das, A. Kumar, H. J. Cho, R. Kalyanaraman, and S. Seal, "Improved hydrogen sensing characteristics of nano-architected tin oxide at room temperature." unpublished.
- [15] R. J. Gambino, *Magneto-optical recording materials*. Piscataway, NJ: IEEE press marketing, 2000.
- [16] I. S. Jacobs and C. P. Bean, "An approach to elongated fine-particle magnets," *Physical Review*, vol. 100, pp. 1060–1067, 11 1955.
- [17] R. Sachan, S. Yadavali, N. Shirato, H. Krishna, V. Ramos, G. Duscher, S. Pennycook, A. Gangopadhyay, H. Garcia, and R. Kalyanaraman, "Self-organized bimetallic ag-co nanoparticles with tunable localized surface plasmons showing high environmental stability and sensitivity," *Nanotechnology*, 2012.
- [18] R. P. Feynman, "There's plenty of room at the bottom," *Caltech Engineering and Science*, vol. 23, pp. 22–36, February 1960.
- [19] G. Binnig, H. Rohrer, C. Gerber, and E. Weibel, "Surface studies by scanning tunneling microscopy," *Physical Review Letters*, vol. 49, pp. 57–61, 07 1982.
- [20] D. Derkacs, S. H. Lim, P. Matheu, W. Mar, and E. T. Yu, "Improved performance of amorphous silicon solar cells via scattering from surface plasmon polaritons in nearby metallic nanoparticles," *Applied Physics Letters*, vol. 89, no. 9, p. 093103, 2006.
- [21] P. V. Kamat, "Meeting the clean energy demand: Nanostructure architectures for solar energy conversion," *J. Phys. Chem. C*, vol. 111, no. 7, pp. 2834–2860, 2007.
- [22] M. Law, L. E. Greene, J. C. Johnson, R. Saykally, and P. Yang, "Nanowire dye-sensitized solar cells," *Nat Mater*, vol. 4, pp. 455–459, 06 2005.
- [23] S. Pillai, K. R. Catchpole, T. Trupke, and M. A. Green, "Surface plasmon enhanced silicon solar cells," *Journal of Applied Physics*, vol. 101, no. 9, p. 093105, 2007.
- [24] D. M. Schaadt, B. Feng, and E. T. Yu, "Enhanced semiconductor optical absorption via surface plasmon excitation in metal nanoparticles," *Applied Physics Letters*, vol. 86, no. 6, p. 063106, 2005.
- [25] A. T. Bell, "The impact of nanoscience on heterogeneous catalysis," *Science*, vol. 299, pp. 1688–1691, 03 2003.

- [26] K. S. Soppimath, T. M. Aminabhavi, A. R. Kulkarni, and W. E. Rudzinski, "Biodegradable polymeric nanoparticles as drug delivery devices," *Journal of Controlled Release*, vol. 70, pp. 1–20, 1 2001.
- [27] X. Gao, Y. Cui, R. M. Levenson, L. W. K. Chung, and S. Nie, "In vivo cancer targeting and imaging with semiconductor quantum dots," *Nat Biotech*, vol. 22, pp. 969–976, 08 2004.
- [28] C. Loo, A. Lowery, N. Halas, J. West, and R. Drezek, "Immunotargeted nanoshells for integrated cancer imaging and therapy," *Nano Letters*, vol. 5, pp. 709–711, 2012/03/04 2005.
- [29] J. N. Anker, W. P. Hall, O. Lyandres, N. C. Shah, J. Zhao, and R. P. Van Duyne, "Biosensing with plasmonic nanosensors," *Nat Mater*, vol. 7, pp. 442–453, 06 2008.
- [30] Y. C. Cao, R. Jin, and C. A. Mirkin, "Nanoparticles with raman spectroscopic fingerprints for dna and rna detection," *Science*, vol. 297, pp. 1536–1540, 08 2002.
- [31] S. Mornet, S. Vasseur, F. Grasset, and E. Duguet, "Magnetic nanoparticle design for medical diagnosis and therapy," *Journal of Materials Chemistry*, vol. 14, no. 14, 2004.
- [32] N. L. Rosi and C. A. Mirkin, "Nanostructures in biodiagnostics," *Chemical Reviews*, vol. 105, pp. 1547–1562, 2012/03/04 2005.
- [33] T. A. Taton, C. A. Mirkin, and R. L. Letsinger, "Scanometric dna array detection with nanoparticle probes," *Science*, vol. 289, pp. 1757–1760, 09 2000.
- [34] A. N. Shipway, E. Katz, and I. Willner, "Nanoparticle arrays on surfaces for electronic, optical, and sensor applications," *ChemPhysChem*, vol. 1, no. 1, pp. 18–52, 2000.
- [35] J. Muth, R. Kolbas, A. Sharma, S. Oktyabrsky, and J. Narayan, "Excitonic structure and absorption coefficient measurements of ZnO single crystal epitaxial films deposited by pulsed laser deposition," *JOURNAL OF APPLIED PHYSICS*, vol. 85, pp. 7884–7887, JUN 1 1999.
- [36] D. Dijkkamp, T. Venkatesan, X. D. Wu, S. A. Shaheen, N. Jisrawi, Y. H. Min-Lee, W. L. McLean, and M. Croft, "Preparation of y-ba-cu oxide superconductor thin films using pulsed laser evaporation from high t_{c} bulk material," *Applied Physics Letters*, vol. 51, no. 8, pp. 619–621, 1987.
- [37] A. Kumar and J. Narayan, "Superconducting $yba_2cu_3o_{7-\delta}$ thin films on si (100) substrates with $cosi_2$ buffer layers by an in situ pulsed laser evaporation method," *Applied Physics Letters*, vol. 59, no. 14, pp. 1785–1787, 1991.
- [38] R. K. Singh, D. Bhattacharya, P. Tiwari, J. Narayan, and C. B. Lee, "Improvement in the properties of high t_{c} films fabricated in situ by laser ablation of $yba_2cu_3o_7$ -ag targets," *Applied Physics Letters*, vol. 60, no. 2, pp. 255–257, 1992.
- [39] X. D. Wu, D. Dijkkamp, S. B. Ogale, A. Inam, E. W. Chase, P. F. Miceli, C. C. Chang, J. M. Tarascon, and T. Venkatesan, "Epitaxial ordering of oxide superconductor thin films on (100) $srtio_3$ prepared by pulsed laser evaporation," *Applied Physics Letters*, vol. 51, no. 11, pp. 861–863, 1987.

- [40] J. Bischof, D. Scherer, S. Herminghaus, and P. Leiderer, “Dewetting modes of thin metallic films: nucleation of holes and spinodal dewetting,” *Phys. Rev. Lett.*, vol. 77, no. 8, pp. 1536–1539, 1996.
- [41] S. Herminghaus, K. Jacobs, K. Mecke, J. Bischof, A. Fery, M. Ibn-Elhaj, and S. Schlagowski, “Spinodal dewetting in liquid crystal and liquid metal films,” *Science*, vol. 282, pp. 916–919, 1998.
- [42] J. D. Fowlkes, L. Kondic, J. Diez, Y. Wu, and P. D. Rack, “Self-assembly versus directed assembly of nanoparticles via pulsed laser induced dewetting of patterned metal films,” *Nano Letters*, vol. 11, pp. 2478–2485, 2012/02/21 2011.
- [43] C. Favazza, R. Kalyanaraman, and R. Sureshkumar, “Robust nanopatterning by laser-induced dewetting of metal nanofilms,” *Nanotechnology*, vol. 17, no. 16, 2006.
- [44] H. Krishna, N. Shirato, C. Favazza, and R. Kalyanaraman, “Energy driven self-organization in nanoscale metallic liquid films,” *Phys. Chem. Chem. Phys.*, vol. 11, pp. 8136–8143, 2009.
- [45] E. Comini, V. Guidi, C. Malagù, G. Martinelli, Z. Pan, G. Sberveglieri, and Z. L. Wang, “Electrical properties of tin dioxide two-dimensional nanostructures,” *The Journal of Physical Chemistry B*, vol. 108, pp. 1882–1887, 2012/02/14 2004.
- [46] P. K. Jain, Y. Xiao, R. Walsworth, and A. E. Cohen, “Surface plasmon resonance enhanced magneto-optics (supremo): Faraday rotation enhancement in gold-coated iron oxide nanocrystals,” *Nano Letters*, vol. 9, pp. 1644–1650, 2012/02/14 2009.
- [47] J. B. González-Díaz, A. García-Martín, J. García-Martín, A. Cebollada, G. Armelles, B. Sepúlveda, Y. Alaverdyan, and M. Käll, “Plasmonic au/co/au nanosandwiches with enhanced magneto-optical activity,” *Small*, vol. 4, no. 2, pp. 202–205, 2008.
- [48] Y. Li, Q. Zhang, A. V. Nurmikko, and S. Sun, “Enhanced magneto-optical response in dumbbell-like ag-cofe₂o₄ nanoparticle pairs,” *Nano Letters*, vol. 5, pp. 1689–1692, 2012/02/14 2005.
- [49] S. S. P. Parkin, M. Hayashi, and L. Thomas, “Magnetic domain-wall racetrack memory,” *Science*, vol. 320, no. 5873, pp. 190–194, 2008.
- [50] A. Yamaguchi, T. Ono, S. Nasu, K. Miyake, K. Mibu, and T. Shinjo, “Real-space observation of current-driven domain wall motion in submicron magnetic wires,” *Physical Review Letters*, vol. 92, pp. 077205–, 02 2004.
- [51] N. Vernier, D. A. Allwood, D. Atkinson, M. D. Cooke, and R. P. Cowburn, “Domain wall propagation in magnetic nanowires by spin-polarized current injection,” *EPL (Europhysics Letters)*, vol. 65, no. 4, 2004.
- [52] A. J. Haes and R. P. Van Duyne, “A nanoscale optical biosensor: Sensitivity and selectivity of an approach based on the localized surface plasmon resonance spectroscopy of triangular silver nanoparticles,” *Journal of the American Chemical Society*, vol. 124, pp. 10596–10604, 2012/03/04 2002.

- [53] C. Wu and Q.-H. Xu, "Stable and functionable mesoporous silica-coated gold nanorods as sensitive localized surface plasmon resonance (lspr) nanosensors," *Langmuir*, vol. 25, pp. 9441–9446, 2012/03/04 2009.
- [54] G. H. Lu, L. E. Ocola, and J. H. Chen, "Room temperature gas sensing based on electron transfer between discrete tin oxide nanocrystals and multiwalled carbon nanotubes," *Advanced Materials*, vol. 21, p. 24, 2009.
- [55] M. Batzill and U. Diebold, "The surface and materials science of tin oxide," *Progress in Surface Science*, vol. 79, p. 47, 2005.
- [56] S. Shukla, S. Seal, L. Ludwig, and C. Parish, "Nanocrystalline indium oxide-doped tin oxide thin film as low temperature hydrogen sensor," *Sensors and Actuators B: Chemical*, vol. 97, no. 2-3, pp. 256 – 265, 2004.
- [57] G. Zhang and M. Liu, "Effect of particle size and dopant on properties of sno2-based gas sensors," *Sensors and Actuators B: Chemical*, vol. 69, no. 1-2, pp. 144 – 152, 2000.
- [58] A. Licciulli, S. Mazzarelli, G. De, P. Siciliano, L. Vasanelli, and R. Rella, "Os and pd modified tin oxide films for sensors by the sol gel process," *Journal of Sol-Gel Science and Technology*, vol. 21, no. 3, pp. 195–201, 2001.
- [59] F. B. Theodore, O. K. Sergei, E. G. Alexander, and H. S. Joe, "Facile synthesis of a crystalline high-surface area sno2 aerogel," *Advanced Materials*, vol. 17, 2005.
- [60] F. Cosandey, G. Skandean, and A. Singhal, "Materials and processing issues in nanostructured semiconductor gas sensors," *JOM-e*, 2000.
- [61] M. Law, H. Kind, B. Messer, F. Kim, and P. D. Yang *Angew Chem Int Ed*, vol. 41, p. 2405, 2002.
- [62] Z. Fan, J. C. Ho, T. Takahashi, R. Yerushalmi, K. Takei, A. C. Ford, Y.-L. Chueh, and A. Javey, "Toward the development of printable nanowire electronics and sensors," *Advanced Materials*, vol. 21, no. 37, pp. 3730–3743, 2009.
- [63] B. N., "Conduction models in gas-sensing sno2 layers: grain-size effects and ambient atmosphere influence," *Sensors and Actuators B: Chemical*, vol. 17, pp. 241–246, 2 1994.
- [64] N. M. Sammes and R. Boersma, "Small-scale fuel cells for residential applications," *Journal of Power Sources*, vol. 86, no. 1-2, pp. 98 – 110, 2000.
- [65] M. Mogensen, M. S. Nigel, and G. A. Tompsett, "Physical, chemical and electrochemical properties of pure and doped ceria," *Solid State Ionics*, vol. 129, no. 1-4, pp. 63 – 94, 2000.
- [66] C. M. White, R. R. Steeper, and A. Lutz, "The hydrogen-fueled internal combustion engine: a technical review," *International Journal of Hydrogen Energy*, vol. 31, no. 10, pp. 1292 – 1305, 2006.

- [67] C. Drake, A. Amalu, J. Bernard, and S. Seal, "Enhancing the low temperature hydrogen sensitivity of nanocrystalline SnO_2 as a function of trivalent dopants," *Journal of Applied Physics*, vol. 101, 2007.
- [68] S. G. Ansari, P. Borojerdian, S. R. Sainkar, R. N. Karekar, R. C. Aiyer, and S. K. Kulkarni, "Grain size effects on H_2 gas sensitivity of thick film resistor using SnO_2 nanoparticles," *Thin Solid Films*, vol. 295, p. 271, 1997.
- [69] B. S. Archanjo, G. V. Silveira, A.-M. B. Goncalves, D. C. B. Alves, A. S. Ferlauto, R. G. Lacerda, and B. R. A. Neves, "Fabrication of gas nanosensors and microsensors via local anodic oxidation," *Langmuir*, vol. 25, pp. 602–605, 2012/03/09 2008.
- [70] B. D. Cullity and C. D. Graham, *Introduction to Magnetic Materials*. Wiley, 2nd ed., 2009.
- [71] Y. Peng, H.-L. Zhang, S.-L. Pan, and H.-L. Li, "Magnetic properties and magnetization reversal of alpha- Fe nanowires deposited in alumina film," *Journal of Applied Physics*, vol. 87, no. 10, pp. 7405–7408, 2000.
- [72] G. Vieira, T. Henighan, A. Chen, A. J. Hauser, F. Y. Yang, J. J. Chalmers, and R. Sooryakumar, "Magnetic wire traps and programmable manipulation of biological cells," *Physical Review Letters*, vol. 103, pp. 128101–, 09 2009.
- [73] D. Niarchos, "Magnetic mems: key issues and some applications," *Sensors and Actuators A: Physical*, vol. 109, pp. 166–173, 12 2003.
- [74] P. M. Hui and D. Stroud, "Theory of faraday rotation by dilute suspensions of small particles," *Applied Physics Letters*, vol. 50, no. 15, pp. 950–952, 1987.
- [75] H. Feil and C. Haas, "Magneto-optical kerr effect, enhanced by the plasma resonance of charge carriers," *Physical Review Letters*, vol. 58, pp. 65–68, 01 1987.
- [76] T. Katayama, Y. Suzuki, H. Awano, Y. Nishihara, and N. Koshizuka, "Enhancement of the magneto-optical kerr rotation in Fe/Cu bilayered films," *Physical Review Letters*, vol. 60, pp. 1426–1429, 04 1988.
- [77] V. I. Safarov, V. A. Kosobukin, C. Hermann, G. Lampel, J. Peretti, and C. Marlière, "Magneto-optical effects enhanced by surface plasmons in metallic multilayer films," *Physical Review Letters*, vol. 73, pp. 3584–3587, 12 1994.
- [78] S. A. Maier, *Plasmonics: Fundamentals and Applications*. Springer, 1 ed., 2007.
- [79] A. Zvezdin and V. Kotov, *Modern Magneto-optics and Magneto-optical Materials, Studies in Condensed Matter Physics*. Bristol and Philadelphia: Institute of Physics Publishing, 1997.
- [80] A. Masanori and G. Manabu, "Magneto-optical effect and effective dielectric tensor in composite material containing magnetic fine particles or thin layers," *Japanese journal of applied physics*, vol. 23, no. 12, pp. 1580–1585, 1984.

- [81] V. I. Belotelov, L. L. Doskolovich, and A. K. Zvezdin, "Extraordinary magneto-optical effects and transmission through metal-dielectric plasmonic systems," *Physical Review Letters*, vol. 98, pp. 077401–, 02 2007.
- [82] M. Abe and T. Suwa, "Surface plasma resonance and magneto-optical enhancement in composites containing multicore-shell structured nanoparticles," *Physical Review B*, vol. 70, pp. 235103–, 12 2004.
- [83] B. Sep'urveda, A. Calle, L. M. Lechuga, and G. Armelles, "Highly sensitive detection of biomolecules with the magneto-optic surface-plasmon-resonance sensor," *Opt. Lett.*, vol. 31, pp. 1085–1087, 04 2006.
- [84] V. G. Kravets and A. S. Lapchuk, "Enhancement of magneto-optical effects in magnetic nanoparticles near gold-dielectric surfaces," *Appl. Opt.*, vol. 49, pp. 5013–5019, 09 2010.
- [85] N. Bonod, R. Reinisch, E. Popov, and M. Nevière, "Optimization of surface-plasmon-enhanced magneto-optical effects," *J. Opt. Soc. Am. B*, vol. 21, pp. 791–797, Apr 2004.
- [86] S. Tomita, T. Kato, S. Tsunashima, S. Iwata, M. Fujii, and S. Hayashi, "Magneto-optical kerr effects of yttrium-iron garnet thin films incorporating gold nanoparticles," *Physical Review Letters*, vol. 96, pp. 167402–, 04 2006.
- [87] R. Fujikawa, A. V. Baryshev, J. Kim, H. Uchida, and M. Inoue, "Contribution of the surface plasmon resonance to optical and magneto-optical properties of a bi:zig-au nanostructure," *Journal of Applied Physics*, vol. 103, no. 7, p. 07D301, 2008.
- [88] S. Peng, C. Lei, Y. Ren, R. E. Cook, and Y. Sun, "Plasmonic/magnetic bifunctional nanoparticles," *Angewandte Chemie International Edition*, vol. 50, no. 14, pp. 3158–3163, 2011.
- [89] Z. Q. Qiu and S. D. Bader, "Surface magneto-optic kerr effect," *Review of Scientific Instruments*, vol. 71, no. 3, pp. 1243–1255, 2000.
- [90] R. P. Cowburn, D. K. Koltsov, A. O. Adeyeye, M. E. Welland, and D. M. Tricker, "Single-domain circular nanomagnets," *Physical Review Letters*, vol. 83, 08 1999/08/02/.
- [91] R. P. Cowburn, S. J. Gray, and J. A. C. Bland, "Multijump magnetic switching in in-plane magnetized ultrathin epitaxial ag/fe/ag(001) films," *Physical Review Letters*, vol. 79, pp. 4018–4021, 11 1997.
- [92] G. Whitesides, J. Mathias, and C. Seto, "Molecular self-assembly and nanochemistry: a chemical strategy for the synthesis of nanostructures," *Science*, vol. 254, no. 5036, pp. 1312–1319, 1991.
- [93] A. N. Zaikin and A. M. M. Zhabotinsky, "Concentration wave propagation in two-dimensional liquid-phase self-oscillating system," *Nature*, vol. 225, pp. 535–537, 02 1970.
- [94] E. Karsenti, "Self-organization in cell biology: a brief history," *Nat Rev Mol Cell Biol*, vol. 9, pp. 255–262, 03 2008.

- [95] G. M. Whitesides and B. Grzybowski, "Self-assembly at all scales," *Science*, vol. 295, no. 5564, pp. 2418–2421, 2002.
- [96] A. Vrij, "Possible mechanism for the spontaneous rupture of thin, free liquid films," *Discuss. Faraday Soc.*, vol. 42, pp. 23–27, 1966.
- [97] A. Vrij and J. T. G. Overbeek, "Rupture of Thin Liquid Films Due to Spontaneous Fluctuations in Thickness," *J. Am. Chem. Soc.*, vol. 90, pp. 3074–78, 1968.
- [98] A. Sharma, "Relationship of thin film stability and morphology to macroscopic parameters of wetting in the apolar and polar systems," *Langmuir*, vol. 9, pp. 861–869, 2012/02/23 1993.
- [99] A. Sharma and R. Khanna, "Pattern formation in unstable thin liquid films," *Physical Review Letters*, vol. 81, pp. 3463–3466, 10 1998.
- [100] A. Sharma and G. Reiter, "Instability of thin polymer films on coated substrates: Rupture, dewetting, and drop formation," *Journal of Colloid and Interface Science*, vol. 178, pp. 383–399, 3 1996.
- [101] G. Reiter, "Unstable thin polymer films: rupture and dewetting processes," *Langmuir*, vol. 9, pp. 1344–1351, 2012/02/17 1993.
- [102] G. Reiter, A. Sharma, A. Casoli, M.-O. David, R. Khanna, and P. Auroy, "Thin film instability induced by long-range forces," *Langmuir*, vol. 15, pp. 2551–2558, 2012/02/17 1999.
- [103] R. Xie, A. Karim, J. F. Douglas, C. C. Han, and R. A. Weiss, "Spinodal dewetting of thin polymer films," *Physical Review Letters*, vol. 81, pp. 1251–1254, 08 1998.
- [104] S. J. Henley, J. D. Carey, and S. R. P. Silva, "Pulsed-laser-induced nanoscale island formation in thin metal-on-oxide films," *Physical Review B*, vol. 72, pp. 195408–, 11 2005.
- [105] J. Trice, D. Thomas, C. Favazza, R. Sureshkumar, and R. Kalyanaraman, "Pulsed-laser-induced dewetting in nanoscopic metal films: Theory and experiments," *Physical Review B*, vol. 75, pp. 235439–, 06 2007.
- [106] C. Favazza, R. Kalyanaraman, and R. Sureshkumar, "Dynamics of ultrathin metal films on amorphous substrates under fast thermal processing," *Journal of Applied Physics*, vol. 102, no. 10, p. 104308, 2007.
- [107] X. Hu, D. G. Cahill, and R. S. Averback, "Nanoscale pattern formation in pt thin films due to ion-beam-induced dewetting," *Applied Physics Letters*, vol. 76, no. 22, pp. 3215–3217, 2000.
- [108] X. Hu, D. G. Cahill, and R. S. Averback, "Dewetting and nanopattern formation of thin pt films on sio₂ induced by ion beam irradiation," *Journal of Applied Physics*, vol. 89, no. 12, pp. 7777–7783, 2001.

- [109] X. Hu, D. G. Cahill, R. S. Averback, and R. C. Birtcher, "In situ transmission electron microscopy study of irradiation induced dewetting of ultrathin pt films," *Journal of Applied Physics*, vol. 93, no. 1, pp. 165–169, 2003.
- [110] J. Lian, L. Wang, X. Sun, Q. Yu, and R. C. Ewing, "Patterning metallic nanostructures by ion-beam-induced dewetting and rayleigh instability," *Nano Letters*, vol. 6, pp. 1047–1052, 2012/02/19 2006.
- [111] K. Zhao, R. S. Averback, and D. G. Cahill, "Patterning of metal nanowires by directed ion-induced dewetting," *Applied Physics Letters*, vol. 89, no. 5, p. 053103, 2006.
- [112] C. Favazza, J. Trice, H. Krishna, R. Kalyanaraman, and R. Sureshkumar, "Laser-induced short- and long-range ordering of Co nanoparticles on SiO₂," *Appl. Phys. Lett.*, vol. 88, pp. 1531181–83, 2006.
- [113] H. Krishna, A. K. Gangopadhyay, J. Strader, and R. Kalyanaraman, "Nanosecond laser-induced synthesis of nanoparticles with tailorable magnetic anisotropy," *Journal of Magnetism and Magnetic Materials*, vol. 323, pp. 356–362, 2 2011.
- [114] G. K. Mor, M. A. Carvalho, O. K. Varghese, M. V. Pishko, and C. A. Grimes, "A room-temperature TiO₂-nanotube hydrogen sensor able to self-clean photoactively from environmental contamination," *J. Mater. Res.*, vol. 19, no. 2, p. 628, 2004.
- [115] C. Wang, L. Yin, L. Zhang, Y. Qi, N. Lun, and N. Liu, "Large scale synthesis and gas-sensing properties of anatase tio₂ three-dimensional hierarchical nanostructures," *Langmuir*, vol. 26, pp. 12841–12848, 2012/03/09 2010.
- [116] P. Tobiska, A. Hugon, A. Trouillet, and H. Gagnaire, "An integrated optic hydrogen sensor based on SPR on palladium," *Sensors and Actuators B*, vol. 74, p. 168, 2001.
- [117] C. K. Kim, J. H. Lee, Y. H. Lee, N. I. Cho, and D. J. Kim, "A study on a platinum-silicon carbide Schottky diode as a hydrogen gas sensor," *Sensors and Actuators B*, vol. 66, p. 116, 2000.
- [118] Z. Fan, J. C. Ho, T. Takahashi, R. Yerushalmi, K. Takei, A. C. Ford, Y. Chueh, and A. Javey, "Toward the development of printable nanowire electronics and sensors," *Advanced Materials*, vol. 21, p. 3730, 2009.
- [119] H. M. van Driel, J. E. Sipe, and J. F. Young, "Laser-induced periodic surface structures on solids: a universal phenomenon," *Phys. Rev. Lett.*, vol. 49, no. 26, pp. 1955–1959, 1982.
- [120] S. E. Clark and D. C. Emmony, "Ultraviolet-laser-induced periodic surface structures," *Phys. Rev. B*, vol. 40, no. 4, pp. 2031–2043, 1989.
- [121] D. Bauerle, *Laser Processing and Chemistry*. Berlin: Springer, second ed., 1996.
- [122] I. H. Malitson, "Interspecimen comparison of the refractive index of fused silica," *J. Opt. Soc. Am.*, vol. 55, p. 1205, 1965.

- [123] N. Shirato, J. Strader, A. Kumar, A. Vincent, P. Zhang, A. Karakoti, P. Nacchimuthu, H. J. Cho, S. Seal, and R. Kalyanaraman, "Thickness dependent self limiting 1-d tin oxide nanowire arrays by nanosecond pulsed laser irradiation," *Nanoscale*, vol. 3, no. 3, pp. –, 2011.
- [124] S. Shukla, S. Patil, S. C. Kuiry, Z. Rahman, T. Du, L. Ludwig, C. Parish, and S. Seal, "Synthesis and characterization of sol-gel derived nanocrystalline tin oxide thin film as hydrogen sensor," *Sensors and Actuators B: Chemical*, vol. 96, pp. 343–353, 11 2003.
- [125] *Handbook of Optics*, vol. 2. McGraw-Hill, 2 ed., 1994.
- [126] V. M. Jimenez, J. P. Espinos, A. Caballero, L. Contreras, A. Fernandez, A. Justo, and A. R. Gonzalez-Elipe, "SnO₂ thin films prepared by ion beam induced CVD: preparation and characterization by X-ray absorption spectroscopy," *Thin Solid Films*, vol. 353, p. 113, 1999.
- [127] J. S. C. Prentice, "Coherent, partially coherent and incoherent light absorption in thin-film multilayer structures," *J. Phys. D: Appl. Phys.*, vol. 33, pp. 3139–3145, 2000.
- [128] O. Heavens, *Optical Properties of Thin Solid Films*. Dover Publications, 1991.
- [129] L. W. Kurt and J. C. Thomas, "Thermal conductivity of clear fused silica at high temperatures," *Journal of Applied Physics*, vol. 30, p. 1702, 1959.
- [130] P. Bouchut, D. Decruppe, and L. Delrive, "Fused silica thermal conductivity dispersion at high temperature," *Journal of Applied Physics*, vol. 96, p. 3221, 2004.
- [131] L. B. Pankratz *US Bureau of Mines Bulletin*, vol. 672, 1984.
- [132] D. Taylor *Trans. J. British Ceramic Soc.*, vol. 83, p. 32, 1984.
- [133] P. Tiirkes *J. Phys, C: Solid St. Phys.*, vol. 13, p. 4941, 1980.
- [134] *CRC Handbook of Chemistry and Physics*. 2009.
- [135] T. Schwarz-Selinger, D. G. Cahill, S. C. Chen, S. J. Moon, and C. P. Grigoropoulos, "Micron-scale modifications of si surface morphology by pulsed-laser texturing," *Physical Review B*, vol. 64, pp. 155323–, 09 2001.
- [136] C. Yaws, ed., *Chemical Properties Handbook*. McGraw-Hill, 1999.
- [137] M. Ohring, *The Materials Science of Thin Films*. Harcourt Brace jovanovich, 1992.
- [138] P. D. Desai *J. Phys. Chem. Ref.*, vol. 15, p. 967, 1986.
- [139] K. K. Kelley, "Bulletin no. 476," *US Bureau of Mines*, vol. 476, 1949.
- [140] C. F. Lucks, H. W. Deem, and W. D. Wood *American Ceramic Socety Bulletin*, vol. 39, p. 313, 1960.
- [141] L. van Vlack, *Physical Ceramics for Engineers*. Addison-Wesley Publishing Co., 1964.

- [142] G. Nicolas and I. Prigogine, *Self-Organization in Non-Equilibrium Systems*. New York: Wiley, 1977.
- [143] H. R. Stuart and D. G. Hall, “Island size effects in nanoparticle-enhanced photodetectors,” *Appl. Phys. Lett.*, vol. 73, no. 26, pp. 3815–3817, 1998.
- [144] S. Pillai, K. R. Catchpole, T. Trupke, G. Zhang, J. Zhao, and M. A. Green, “Enhanced emission from Si-based light-emitting diodes using surface plasmons,” *Appl. Phys. Lett.*, vol. 88, no. 16, p. 161102, 2006.
- [145] J. Cole and N. Halas, “Optimized plasmonic nanoparticle distributions for solar spectrum harvesting,” *Appl. Phys. Lett.*, vol. 89, p. 153120, 2006.
- [146] J.-M. Nam, C. S. Thaxton, and C. A. Mirkin, “Nanoparticle-Based Bio-Bar Codes for the Ultrasensitive Detection of Proteins,” *Science*, vol. 301, p. 1884, 2003.
- [147] M.-C. Daniel and D. Astruc, “Gold Nanoparticles: Assembly, Supramolecular Chemistry, Quantum-Size-Related Properties, and Applications toward Biology, Catalysis, and Nanotechnology,” *Chem. Rev.*, vol. 104, pp. 293–346, 2004.
- [148] W. K. Park, R. J. Ortega-Hertogs, J. S. Moodera, A. Punnoose, and M. Seehra, “Semiconducting and ferromagnetic behavior of sputtered Co-doped TiO₂ thin films above room temperature,” *J. Appl. Phys.*, vol. 91, no. 10, p. 8093, 2002.
- [149] S. Sun, C. B. Murray, D. Weller, L. Folks, and A. Moser, “Monodisperse fept nanoparticles and ferromagnetic fept nanocrystal superlattices,” *Science*, vol. 287, no. 5460, pp. 1989–1992, 2000.
- [150] R. Seemann, S. Herminghaus, and K. Jacobs, “Dewetting patterns and molecular forces,” *Phys. Rev. Lett.*, vol. 86, pp. 5534–37, 2001.
- [151] C. Redon, F. Brochard-Wyart, and F. Rondelez, “Dynamics of dewetting,” *Physical Review Letters*, vol. 66, no. 6, pp. 715–718, 1991.
- [152] T. Stange and D. Evans, “Nucleation and growth of defects leading to dewetting of thin polymer films,” *Langmuir*, vol. 13, pp. 4459–4465, 1997.
- [153] U. Thiele, M. G. Velarde, and K. Neuffer, “Dewetting: film rupture by nucleation in the spinodal regime,” *Phys. Rev. Lett.*, vol. 87, no. 1, p. 016104, 2001.
- [154] L. Kondic, J. A. Diez, P. D. Rack, Y. Guan, and J. D. Fowlkes, “Nanoparticle assembly via the dewetting of patterned thin metal lines: Understanding the instability mechanisms,” *PHYSICAL REVIEW E*, vol. 79, FEB 2009.
- [155] J. Becker, G. Grun, R. Seeman, H. Mantz, K. Jacobs, K. Mecke, and R. Blossey, “Complex dewetting scenarios captured by thin-film models,” *Nature Materials*, vol. 2, p. 59, 2003.

- [156] J. Trice, R. Kalyanaraman, and R. Sureshkumar, “Computational modeling of laser-induced self-organization in nanoscopic metal films for predictive nanomanufacturing,” in *Instrumentation, Metrology, and Standards for Nanomanufacturing* (M. T. Postek and J. A. Allgair, eds.), vol. 6648 of *Proceedings of SPIE*, p. 66480K, SPIE, SPIE, 2007.
- [157] A. Atena and M. Khennar, “Thermocapillary effects in driven dewetting and self assembly of pulsed-laser-irradiated metallic films,” *Physical Review B (Condensed Matter and Materials Physics)*, vol. 80, no. 7, p. 075402, 2009.
- [158] P.-G. de Gennes, “The dynamics of a spreading droplet,” *C. R. Acad. Paris*, vol. 298, pp. 111–115, 1984.
- [159] P. G. de Gennes, “Wetting: statics and dynamics,” *Rev. Mod. Phys.*, vol. 57, pp. 827–863, Jul 1985.
- [160] L. Kondic, “Instabilities in gravity driven flow of thin fluid films,” *SIAM Review*, vol. 45, p. 95, 2003.
- [161] E. Guyon, J.-P. Hulin, L. Petit, and C. D. Matescu, *Physical Hydrodynamics*, ch. Hydrodynamic instabilities, pp. 439–489. Oxford university press, 2001.
- [162] A. Sharma and E. Ruckenstein, “Finite-Amplitude Instability of Thin Free and Wetting Films: Prediction of Lifetimes,” *Langmuir*, vol. 2, pp. 480–494, 1986.
- [163] P.-G. de Gennes, F. Brochard-Wyart, and D. Quere, *Capillarity and Wetting Phenomenon*. New york: Springer, 2003.
- [164] N. Shirato, H. Krishna, A. K. Gangopadhyay, and R. Kalyanaraman, “Magnetic measurement of pulsed laser-induced nanomagnetic arrays using surface magneto-optic kerr effect,” vol. 7767, p. 77670Q, SPIE, 2010.
- [165] A. Westphalen, M.-S. Lee, A. Remhof, and H. Zabel, “Invited article: Vector and bragg magneto-optical kerr effect for the analysis of nanostructured magnetic arrays,” *Review of Scientific Instruments*, vol. 78, no. 12, p. 121301, 2007.
- [166] S. Visnovsky, *Optics in magnetic multilayers and nanostructures*. CRC Press, 2006.
- [167] M. Faraday, “Experimental researches in electricity. nineteenth series,” *Philosophical Transactions of the Royal Society of London*, vol. 136, pp. 1–20, 1846.
- [168] J. Kerr, “Xliii. on rotation of the plane of polarization by reflection from the pole of a magnet,” *Philosophical Magazine Series 5*, vol. 3, pp. 321–343, 2012/04/30 1877.
- [169] J. Zak, E. R. Moog, C. Liu, and S. D. Bader, “Universal approach to magneto-optics,” *Journal of Magnetism and Magnetic Materials*, vol. 89, pp. 107–123, 9 1990.
- [170] Z. J. Yang and M. R. Scheinfein, “Combined three-axis surface magneto-optical kerr effects in the study of surface and ultrathin-film magnetism,” *Journal of Applied Physics*, vol. 74, no. 11, pp. 6810–6823, 1993.

- [171] J.-W. Lee, J.-R. Jeong, D.-H. Kim, J. S. Ahn, J. Kim, and S.-C. Shin, “Three-configurational surface magneto-optical kerr effect measurement system for an ultrahigh vacuum in situ study of ultrathin magnetic films,” *Review of Scientific Instruments*, vol. 71, no. 10, pp. 3801–3805, 2000.
- [172] H. Zeng, R. Skomski, L. Menon, Y. Liu, S. Bandyopadhyay, and D. J. Sellmyer, “Structure and magnetic properties of ferromagnetic nanowires in self-assembled arrays,” *Physical Review B*, vol. 65, pp. 134426–, 03 2002.
- [173] P. R. Krauss, P. B. Fischer, and S. Y. Chou, “Fabrication of single-domain magnetic pillar array of 35 nm and 65 bits/in² density,” *J. Vac. Sci. Technol. B*, vol. 12, p. 3639, 1994.
- [174] R. M. H. New, R. F. W. Pease, and R. L. White *J. Vac Sci. Technol. B*, vol. 12, p. 3196, 1994.
- [175] S. Y. Chou, P. R. Krauss, and L. Kong, “Nanolithographically defined magnetic structures and quantum magnetic disk,” *J. Appl. Phys.*, vol. 79, p. 6101, 1996.
- [176] M. Salerno, J. R. Krenn, B. Lamprecht, G. Schider, H. Ditlbacher, N. Felidj, A. Leitner, and F. R. Aussenegg *Opto-Electron. Rev.*, vol. 10, p. 217, 2002.
- [177] R. S. Molday and D. Mackenzie *J. Immunol. Methods*, vol. 52, p. 353, 1982.
- [178] A. Jordan, R. Scholz, P. Wust, H. Schirra, T. Schiestel, H. Schmidt, and R. Felix *J. Magn. Magn. Mater.*, vol. 194, p. 185, 1999.
- [179] D. H. Reich, M. Tanase, A. Hultgren, L. A. Bauer, C. S. Chen, and G. J. Meyer, “Biological applications of multifunctional magnetic nanowires (invited),” *Journal of Applied Physics*, vol. 93, no. 10, pp. 7275–7280, 2003.
- [180] E. J. Felton and D. H. Reich, *Biological Applications of Multifunctional Magnetic Nanowires*, pp. 1–22. John Wiley & Sons, Inc., 2007.
- [181] H. Krishna, N. Shirato, A. K. Gangopadhyay, and R. Kalyanaraman, “Fe nanomagnets with unusual size-dependent magnetization directions produced by fast laser-induced self-organization,” *Proc. SPIE*, vol. 7039, p. 703909, 2008.
- [182] K. Nielsch, R. B. Wehrspohn, J. Barthel, J. Kirschner, U. Gosele, S. F. Fischer, and H. Kronmuller, “Hexagonally ordered 100 nm period nickel nanowire arrays,” *Applied Physics Letters*, vol. 79, no. 9, pp. 1360–1362, 2001.
- [183] C. Kittel, “Theory of the structure of ferromagnetic domains in films and small particles,” *Physical Review*, vol. 70, pp. 965–971, 12 1946.
- [184] H. Krishna, N. Shirato, S. Yadavali, R. Sachan, J. Strader, and R. Kalyanaraman, “Self-organization of nanoscale multilayer liquid metal films: Experiment and theory,” *ACS Nano*, vol. 5, pp. 470–476, 2012/04/29 2010.

- [185] M. Khenner, S. Yadavali, and R. Kalyanaraman, “Formation of organized nanostructures from unstable bilayers of thin metallic liquids,” *Physics of Fluids*, vol. 23, no. 12, p. 122105, 2011.
- [186] R. Sachan. PhD thesis, University of Tennessee, 2012.
- [187] H. Garcia, R. Sachan, and R. Kalyanaraman, “Optical plasmon properties of co-ag nanocomposites within the mean-field approximation,” *Plasmonics*, vol. 7, no. 1, pp. 137–141, 2012-03-01.

Vita

Nozomi Shirato was born in Tokyo, Japan, on 27 February 1985, the son of Mitsuko Shirato and Satoshi Nemoto. After completing his work at Seijou High School, he went to Saint John's Preparatory School in Minnesota where he spent one year for post graduation study. Then, after one year of study at the College of Saint Benedict and Saint John's University, he transferred to Washington University in St. Louis where he studied physics and received his Bachelor of Arts in May 2008. For the next four years he pursued Doctor of Philosophy degree in Materials Science and Engineering at the University of Tennessee, Knoxville. He completed the program in August 2012.